

**Using reaction-diffusion equations to model and  
simulate the interaction of bone cells with  
electrical stimulation**

Dissertation

zur

Erlangung des akademischen Grades

Doktor-Ingenieur (Dr.-Ing.)

der Fakultät für Informatik und Elektrotechnik

der Universität Rostock

**vorgelegt von**

Bachir Delenda, geboren am 22.12.1986 in Ain Touta  
aus Algerien

Rostock, 2020

**Datum der Einreichung:** 08.04.2020  
**Datum der Verteidigung:** 14.10.2020

### **Gutachter**

Prof. Dr. Ursula van Rienen, Universität Rostock, Fakultät für Informatik und Elektrotechnik Institut für Allgemeine Elektrotechnik

Prof. Dr. Rüdiger Köhling, Universitätsmedizin Rostock, Oscar Langendorff Institut für Physiologie

Prof. Dr. José Manuel García Aznar, Universität Zaragoza, Fakultät für Maschinenwesen

# Abstract

Electrical stimulation is being used clinically to promote bone ingrowth on implant surfaces and bone healing after complicated fractures. The osseointegration of biomaterials in bone requires complex biological interactions between different bone cells types and electrical stimulation. There are several assumptions and approaches in different studies in order to explain how cells respond to electrical stimulation and whether their response is dependent on the cell type. However, this mechanism of cell sensing and responding is not well understood. This work addresses modeling and simulation of the interactions between bone cells and electrical stimulation. An *in vitro* system is constructed in order to conduct electro-taxis experiments on osteoblasts. Two kinds of cells are used in the experiments, osteoblast-like cell line MG-63 and human osteoblasts derived from the femur of a patient. A mathematical model of the effect of electrical stimulation on osteoblasts is discussed. This model is based on the general law of conservation and the different strategies for cells in sensing their surrounding environment. The electric field strength inside the chamber is simulated. In addition, the electrochemical impedance created at the electrodes is modeled. In the experimental part we have observed primary human osteoblast's migration toward the anode. However, MG-63 cells have showed random movements. Furthermore, we have carried out a simulation study on an *in vivo* application. A 3D electro-stimulating dental implant with the surrounding tissues is modeled. First results of cells interaction and migration toward the implant surface are achieved.

# Zusammenfassung

Die elektrische Stimulation wird klinisch eingesetzt, um das Einwachsen von Knochen auf Implantatoberflächen sowie die Knochenheilung nach komplizierten Frakturen zu fördern. Die Osseointegration von Biomaterialien im Knochen unterliegt dabei komplexen biologischen Interaktionen zwischen Knochenzellen und der elektrischen Stimulation. Es gibt verschiedene Annahmen und Ansätze in unterschiedlichen Studien, um zu erklären, wie die Zellen auf elektrische Stimulation reagieren und ob die Reaktion vom Zelltyp abhängig ist. Allerdings ist dieser Mechanismus der Zellerkennung und -reaktion nach wie vor nicht gut verstanden. Im Rahmen dieser Arbeit erfolgte daher die Modellierung und Simulation der Wechselwirkungen zwischen Knochenzellen und elektrischer Stimulation mit Hilfe eines konstruierten in-vitro Systems, um elektrotaktische Experimente an Osteoblasten durchzuführen. In den Experimenten wurden zwei Arten von Zellen verwendet, eine osteoblastenähnliche Zelllinie MG-63 und menschliche Osteoblasten, die aus dem Oberschenkelknochen eines Patienten gewonnen wurden. Es wird ein mathematisches Modell der Wirkung der elektrischen Stimulation auf die Osteoblasten vorgestellt, welches auf dem allgemeinen Erhaltungssatz und den verschiedenen Strategien für Zellen, ihre Umgebung zu erfassen, basiert. Die elektrische Feldstärke im Inneren der Kammer sowie die an den Elektroden erzeugte elektrochemische Impedanz wurde modelliert. Im experimentellen Teil konnte die Migration primärer menschlicher Osteoblasten zur Anode beobachtet werden. Im Gegensatz dazu haben die MG-63-Zellen jedoch zufällige Bewegungen gezeigt. Darüber hinaus haben wir eine Simulationsstudie über eine in vivo-Anwendung der elektrischen Stimulation zur Knochenregeneration durchgeführt. Dabei wurde ein 3D-elektrostimulierendes Zahnimplantat mit dem umgebenden Gewebe modelliert. Erste Ergebnisse der Zellinteraktion und der Migration zur Implantatoberfläche konnten erzielt werden.

# Acknowledgement

First of all, I would like to express my deepest appreciation to my supervisor Prof Ursula van Rienen, for providing guidance and feedback throughout this research. She has given me kind support, encouragement and was always willing and enthusiastic to assist in any way she could throughout my research.

Secondly, I would like to extend my sincere thanks to Prof. Rüdiger Köhling, Prof. Rainer Bader and Prof. Barbara Nebe for their valuable advices and their kind collaboration during my research. I am also grateful to their teams, especially Josefin Ziebart and Caroline Mörke who provided me support to conduct experiments on bone cells.

I would also like to thank all my PhD colleagues for their support and nice discussions. Particularly, I would like to thank Thanh Duy Truong, Märwan Kebbach, Eden Tafa Tulu, Dr. Bernhard Himmel and Dr. Christian Bahls for their strong support and encouragement.

I am also grateful to all my friends. Particularly, Tariqe Hamza, Toufik Boudjellal and Abdelali Bouguelaa for their encouragement and support.

My research would not have been possible without the financial support from the German Science Foundation (DFG) through the research training group 1505/2 welisa. I would like to acknowledge their support.

Finally, my success and the completion of my dissertation would not have been possible without the support and encouragement of my family. Particularly, my parents and my wife. My deepest gratitude to them for always being there.

# Contents

<b>List of Figures</b>	<b>vi</b>
<b>1 Introduction</b>	<b>1</b>
1.1 Motivation . . . . .	1
1.2 Importance of numerical simulations for predicting bone ingrowth and cell-implant interactions . . . . .	2
1.3 Organization . . . . .	3
<b>2 Peri-implant healing</b>	<b>5</b>
2.1 Brief history of implants . . . . .	5
2.2 Basic aspects of bone biology . . . . .	6
2.2.1 Bone cells . . . . .	6
2.2.2 Bone morphology . . . . .	7
2.2.3 Bone tissue . . . . .	8
2.2.4 Bone remodeling . . . . .	10
2.2.5 Bone ingrowth on metallic implants . . . . .	12
2.3 Multiscale aspects of the biointerfaces . . . . .	15
<b>3 Interaction between electrical components and cells</b>	<b>17</b>
3.1 Mechano-biological models . . . . .	18
3.1.1 Brief overview of partial differential equations . . . . .	19
3.1.2 Basic concepts of finite element method . . . . .	20
3.1.3 Reaction-diffusion model by George Khalil . . . . .	21
3.1.4 Reaction-diffusion model by Pedro Moreo . . . . .	24
3.2 Effect of electrical stimulation on cells . . . . .	29
3.3 Mathematical modeling of cell sensing strategies . . . . .	31
3.3.1 Cell response strategies to environmental cues . . . . .	32
3.4 Maxwell's equations for electrical stimulation at low frequency . . . . .	33
3.4.1 Steady-state electric currents . . . . .	34
3.5 Coupling reaction-diffusion equations with electrical stimulation . . . . .	34
<b>4 Determination of model parameters from <i>In vitro</i> studies</b>	<b>37</b>
4.1 Experimental setup . . . . .	37
4.1.1 Silver chloride coating preparation . . . . .	37
4.1.2 Electro-taxis chamber construction . . . . .	38
4.1.3 Voltage and pH measurements . . . . .	41

4.1.4	Accuracy in measurements . . . . .	43
4.1.5	Cell's observation . . . . .	45
4.2	Numerical simulation of electrical components . . . . .	54
4.2.1	Customized electro-taxis chamber . . . . .	54
4.2.2	Convergence study . . . . .	55
4.2.3	Visualization of the stimulating electric field . . . . .	57
4.2.4	Impedance and thickness of silver chloride layer . . . . .	59
4.3	Equivalent circuit for AgCl layer . . . . .	60
4.4	Parametric study . . . . .	62
4.5	Avoiding negative concentrations . . . . .	65
4.6	Numerical simulation of bone cell population . . . . .	66
4.6.1	Model parameters . . . . .	67
4.6.2	Comparison of both numerical models . . . . .	70
<b>5</b>	<b>Numerical study of <i>in vivo</i> electro-stimulating system</b>	<b>73</b>
5.1	Mathematical framework . . . . .	73
5.2	3D dental implant design . . . . .	74
5.3	Electric field distribution . . . . .	76
5.4	Evolution of platelets concentration . . . . .	78
5.5	Discussion . . . . .	78
<b>6</b>	<b>Conclusions and outlook</b>	<b>81</b>
6.1	Conclusions . . . . .	81
6.1.1	Coupling reaction diffusion equations with electrical stimulation	82
6.1.2	Electro-taxis chamber construction . . . . .	82
6.1.3	<i>In vitro</i> studies . . . . .	83
6.1.4	Electric field strength and cells populations simulations . . . . .	84
6.1.5	<i>In vivo</i> studies . . . . .	84
6.2	Outlook . . . . .	85
6.2.1	The effect of surface roughness and topography on bone cells .	85
6.2.2	Numerical studies on osteoblasts using a reaction-diffusion model	86
<b>A</b>	<b>Appendix</b>	<b>88</b>
A.1	The main steps followed to model a combined stationary and transient system . . . . .	88
	<b>Bibliography</b>	<b>94</b>

# List of Figures

2.1	Composition and hierarchical structure of bone at different scales. . .	8
2.2	Bone tissue . . . . .	10
2.3	Schematic representation of the basic multicellular unit (BMU) during bone remodeling process. . . . .	11
2.4	Illustration of host bone-implant interface. . . . .	14
2.5	Multiscale aspects of the biointerfaces between the surface of implants and the biological elements. Figure 2.5 is extended from [1] . . . . .	16
3.1	The motivation behind studying the electrical stimulation of bone cells.	18
3.2	Typical finite element method elements in two dimensions. . . . .	21
3.3	Diagram representing the main elements considered in the mathematical model of George Khalil et al. and their interactions. . . . .	24
3.4	Diagram representing the main elements considered in the mathematical model of Pedro Moreo et al. and their interactions. . . . .	26
3.5	(a) Three dimensional dental implant (image from Neobiotech CMI IS-II active <sup>®</sup> ). (b) Dimension of the computational domain implant-host bone cavity and the boundary conditions. Figure 3.5 is adapted and used with permission from [2]. . . . .	27
3.6	Concentration of the adsorbed proteins in case of an implant with rough surface . . . . .	28
3.7	Distribution of the concentration of growth factor S1 after 14 days in case of a rough surface. The left and right figure show the results from Pedro Moreo's model and our simulation result, respectively. Left figure is used with permission from [2]. . . . .	29
3.8	Response of a cell to electrical stimulation in case of negligible voltage-gated conductance of the cell membrane. The figure is adapted and used with permission from [3]. . . . .	30
3.9	Response of a cell to electrical stimulation in case of voltage-gated conductance of the cell membrane. The figure is adapted and used with permission from [3]. . . . .	31
4.1	Electrodeposition of silver chloride AgCl on silver wire Ag. . . . .	39
4.2	3D printed electro-taxis chamber (middle) and the corresponding support. The complete system is already in the bottom . . . . .	40
4.3	Electro-taxis chamber designed in AutoCAD 2014. . . . .	41
4.4	Curve fitting of the measured data. . . . .	43



4.5	The used equipments for electro-taxis experiments. . . . .	44
4.6	Electro-taxis chamber under time lapse microscopy, Carl Zeiss AG (Prof. Nebe Lab, Dept. of Cell Biology, Rostock University Medical Center). . . . .	45
4.7	Visualization of osteoblast-like cell line MG-63 under time lapse microscopy . . . . .	47
4.8	Visualization of osteoblast-like cell line MG-63 under time lapse microscopy . . . . .	48
4.9	Modified electro-taxis chamber under Leica DMI 6000 microscope, (laboratory of Prof. Köhling Oscar Langendorff Institute of Physiology). . . . .	49
4.10	Visualization of osteoblast-like cell line MG-63 under time lapse microscopy . . . . .	51
4.11	Visualization of primary human osteoblasts under time lapse microscopy. . . . .	53
4.12	Three dimensional electro-taxis chamber with electrodes are imported to COMSOL MULTIPHYSICS <sup>®</sup> version 5.1. . . . .	54
4.13	This graph shows the relative error RE of the estimated concentration of osteoblasts inside the circular opening as function of the degrees of freedom. . . . .	56
4.14	Discretization of the CAD model. . . . .	57
4.15	Distribution of the electric field amplitude $\mathbf{E}$ (coloured scale) and the current density $\mathbf{J}$ (red arrows) inside the electro-taxis chamber. . . . .	57
4.16	This graph shows the comparison between the simulated magnitude of electric field strength $\mathbf{E}_{sim}$ and the measured ones $\mathbf{E}_{meas}$ inside the culture medium. . . . .	59
4.17	Equivalent circuit of the electric double layer in case of ideally polarizable and nonpolarizable electrodes adapted from [4]. . . . .	61
4.18	Results of the parametric study. . . . .	63
4.19	Results of the parametric analysis. Figure (a) shows the averaged relative error. The smallest relative error is highlighted by the red point. Figure (b) shows the improvement of the prediction of the simulated electric field value inside the culture medium. . . . .	64
4.20	Simulation of the electric field inside the electro-taxis chamber after including a resistive layer at the electrode with resistivity value calibrated based on the experimental measurements, see figure 4.11. . . . .	65
4.21	Electro-taxis chamber. . . . .	67
4.22	Temporal evolution of primary human osteoblasts inside the culture medium. . . . .	69
4.23	This graph resumes the temporal evolution of the population of primary human osteoblasts inside the circular opening near the anode ( $C_A$ ) and near the cathode ( $C_C$ ) as a function of time $t$ . . . . .	70
4.24	Comparison between the original method and the transformed one. . . . .	71

5.1	Electrostimulating dental implant. . . . .	75
5.2	Electro-stimulating dental implant and the surrounding tissues. . . . .	76
5.3	Distribution of the electric field strength around the dental implant. . . . .	77
5.4	Density of platelets $C$ one day (top figure) and four days (below figure) after placement of the implant in the case of an implant without ES (a, c) and with the ES (b, d). . . . .	80
6.1	Generation of three-dimensional rough surface using COMSOL MULTIPHYSICS <sup>®</sup> version 5.1. B: Adding the rough surface to the original stimulating system. . . . .	86
A.1	Global parameters. . . . .	88
A.2	Adding physics interfaces. Electric currents (ec) and coefficient form PDE (C) interfaces are highlighted. . . . .	89
A.3	The electric currents interface (ec). . . . .	90
A.4	The coefficient form PDE (C) interface. . . . .	91
A.5	Mesh generation. . . . .	92
A.6	The study node. . . . .	93

# 1 Introduction

## 1.1 Motivation

Electrical stimulation is of great importance especially because of the key role it plays in promoting several physiological processes, such as fracture, peri-implant and wound healing [5]. In orthopedics, the use of electrical stimulations techniques has become significant in clinical applications since the discovery of the electric properties of the bone in the 1950s [6].

More than six decades ago, Yasuda et al. [7] first investigated the electrical properties of bone and discovered that bone is a piezoelectric material, in other words bone exposed to mechanical load can generate an endogenous electric potential. This discovery provided more explanation to Wolffs law [8], which states that mechanical load leads to bone growth. The work of these scientists led us to ask the question whether bone growth could be stimulated directly using external electrical stimulation. Thereby, increasing the activity of osteoblasts could help to cure bone diseases e.g. osteoporosis, non-union fracture and implant failure. For instance, electrical stimulation could promote osteoblasts and bone precursor cells activity, hence enhancing and accelerating bone formation around the implants [9].

The pioneering work of Yasuda et al was continued furthermore in 1964. In 1964, Basset et al [10] reported on bone ingrowth around a cathode, which was inserted into the medullary cavity of dogs' femurs. Various types of exogenous electrical stimulation were recorded. In most of the cases DC voltages are applied [10], [11], [12], [13], [14] because it can be easily incorporated in a bone implant. Inductive coupling [15] and capacitive coupling were also investigated in several studies [16], [17], [18].

Bone healing requires a complex physiological process. Osteoblasts migration, adhesion, differentiation and proliferation play an important role in bone healing [19]. It is reported that osteoblasts respond to mechanical stimulation [20] as well as electrical stimulation [21]. However, the mechanism of the response is not well understood. The discovery of endogenous potentials by Luigi Galvani in the 18th century [22] had inspired many scientists to investigate the natural potentials existence in different kinds of tissues and to apply an external electrical stimulation to enhance its functionality.

At the cellular level, the mechanism of how cells sense and respond to external electrical stimulation remains poorly understood. Electrical stimulation plays an important role in cellular physiology. It can interfere in cell growth, apoptosis,

## 1 Introduction

proliferation and migration. Focusing on electro-taxis, in most cases of applied DC voltage, cells move towards the cathode; such as, human keratinocytes [23], bovine vascular endothelial cells [24], osteoblasts [10], chondrocyte and anterior cruciate ligament fibroblasts [25]. However, it is also reported in literature that some kind of cells move towards the anode; similar to the previous one, keratocyte fragments [26], osteoclasts [10], murine resident peritoneal macrophage [27].

Cells respond differently to electrical stimulation. Mycielska et al. [3] explains that the main causes of the directional movement of cells are the influx and efflux of  $\text{Ca}^{2+}$ , which are caused by the cell membrane hyperpolarization at the anode side and depolarization at the cathode side.

The primary focus of the current study is to model and simulate the interactions between bone cells and electro-stimulating systems using reaction-diffusion models. Initially, peri-implant healing is described and discussed. Secondly, a mathematical model of the coupling of reaction-diffusion models and electrical stimulation is discussed. The mathematical formulation is based on the fundamental conservation law and the different strategies of cell sensing of their external environment. Experiments are conducted in the labs in order to stimulate osteoblast-like cell line MG-63 and primary human osteoblasts. The obtained results from the experiments are used as an input to the mathematical model. Equivalent to the experimental setup, an *in silico* model i.e. a numerical model for computer simulations, is implemented in some finite element-based software. Furthermore, studies are conducted to minimize the relative error between the obtained results from the experimental measurements and the *in silico* model. The effect of the electric field on osteoblasts is observed. From *in vitro* to *in vivo* system, an electro-stimulating dental implant is simulated including the surrounding tissues. The first response of platelets to electrical signals is investigated. First results show that electrical stimulation could increase the number of adhered platelets to the surface of the implant and therefore improve bone ingrowth on implant surfaces.

### 1.2 Importance of numerical simulations for predicting bone ingrowth and cell-implant interactions

Bone ingrowth on implant surfaces is a complex process. It involves a group of cells. Each cell is regulated by various signaling pathways and molecules, which are secreted in most cases by the cells themselves [28]. Bone growth is also affected by external stimulus, mechanical load, characteristics of the implants surfaces and electromagnetic field [29].

In computational biology, it is a challenge to create a relevant model that makes use of the experimental data, which takes into account the role of each stimulus,

## 1 Introduction

molecule and signaling pathways. The main aim of this modeling is to produce a model that is capable of predicting the bone growth under different circumstances. Reducing the complexity of bone growth process by modeling and simulations could give a better understanding of the interactions between bone cells in different stimulation environments. For instance, the electric field strength and current flow in the surrounding tissues of the electro-stimulating system is difficult or sometimes impossible to quantify or observe in real experiments, however it is possible in a relevant model. A parametric study could be easily performed on the model to study in details the different factors that affect the process of bone ingrowth on implant surfaces. However, it is costly and time consuming in real experiments. Uncertainty in stimulating related factors and its influence on the outcome results could be quantified by numerical studies. For instance, small differences in the electrical properties of bone tissue may affect the accuracy of the electric field strength inside the bone tissue. Therefore, the design of electro-stimulating bone implants could be enhanced via conducting experimental simulations.

### 1.3 Organization

This dissertation consists of six chapters and it is organized as follows:

Chapter I introduces the importance of numerical simulations for predicting bone ingrowth and cell-implant interactions. It also gives a short overview of the work of Yasuda et al and how it explains Wolff's law. The role of electrical stimulation in cellular physiology is also briefly described.

Chapter II describes the biological background of this research. A brief history of implants from the ancient civilizations up to the 20th century is given. It also includes the basic aspects of bone biology in the context of the different types of bone cells, bone morphology, bone tissue, bone remodeling and the bone ingrowth on metallic implants. Finally, the main aspects considered in biointerfaces and some examples of the existing models in different scales, from nano-scales to macro-scales, are provided.

Chapter III analyzes in detail two known mechano-biological models, model of George Khalil and Pedro Moreo, of osseointegration of bone on metallic implants. The model of Pedro Moreo is simulated in COMSOL Multiphysics<sup>®</sup> version 5.1 and compared to the original results. Different types of partial differential equations are derived based on the cell sensing strategies. A summary of Maxwell's equations is given, including the differential form and steady-state electric currents approximation.

Chapter IV describes the *in vitro* studies. The electro-taxis chamber is first constructed in AutoCAD and then printed using a 3D printer, then the Agar-bridges and the silver chloride electrodes are prepared. Experiments are then conducted on osteoblast-like cell line MG-63 and primary human osteoblasts. In addition,

## 1 Introduction

the methods and approaches used to study numerically the electrical components inside the electro-taxis chamber are presented. Finally, the interactions between the electrical stimulation and the cells are simulated.

Chapter V gives the application of reaction-diffusion equations to electro-stimulating implants. The reaction-diffusion model is used to describe the coupling of the interaction of bone cells with the electric field as they are observed in *in vivo* studies. For this, we introduce a mathematical model framework consisting of a system of coupled partial differential equations. Platelets migration and interaction within a realistic three dimensional model adapted from an electro-stimulating dental implant is studied. DC voltage of 3.1 V is applied at the electrodes. The electric field distribution around the electro-stimulating dental implant is simulated. High concentration of platelets around the implant surface is achieved after one day of healing. Based on these results, it is shown that osseointegration of dental implants in bone could be enhanced and accelerated by means of electrical stimulation.

Chapter VI describes the significance of this research, model validation and limitation. Possible future work is also given.

## 2 Peri-implant healing

The aim of this chapter is to provide a brief summary of the biology of bone. This chapter is divided into three subsections: The implants history part gives an overview of the evolution of bone implants. In the second subsection, basic aspects of bone biology are discussed in context of different types of bone cells, bone morphology, bone tissue, bone remodeling and the bone ingrowth on metallic implants. Finally, the last subsection provides the main aspects considered in biointerfaces and some examples of the existing models in different scales, from nano-scales to macro-scales.

### 2.1 Brief history of implants

Bone implants have been used since a hundred of thousands of years ago. Evidence of the Mayan and Egyptian civilization using seashells, curved iron and animal teeth were found by archaeologist. They tried to replace teeth but none of them lasted for enough time [30]. However, their attempts show their intention to implant artificial materials inside the bone.

Modern orthopedic implants are based on the discovery of the Swedish orthopedic surgeon Per Ingvar Branemark in 1952. He accidentally discovered the osseointegration when he was trying to study the blood flow during the healing process inside a rabbit bone [31]. He placed a metallic cage made out of titanium through the skin and observed the behavior of the blood cells. After finishing his study, he tried to remove the piece of metal but he found that it was already integrated in the bone [32]. Branemark called his discovery Osseointegration. In 1965 Branemark treated a patient named Goesta Larsson. She was the first patient in the world that has been treated by a titanium dental implant [33]. Even though it was the first dental implant inserted in a human mandible it was successful [33].

After the discovery of Branemark in 1952, scientists tried to study the effect of electrical stimulation on bone growth. In 1956, Noguchi studied the effect of direct current on bone growth. He found that bone growth increases in the presence of direct currents [34]. Further more, Basset et al did some studies *in vivo* on canine femora using 1.4 V mercury cell battery connected in series with a resistor. They found that almost the total occupation of the medullary cavity by new bone is around the cathode, the stimulating electric currents they have used are 1 A, 10 A and 100 A [10].

Nowadays, there exist several types of electro-stimulating implants (e.g. orthopedic implants [35], [36], cochlear implants [37], [38], deep brain stimulation [39], [40] and

the pioneering cardiac pacemaker [41], [42]). In bone-implant applications, three methods of bone stimulation are commonly used: Direct currents, capacitive electric field and pulsed electromagnetic field (PEMFs) [43].

## 2.2 Basic aspects of bone biology

The aim of this section is to briefly provide a summary of the basic aspects of the biology of bone including: The description of the different types of bone cells, bone tissue, bone remodeling, and the mechanisms of osseointegration, hence the ingrowth of bone on implants.

### 2.2.1 Bone cells

Bone is a living tissue. It consists mainly of five types of cells: Osteoprogenitors, osteoblasts, osteocytes, bone lining cells and osteoclasts [44]. They interact and communicate with each other to adapt the bone to the mechanical loading [45] and maintain the balance of bone formation and resorption [44].

The osteoprogenitors also known as inactive osteoblasts [46] are derived from mesenchymal stem cells in bone marrow [47]. Besides, they are present in the inner layer of the periosteum, Volkmann's and Haversian canal and endosteum [44]. They are undifferentiated and non-specialized cells. They have the ability to differentiate to osteoblasts under certain conditions.

The osteoblasts are known for their role in bone formation. They are mononucleate and cuboidal with an average diameter between 20-30  $\mu\text{m}$  [48]. They are arranged on the inner and outer surface of the bone (endosteum and periosteum, respectively) [44]. These cells have similar characteristic of typical synthesizing cells, including endoplasmic reticulum and enlarged golgi apparatus [49]. Mature osteoblasts produce bone matrix by synthesizing and mineralizing collagen. During bone remodeling process, 60 % to 70 % of osteoblasts undergo apoptosis; The remaining differentiate to osteocytes as they are embedded within the bone and some cells stay inactive on the surface of the bone as bone lining cells [50] and [51].

Alive osteoblasts that do not differentiate to osteocytes become bone lining cells. The latter, have flat and slender shape [52]. In contrast to osteoblasts, bone lining cells are able to produce intercellular adhesion molecule 1 (ICAM1), however they are not able to produce osteocalcin [53]. Bone lining cells can get activated if they are stimulated mechanically or chemically [44].

Osteocytes, which compose 90 % to 95 % of the total amount of bone cells, are mature bone cells that rise from the differentiation of osteoblasts and become embedded in bone matrix [54]. Therefore they are no more capable of migrating to other sites [55]. They are the longest-lived cells in humans with a life span up to 20 years [56]. During their life span, they reside inside small cavities named lacunae



## 2 Peri-implant healing

[56]. By means of their dendritic morphology, osteocytes form a complex network, through which they are connected to the neighboring osteocytes and also to other bone cells, e.g. osteoblasts and bone lining cells [44]. Unlike osteoblasts, which are typical protein synthesizing cells, osteocytes are less active, relatively small and possess few intercellular organelles [57]. Through the canaliculi, which are canals surrounding the dendrites and filled with extracellular fluid, osteocytes communicate to other cells and exchange nutrients [58]. Osteocytes are involved in maintenance of bone. They are capable of activating bone remodeling at the sites of damage in case a microdamage is occurred [58]. Furthermore, they play a key role in sensing the mechanical load and also mineralizing bone [59].

Osteoclasts, known for their essential role in bone resorption, are relatively huge cells with a diameter between 20-100  $\mu\text{m}$  [60]. They are multinucleated cells and contain five to ten nuclei [49]. These motile cells are located on the surface of cortical and cancellous bone. Mature osteoclasts bind to the surface of the bone via integrins and create a closed environment surrounding the resorption areas [61]. They release acids and hydrolase to break down and resorb bone matrix. As a result, minerals and organic materials are liberated [62]. Osteoclasts activity is regulated by different kinds of cells. For instance, osteoblasts stimulate the maturation of osteoclasts by expressing RANKL [63]. See figure 2.3 for schematic representations of bone cells and their interactions.

### 2.2.2 Bone morphology

The adult human skeleton consists of around 206 bones [64]. This total number of bones are divided as following: 126 bones in the appendicular skeleton, 74 bones in the axial skeleton and six in the auditory ossicles [65]. Based on the form and structure of the bone, it can be divided into four categories: long bones, short bones, flat bones and irregular bones [65]. Their mass and size are different from one individual to another.

The human skeleton performs several functions which could be mechanical, biological or chemical. It can serve as a repository or reservoir of minerals. Human skeleton consists of 99 % of calcium, around 90 % of phosphate, and approximately 65 % of sodium in the body [66]. The skeleton plays an essential role in the protection of the soft organs, like spinal cord, heart, lungs and brain. It supports and provides the framework of the whole body. Another important feature of the skeleton is to permit the movement of different parts of the body with the help of the joints.

The bone is considered as anisotropic and heterogeneous material [67], which means that it does not preserve the same mechanical and electrical properties in one location at different directions. This is because of the irregular hierarchical structure of bone at different scales [67], see figure below.

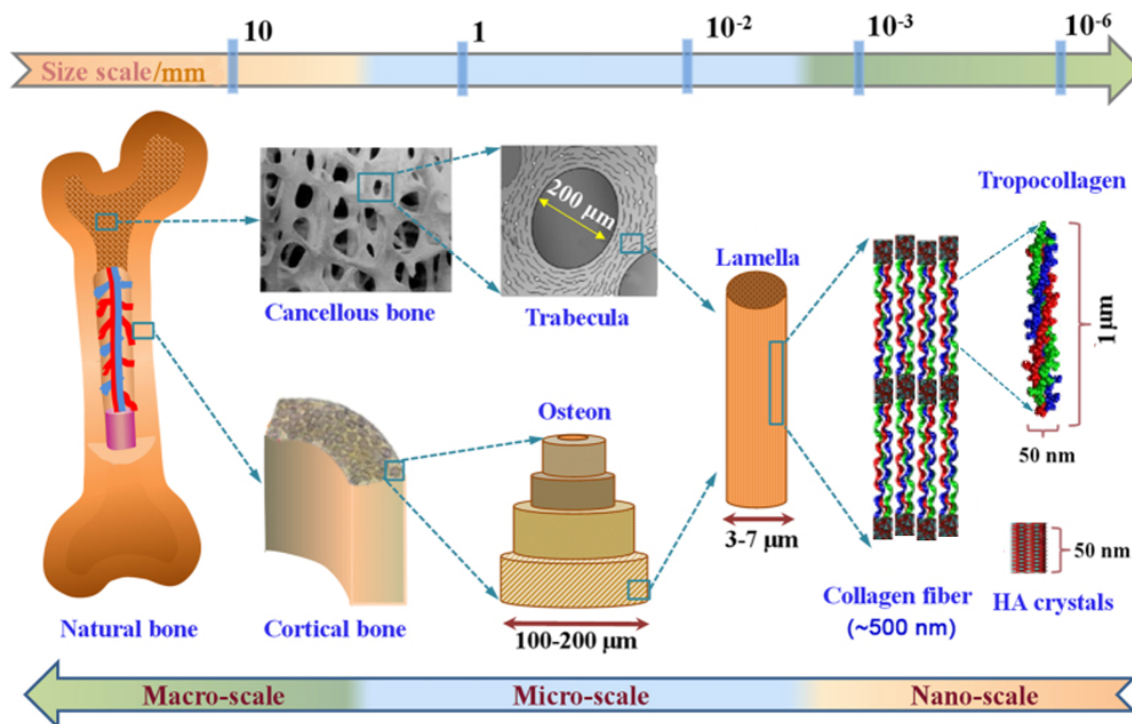


**Figure 2.1:** Composition and hierarchical structure of bone at different scales. From left to right: Natural bone; cortical and cancellous bone tissue. Cortical bone is compact and solid, it makes up the outer layer of the bone. Cancellous bone has a porous and spongy framework, it constructs the inner layer of bones; At the microstructure level, osteon and trabecula are the units produced during bone remodeling. Each osteon has a ring structure, it consists of a central canal called Haversian canal, which contains blood vessels and nerves; Lamellae (approximately  $3-7 \mu\text{m}$  of diameter) which surrounds the osteons; Collagen fibers (approximately  $500 \text{ nm}$  of diameter) are arranged in a parallel way; and hydroxyapatite crystals (approximately  $50 \text{ nm}$  of length) which are mineral crystals that determine the strength of bone at nano-scale; Tropocollagen is an organic material (approximately  $50 \text{ nm}$  of diameter and  $1 \mu\text{m}$  of length) [68]. The figure 2.1 is adapted and used with permission from [69] and [68].

### 2.2.3 Bone tissue

Bone is a connective tissue where different types of cells are connected together through a hard extracellular matrix [70]. The extracellular matrix is synthesized by bone cells themselves through a very complex biological interactions. Different kinds of tissue contribute to its dynamic behavior, including periosteum, red bone marrow, nerves, yellow bone marrow and endosteum [71].

There are two types of bone tissue: cortical and cancellous bone tissue. Cortical bone, which constitutes around 80 % of the skeletal mass, is compact and solid, it makes up the outer layer of the bone [72]. Cancellous bone, which constitutes only 20 % has a spongy form, it constructs the inner layer of bones [72]. At micro-structure

## 2 Peri-implant healing

level, cortical bone is made up with osteons, which represents its basic functional unit produced during remodeling process. Each osteon has a ring structure, it consists of (1) a central canal or tube called Haversian canal, which contains blood vessels and nerves. (2) Lamellae, which constitute circumferential layers of the extracellular matrix surrounding the Haversian canal. (3) Lacunae, which is the space where the osteocytes are founded. (4) Canaliculi, which are tiny canals between the lacunae. It allows the flow of nutrients and minerals to the osteocytes [73]. Compact bone and cancellous bone consist of the same components, some of them are organic compounds like extracellular matrix, cells and lipids and inorganic like crystalline hydroxyapatite and water [74].

The outer membrane of the bone is called periosteum, it consists of fibrous layer and osteogenic layer. The fibrous layer consists of fibroblasts and the osteogenic layer consists of progenitor cells which may differentiate to osteoblasts. The periosteum is connected to the Haversian canals via Volkmann's canals [75].

There are two types of bone marrow, red and yellow marrow. Red bone marrow is a flexible tissue found inside the spongy bone, it is the source of red blood cells, white blood cells and platelets [76]. Yellow bone marrow is a fatty tissue, it stores fat to support the other organs in times of need and it is also a source of mesenchymal stem cells which can differentiate to different kind of cells [77].

Endosteum is the inner membrane of the cortical bone or the outer membrane of the spongy bone, which consists of a thin layer of flat endosteal lining cells that covers the central cavity or medullary cavity. Osteoprogenitor cells, osteoblasts and osteoclasts can be also found in some areas of the endosteum [78].

Lacunae or osteocytes lacunae, which have irregular and ellipsoidal shape, are small cavities where osteocytes reside during their life time. Osteocytes communicate to other cells and exchange the nutrients via the canaliculi, which are canals surrounding the dendrites and filled with extracellular fluid [79].

### Compact Bone & Spongy (Cancellous Bone)

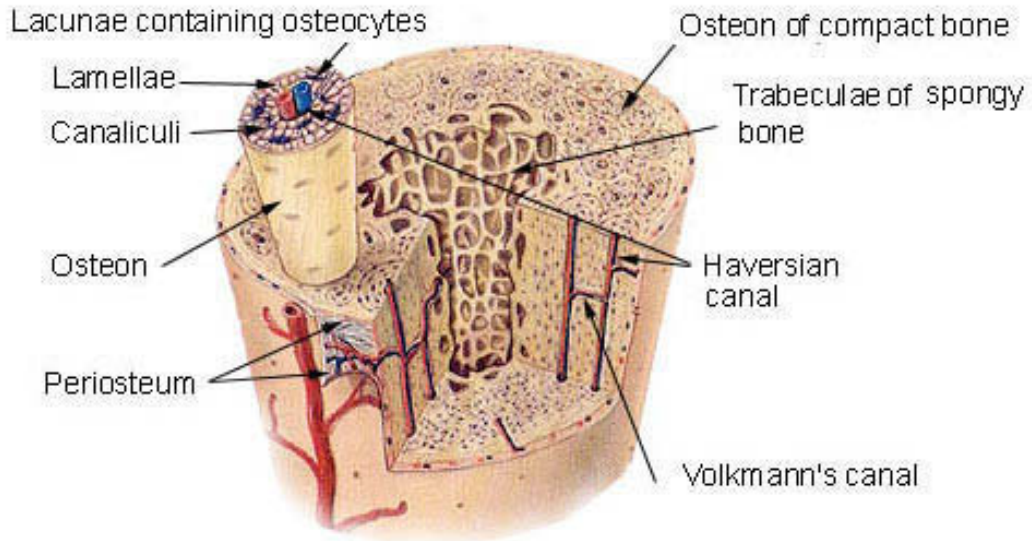


**Figure 2.2:** Bone tissue. Two types of bone can be distinguished, cortical and cancellous bone. In contrast to cancellous bone which constitutes around 80 % of the mass of skeletal, cortical bone constitutes to 20 %. At micro-structure level, osteons are the basic functional unit of cortical bone. Each osteon has a ring structure and it consists of a central canal or tube called Haversian canal, lamellae, which are circumferential layers of extracellular matrix surrounding the Haversian canal, lacunae, which is the space where the osteocytes are founded and canaliculi, which are tiny canals between the lacunae. Periosteum is the outer membrane of the bone, and is connected to Harversian canals via Volkmann's canal. Endosteum is the inner membrane of the cortical bone, hence the outer membrane of the spongy bone<sup>1</sup>.

#### 2.2.4 Bone remodeling

Although bone is a hard tissue, it is very active and dynamic tissue. It changes its structure continuously during its life span [55], the old bone is removed by osteoclasts and new bone is formed by osteoblasts. This biological process is called bone remodeling. There are three main processes involved in bone remodeling cycle, bone resorption, reversal (mononuclear cells emerge on the bone surface) and bone formation [80].

<sup>1</sup><https://en.wikipedia.org/wiki/Bone>

## 2 Peri-implant healing

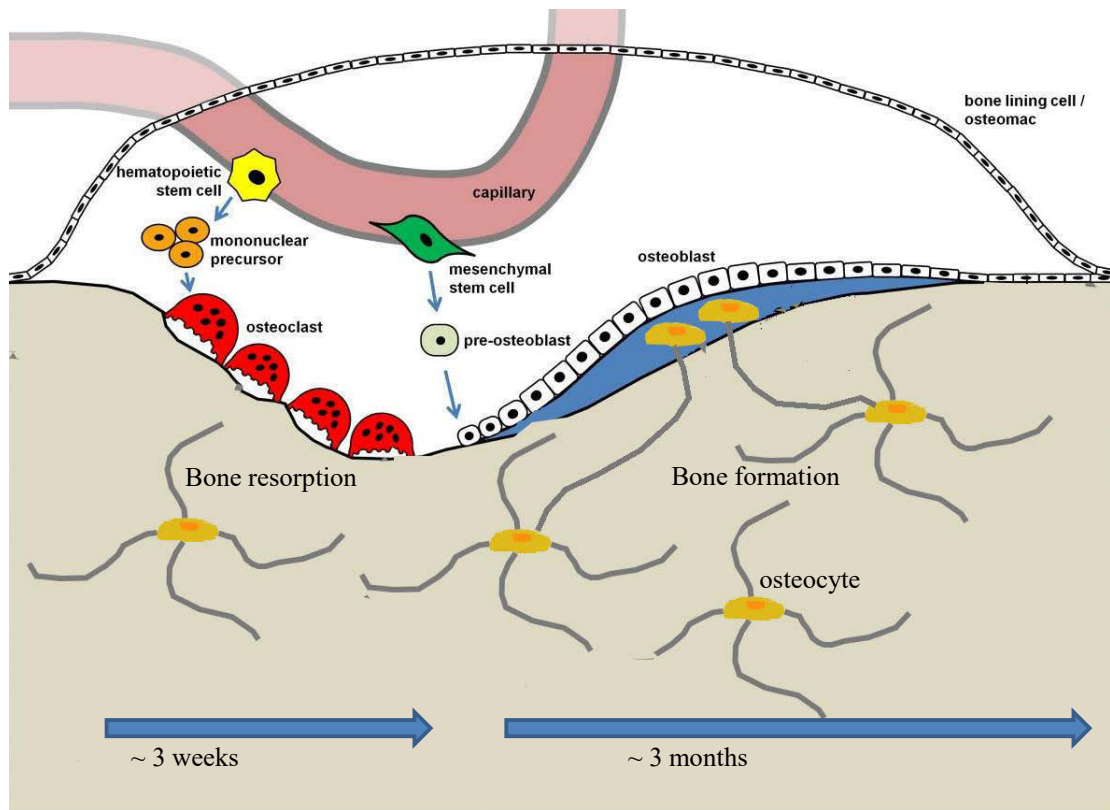


**Figure 2.3:** Schematic representation of the basic multicellular unit (BMU) during bone remodeling process. The resorption of bone tissue is carried out by osteoclasts in a duration of 3 weeks, then a new bone is formed by osteoblasts, which lasts for 3 months. Mesenchymal and hematopoietic stem cells flow from the bone marrow to the local domains, where bone remodeling takes place, then they differentiate to osteoclasts and osteoblasts, respectively. The response of osteocytes and lining cells to the physiological stimuli triggers the bone remodeling process [81]. Figure 2.3 is adapted and used with permission from [81].

Bone remodeling is regulated by hormones or mechanical forces [82]. Lining cells, also called osteoblast-lineage cells which line the surfaces of bone in resting state, are perturbed by microdamage or mechanical stress [83]. Osteocytes, which form a complex network inside the bone, sense this mechanical change of the lining cells and trigger the bone remodeling process [84]. At each remodeling cycle the bone is broken down by osteoclasts in duration of approximately three weeks in humans [9]. Hematopoietic stem cells flow from the bone marrow to the local domains, where bone remodeling is taking place. They differentiate to mononuclear precursor cells and then fuse together to form osteoclasts, these latter bind its surface integrins to vitronectin (bone protein) and create a sealed environment at the resorptions zones [81]. Activated osteoclasts lower the pH of the remodeling sites to facilitate

## 2 Peri-implant healing

bone resorption, they secrete acids like: tartrate-resistant acid phosphatase and enzymes like: cathepsin K, matrix metalloproteinase 9, and gelatinase. Besides bone resorption, this process leads to the release of minerals and organic molecules contained in the bone matrix [72]. At the level of resorption areas, osteoblasts begin to build up new bone. Bone formation takes much longer, it lasts approximately three to four months in each remodeling cycle [85]. Mesenchymal cells are migrated from bone marrow to the remodeling sites where they differentiate to pre-osteoblasts and then to osteoblasts [86]. The latter synthesize organic bone matrix which contains mostly collagen type I, in order to fill the resorption areas. Finally, the osteoblasts promote calcium salts and phosphor to bind to the newly formed osteoid which leads to the mineralization of bone matrices [87]. Figure 2.3 illustrates the essential bone cells involved in bone remodeling process.

Due to aging the balance between the bone formation and resorption might be not maintained. The increase of bone resorption over bone formation leads to decrease of bone mass density (BMD) which may cause osteoporosis [88].

### 2.2.5 Bone ingrowth on metallic implants

The stability is a key factor in the success of implant placement that can last for a long time. However, this remains a challenging task for clinicians. The stability of the implant is guaranteed by both of the primary and secondary implant stability. Primary or initial stability, which comes directly after implant insertion, is insured by the mechanical friction between the surface of the implant and the host bone. The secondary stability, which comes after the bone ingrowth on the surface of the implant, requires a complex sequence of biological events that lead to osseointegration<sup>2</sup>. Many factors have a direct effect on the primary stability. For instance, bone quality and quantity, implant characteristics and surgical methods. However secondary stability is affected mainly by the primary stability [89].

Osseointegration, which is taken from the greek word osseon, which means bone, and the latin word integrare, which means creating a whole [90], is defined by professor Per-Ingvar Branemark as the direct structural and functional connection between ordered living bone and the surface of load carrying implant [91].

The main biological cascade events involved in bone-implant healing are presented in figure 2.4. Initially, hematoma occur first, the blood vessels are damaged due to implants site preparation, the blood contained in the blood vessels is leaking to the cavity between the host bone and the implant immediately after inserting the implant. On the part of the implant, some proteins and ions contained in the blood will bind to the surface of the implant. This adsorption is considered to be the trigger of the

---

<sup>2</sup>Sometimes scientists also use "osteointegration", however the term osseointegration is often used instead of osteointegration (as it is discussed in the following example website <https://clinicalgate.com/osteointegration-osseointegration/>) and therefore we only use "osseointegration".

## 2 *Peri-implant healing*

following cellular reactions. This will be followed by cells adhesion [92]. For instance, platelets, which are small, nonnucleated and subcellular fragments contained in the blood [93], bind to these proteins which leads to their adherence to the surface of the implant [94]. The effect of platelets activation, which is caused by its adherence to the surface of the biomaterial, can be observed first on the cells themselves. They change their shape and gather the storage granules to the center, followed by the release of these granules, hence, histamines, serotonin and several kinds of growth factors like platelet-derived growth factor (PDGF) and transforming growth factor beta (TGF-B) [95]. This process will result in a high density of signaling molecules at the surface of the biomaterial in comparison to the surface of the bone, which may effect the migration of fibroblasts, neutrophils, smooth muscle cells, and osteogenic cells by means of chemotaxis [95]. Following platelets activation, fibrin clot is formed by transforming of prothrombin to thrombin. Drilling the cavity will lead to cessation of circulation, thus to ischemia and necrosis.

By the time necrosis happens, the inflammatory response takes place. Neutrophils and monocytes migrate to the implant site to accumulate damaged tissue, beside monocytes differentiation to macrophages, they become activated and start secreting interleukin IL1 and IL6. New blood vessels are needed to replace the ones damaged during the surgical preparation of the implant site. This process is called angiogenesis. It is important for peri-implant healing as well as other natural processes such as maturation of certain organs, formation of a living vertebrate organism, wound healing and reproduction [96]. Angiogenesis is required since its the only way to supply different bone cells of nutrients. The endothelial cells, which are stimulated by vascular endothelial growth factor (VEGF), are the cells responsible for forming new blood vessels [95].

In the next phase, mesenchymal cells migrate to the surface of the biomaterial through the fibrin network. In their way, they may differentiate to osteoprogenitor cells and later to osteoblasts. These biological events are mainly promoted by the different factors secreted by platelets and leukocytes. This phase is called contact osteogenesis [95]. Formation of new bone may also start in the direction from host bone to the surface of the implant, which is in opposition to the process mentioned previously, this is called distance osteogenesis [95].

Initially, woven bone matrix is formed at the surface of the implant, which is synthesized by the newly differentiated osteoblasts, and grows to the old bone and links them together to provide a mechanical stability to the implant. The woven bone has a random and unorganized structure of collagen fibers. At the final stage of the bone-implant healing, the woven bone is probably transformed to lamellar bone which is characterized by its organized structure of collagen fibers and their near-parallel orientation to the implant. This process is called bone remodeling [97].

## 2 Peri-implant healing

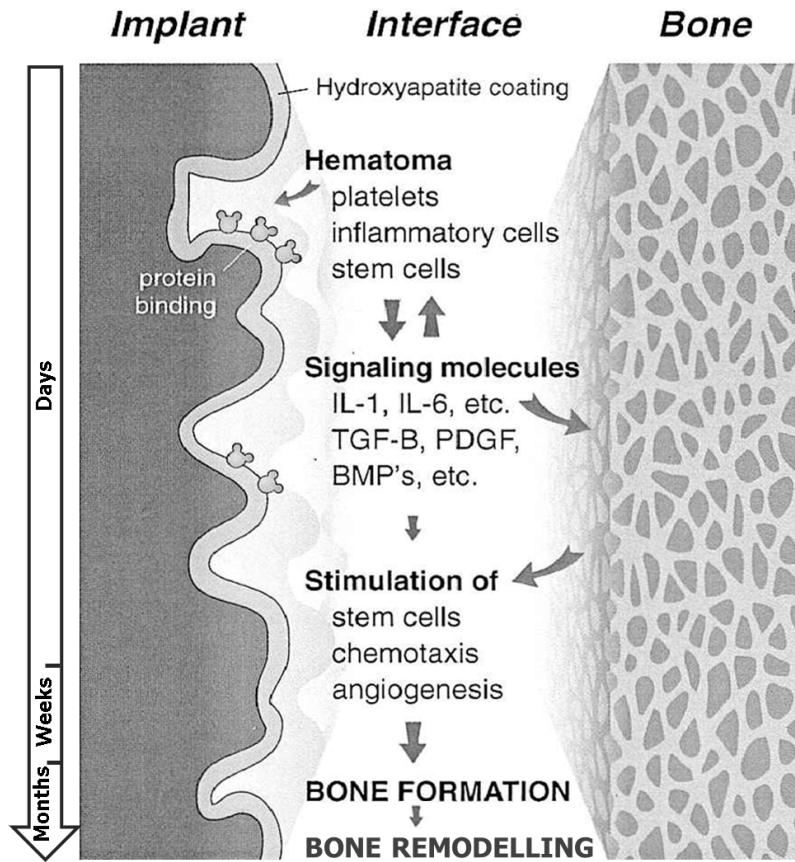


**Figure 2.4:** Illustration of host bone implant interface. The essential biological processes involved in peri-implant healing are shown above including their time evolution [98]. Initially, hematoma occurs first leading to protein binding to the implant surface. This facilitates platelets adherence to the implant surface followed by their activation. At the same time inflammatory cells invade the implant site. Both platelets and inflammatory cells release the essential signaling molecules for bone formation, e.g., IL-1, IL-6, TGF-B, PDGF and BMP's. Angiogenesis is important for the supply of bone cells with nutrients. Stem cells are migrated to the surface of the bone where they may differentiate to osteogenic cells and then to osteoblasts. This cascade of interactions results in bone formation and at the end stage to bone remodeling, which lasts for long time. The figure 2.4 is adapted from [99]. Used with permission of Nordic Orthopaedic Federation.



## 2.3 Multiscale aspects of the biointerfaces

Many factors and aspects affect the osseointegration or the growth of bone on implants. Characteristics of the surface of the implant, negatively and positively charged surface of hydroxyapatite have a remarkable effect on osteoblasts activity and new bone formation [100] and [101]. It has been shown experimentally that N-surface (negatively charged surface) of polarized hydroxyapatite promote osteoblasts adhesion and bone formation in comparison to P-surface (positively charged surfaces) and 0-surface (non-polarized surface) [102] and [103]. Besides, the surface topography and roughness [104] and [105], the properties of the surroundings of the bone, the mechanical loading process [106], and electrical stimulation [34], [107] and [108].

There exist considerable number of simplified mathematical models which implement in their mathematical formulations the main factors and aspects that influence the behavior of the osteoblasts during peri-implant healing process, hence, the amount of bone that occupies the space between the implant and the host bone and its anchorage to the surface of the implant. These models exist in different scales. For instance, at nano scale, a theoretical model [109] describes the relationship between the roughness of the titanium surface and its charge distribution and how this charge distribution influences the adhesion of osteoblasts on the titanium surface. At microscopic and macroscopic levels, proliferation and adhesion of osteoblasts were modeled in [110] as functions, which depend on time and surface roughness. Bone ingrowth on porous coated implants under the load and interface micro motion is described in [111]. The influence of fixation, elastic properties of the backing and friction at bone/implant interface on bone ingrowth is simulated in [112]. Simulation results in [113] show that anisotropy has an influence on peri-implant stress and strain. The dependence of bone ingrowth on the stiffness of the stem is demonstrated in [114]. Figure 3.4 illustrates the main aspects considered in peri-implant healing on different scales. On macro scale, geometrical design of the implant and structure of bone tissue is important. In micro scale, surface roughness and different kinds of cells shall be considered. Finally at the nano scale, the atomic structure of the biointerface, cell membrane, peptides amino acids and proteins are essential and must be taken into account.

## 2 Peri-implant healing

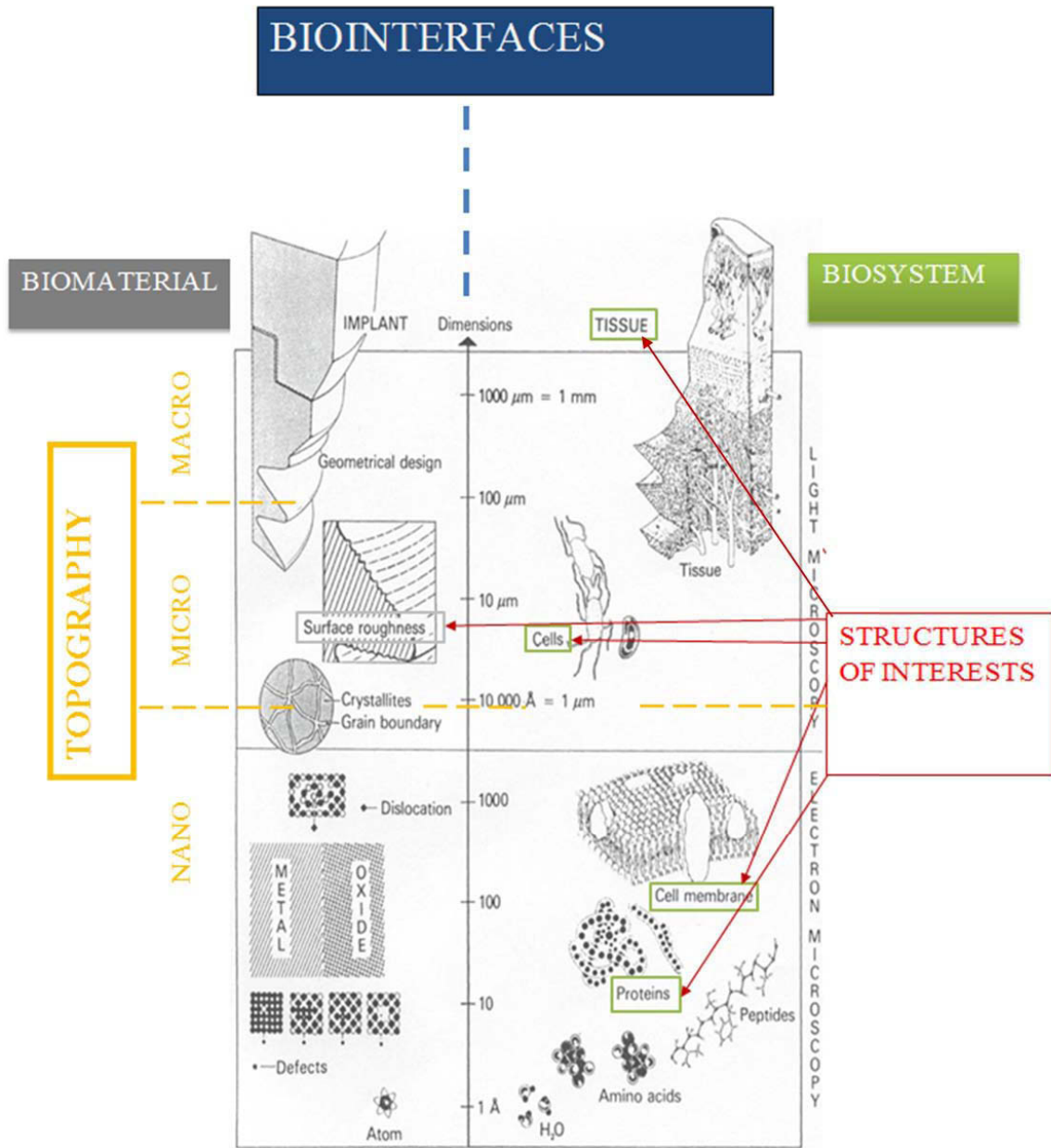


**Figure 2.5:** Multiscale aspects of the biointerfaces between the surface of implants and the biological elements. Figure 2.5 is extended and used with permission from [1].

### 3 Interaction between electrical components and cells

It is reported in literature [115] that endogenous potentials, potential differences and currents are generated at the site of the injury. These endogenous currents are stable, direct currents and last till the wound is healed. During the healing process, the endogenous potential affects the following cell characteristics: speed, migration, proliferation and differentiation. Many scientists are trying to enhance these endogenous potentials by applying external exogenous potentials. For example, at the University of Rostock, our research team of the DFG-funded Research Training Group 1505 welisa conducted *in vitro*, *in vivo*, and *in silico* experiments in order to enhance osteoblasts' migration, differentiation and proliferation. Our challenge is to find optimal parameters for stimulating osteoblasts and bone growth on implants. However, it is not well known how cells sense and respond to the electrical stimulation.

Furthermore, it is well known that mechanical load may stimulate bone formation that is known as Wolff's law [116]. However, the mechanism of how bone cells respond to mechanical stress is poorly understood. Yasuda et al. have conducted several studies on the mechanical and electrical properties of bone, and they have discovered that bone is a piezoelectric material, which means that bone exposed to load generates electric signals and vice versa. This work follows work by Basset et al.. In 1964 they have conducted *in vivo* studies on dogs where they have inserted a cathode inside a femur of a dog, and after finishing their experiments, they have noticed bone ingrowth on the cathode [10]. This work of these scientists had a significant impact on the development of electro-stimulating implants. For example, at the University of Rostock a hip revision system, which enriches the acetabular cup and the femoral component by electrodes, has been developed [117], [118] and [119]. The aim of this thesis consists in contributing to find suitable numerical models to perform not only macroscopic but also various kind of multiscale simulations for these and other bone implants.

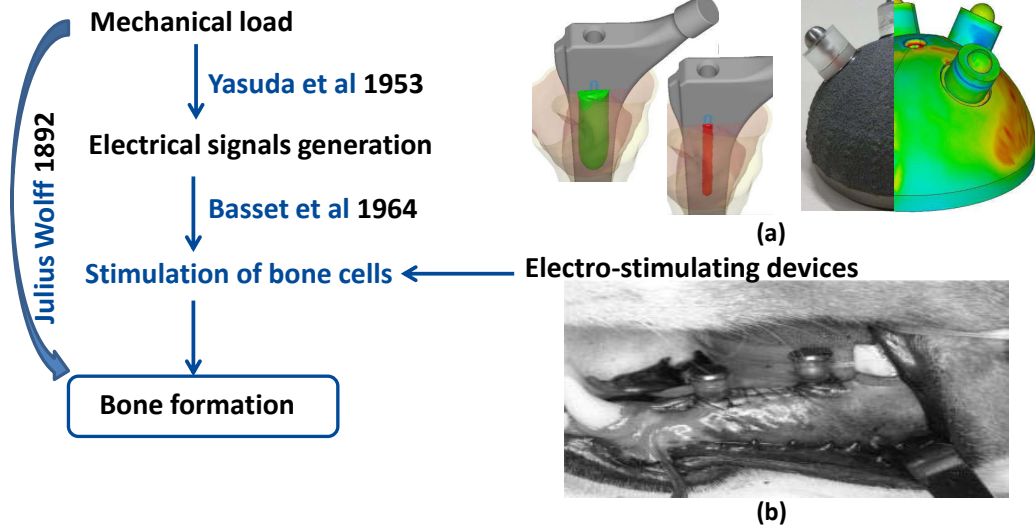


**Figure 3.1:** The motivation behind studying the electrical stimulation of bone cells. Figure (a) shows an electrically stimulating hip revision system (Courtesy of Ursula van Rienen and Ulf Zimmermann) and (b) an electronic dental implant insertion in mandible [120] (Courtesy of J. K. Song, used with permission from [120]).

### 3.1 Mechano-biological models

Mechano-biological models exist on different scales, macro, micro and nano. In multi-scale modeling of biointerfaces, all the scales are considered. The interactions, which take place on small scales (proteins, cell membrane and cells), result in significant changes in the structure on larger scales (tissue). The models on small levels explain the ambiguity on the large levels. Following a widely accepted approach, the set of continuous governing equations is based on the fundamental conservation law, where the temporal variation of the amount of quantity  $Q = Q(x, t)$  at time  $t$  and spatial position  $x$  is modeled, i.e. parabolic partial differential equations.

$$\frac{\partial Q}{\partial t} = J_Q + f_Q, \quad (3.1)$$

where  $J_Q$  is the flux of  $Q$ ,  $f_Q$  is the source term or the reaction term of  $Q$ . This model is often used in the field of mathematical modeling of biological systems in general [121]. For example, the basic reaction-diffusion-chemotaxis [122] model is

$$\frac{\partial Q}{\partial t} = D \nabla^2 Q - \chi(a) \nabla \cdot (Q \nabla a) + f(Q), \quad (3.2)$$

where  $D \nabla^2 Q$  is the diffusion flux,  $Q \chi(a) \nabla a$  is the chemotaxis flux,  $a$  is the attractant,  $\chi(a)$  is a function of the attractant concentration and  $f(Q)$  is the reaction term of  $Q$ .

### 3 Interaction between electrical components and cells

In this section we will give a short summary of mechano-biological models described in [123] and [2]. We choose to study these models because they both predict the peri-implant healing process. In addition, bone cells and tissues involved in the peri-implant healing process are mathematically modeled as well as the signaling pathways. The first model studies the influence of the stability of the implant on the healing process while the second model concentrates on modeling the effect of surface roughness on bone growth. In our research, these kinds of reaction-diffusion models are coupled with the electrical stimulation using the cells sensing strategies.

#### 3.1.1 Brief overview of partial differential equations

Second order partial differential equations encountered in physics can be classified into three types: elliptic, parabolic and hyperbolic. The three types of partial differential equations describe different phenomena. For instance, parabolic PDEs can model heat transfer and reaction-diffusion phenomena [124].

The order of a PDE is the order of the highest derivative. The general form of a linear second order partial differential equation of two-dimensional function  $u(x, y)$  or  $u(x, t)$  is written as follows:

$$Au_{xx} + 2Bu_{xy} + Cu_{yy} + Du_x + Eu_y + Fu + G = 0 \quad (3.3)$$

where  $A, B, C, D, E, F$  and  $G$  are unknown functions of  $x$  and  $y$ , the shorthand notations are:  $u_{xx} = \frac{\partial^2 u}{\partial x^2}$ ,  $u_{xy} = \frac{\partial^2 u}{\partial y \partial x}$ ,  $u_{yy} = \frac{\partial^2 u}{\partial y^2}$ ,  $u_x = \frac{\partial u}{\partial x}$  and  $u_y = \frac{\partial u}{\partial y}$ . We can distinguish three cases of the linear PDE depending on the values of the coefficients  $A, B$  and  $C$ :

$$\begin{aligned} B^2 - AC < 0 & \text{ elliptic} \\ B^2 - AC = 0 & \text{ parabolic} \\ B^2 - AC > 0 & \text{ hyperbolic} \end{aligned}$$

For illustration we consider some well-known PDEs in physics which are Laplace's, heat and wave equation [125]. Laplace's equation is a second order partial differential equation. It is an example of an elliptic PDE:

$$\frac{\partial^2 \psi}{\partial x^2} + \frac{\partial^2 \psi}{\partial y^2} = 0 \quad (3.4)$$

where  $\psi$  is the potential flow in two dimensions. In this case  $A = 1, B = 0$  and  $C = 1$ , thus  $B^2 - AC < 0$ . This kind of equations is often used to represent steady-state problems [126]. Heat equation in one dimension is written as follows

$$\frac{\partial T}{\partial t} = \alpha \frac{\partial^2 T}{\partial y^2} \quad (3.5)$$

### 3 Interaction between electrical components and cells

where  $T$  is the temperature at time  $t$  and position  $y$  and  $\alpha$  is the thermal diffusion coefficient. This equation satisfies the criteria for a parabolic PDE with  $A = \alpha$ ,  $B = 0$  and  $C = 0$ , and hence  $B^2 - AC = 0$ . This type of equations often describes the change of a quantity with respect to time and distance [126]. Next, the wave equation in one dimension is described as follows:

$$\frac{\partial^2 y}{\partial t^2} = \kappa \frac{\partial^2 y}{\partial x^2} \quad (3.6)$$

where  $\kappa$  is a non-negative real coefficient. Here,  $A = \kappa$ ,  $B = 0$  and  $C = 1$ , and therefore  $B^2 - AC < 0$ , which fulfil the criteria for an hyperbolic equation. This kind of equations is used to describe an oscillatory systems [126].

It is often difficult to find the exact analytical solution of the partial differential equations described in this subsection, therefore a numerical solution is needed. There exist two main concepts to transfer the continuous problems into discrete ones [127]. The first one, is to consider a finite number of nodes and approximate the derivatives by differences, the finite difference method is a well-known method for such an idea. The second one is to replace the exact solution by a representation in a finite number of basis functions, which is the concept beyond the finite element method. The most commonly used numerical methods for solving PDEs are the finite difference, finite element and finite volume schemes [128].

#### 3.1.2 Basic concepts of finite element method

Finite element method is a numerical technique or tool for solving partial differential equations. It is one of the most famous numerical techniques used to approximate the solution of PDEs [128]. Its ability to deal with complex geometries make it preferable in solving a wide range of engineering problems [129]. The basic idea of FEM is to divide the whole domain into smaller subdomains (finite elements, which is the origin of the name finite element method) [130]. Typical finite element method elements for structured grid are squares in two dimensions and cubes in three dimensions, and for unstructured grid are triangles in two dimensions and tetrahedra in three dimensions.

The basic steps involved in finite element method are [129]:

1. Establish the finite element mesh by subdividing the computational domain into a finite number of elements, e.g. triangles or squares in a two dimensional domain. These elements are interconnected at nodes (see figure 3.2).
2. Approximate the field variable (e.g., temperature or concentration) over an element using shape or basis functions, i.e.,  $f = \sum_{i=1}^n f_i \varphi_i$ , where  $f$  is the desired function,  $f_i$  are undetermined coefficients and  $\varphi_i$  are the basis functions.
3. Construct the residual formula by substituting the approximated field variable into the PDE, which has the form  $L[f] = s$ . The produced residual equation is

### 3 Interaction between electrical components and cells

written as follows:

$$r = L\left[\sum_{i=1}^n f_i \varphi_i\right] - s \quad (3.7)$$

where  $L$  is an operator and  $s$  is the source.

4. Determine the test functions  $\omega_i$  in order to weight the residual. In case the test function and the shape function are identical ( $\omega_i = \varphi_i$ ) the method is named Galerkin method.

5. Determine the unknown field variables  $f_i$  by setting the integral of the weighted residual to zero  $\int_{\Omega} \omega_i r d\Omega = 0$ .

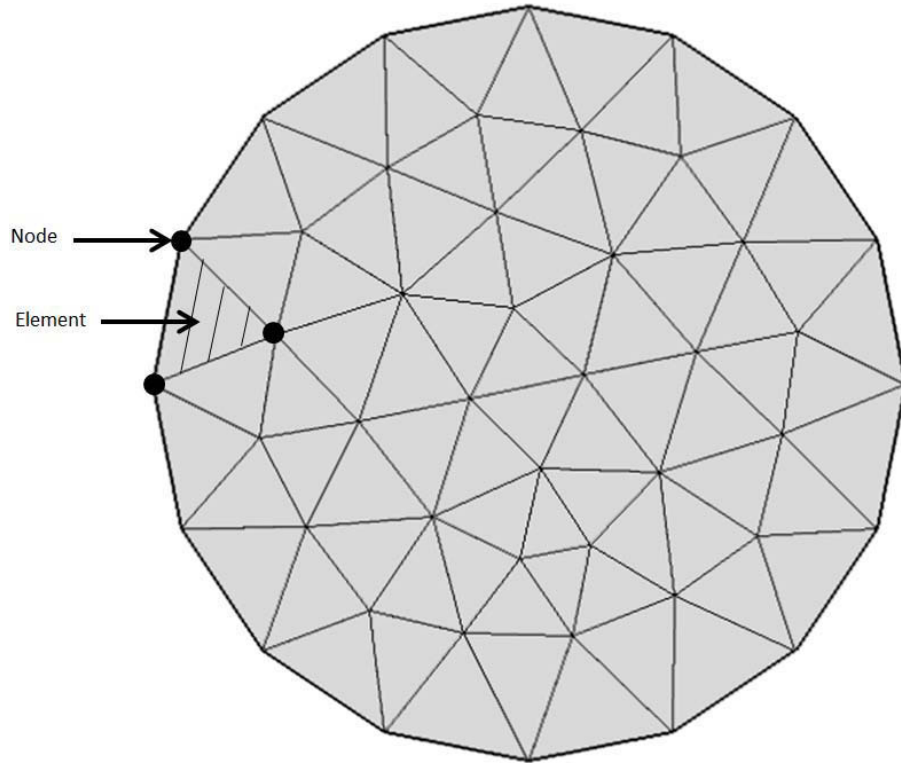


**Figure 3.2:** Typical finite element method elements in two dimensions. The whole disc is divided into smaller triangular elements.

#### 3.1.3 Reaction-diffusion model by George Khalil

The first model by George Khalil et al. [123] presents a mathematical framework to predict bone osseointegration on canine implant. The main variables that are described in the set of governing equations are: porosity ( $\phi^f$ ), populations of osteoblasts and endothelial cells, phases of bone growth factors (e.g. TGF-1), transforming angiogenic factors (TAF), osseous matrix ( $\phi^s$ ), and fibronectin factors (FF). The model variables are mathematically described as follows

### 3 Interaction between electrical components and cells

#### Solid and liquid fractions

A sample of total volume  $V$  is assumed to be composed of solid material and some fluid. Their volume fractions, i.e. their fractions normalized to the total volume  $V$ , add up to one:

$$\phi^s + \phi^f = 1 \quad (3.8)$$

where  $\phi^s$  is the solid fraction and  $\phi^f$  is the liquid fraction or porosity.

#### Endothelial cell population

The flux term of the endothelial cells is affected by the random motility, chemotaxis and haptotaxis. These terms are modeled as  $D^n \Delta n$ ,  $[\chi^n(c)n \cdot c]$  and  $[h^n n \cdot f]$ , respectively, where chemotaxis and haptotaxis are influenced by the gradient of TAF and FF.

$$\frac{\partial}{\partial t}(\phi^f Jn) = \phi^f (D^n \Delta n + [\chi^n(c)n \cdot c] + [h^n n \cdot f]) + \alpha^n \phi^{f2} n (N_1^n - n) \quad (3.9)$$

where  $n$  is the endothelial concentration,  $D^n$  is diffusion coefficient of endothelial cells,  $\chi^n(c)$  is chemotactic coefficient which is proportional to the concentration of TAF,  $h^n$  is haptotactic coefficient,  $f$  is the concentration of FF,  $\alpha^n$  is the proliferation coefficient and  $N_1^n$  is a concentration threshold of endothelial cells.

#### Transforming Angiogenic Factors

After the secretion of the TAFs by the inflammatory cells, they diffuse into the direction of the implant surface and form a concentration gradient between the implant and the host bone.

$$\frac{\partial}{\partial t}(\phi^f c) = D^c \phi^f \Delta c + q^{f/s} \cdot c - \lambda^c \phi^{f2} n c \quad (3.10)$$

where  $c$  is the TAF concentration,  $D^c$  is the TAF diffusion coefficient and  $\lambda^c$  is the uptake and binding rate by other cells,  $q^{f/s}$  is the fluid flux.

#### Fibronectin factor

In addition to the existing FF tissue, it is also secreted by endothelial cells (see equation (3.9)). The reaction-diffusion equation for FF population is:

$$\frac{\partial}{\partial t}(\phi^f f) = D^f \phi^f \Delta f + \phi^f (\omega^f n - \mu^f \phi^f n f) \quad (3.11)$$

where  $f$  is FF concentration,  $D^f$  is FF diffusion coefficient,  $\omega^f$  and  $\mu^f$  are the secretion and uptake factors, respectively.

#### Osteoblasts population

The mechanical deformation of porous medium is considered in the conservation equation of osteoblasts. This equation is a convection-diffusion-reaction equation.

$$\frac{\partial}{\partial t}(\phi^f J \cdot C^0) = \mathbf{q}^0 + \Omega^0 \quad (3.12)$$



### 3 Interaction between electrical components and cells

where  $C^0$  is osteoblasts population,  $J$  is mechanical deformation of porous medium,  $\mathbf{q}^0$  is the flux of osteoblasts and  $\Omega^0$  is the reactive term, which involves proliferation and cell decay rate.

#### Anabolic growth factor

The evolution of anabolic growth factor population includes diffusion and convective fluxes. The consumption of production of anabolic growth factor are modeled by the source term  $\Omega^g$ .

$$\frac{\partial}{\partial t}(\phi^f C^g) = D^g \phi^f \Delta C^g + \mathbf{q}^{f/s} \cdot \nabla C^g + \Omega^g \quad (3.13)$$

where  $C^g$  is the anabolic growth factor,  $D^g$  is the diffusion coefficient of anabolic growth factors (AGF),  $\mathbf{q}^{f/s}$  is the fluid flux and  $\Omega^g$  is the reactive term.

#### Osseous matrix

The osseous matrix is synthesized by osteoblasts under the stimulation of growth factors. Osseous matrix is modeled as follows:

$$\frac{\partial}{\partial t}(J\phi^s) = \alpha^s \phi^{f2} C^0 (C^g - C_p^g) \quad (3.14)$$

where  $\phi^s$  is the osseous matrix,  $\alpha^s$  is a coefficient of the matrix synthesis,  $C_p^g$  is a threshold of the population of the growth factor  $C^g$ .

The set of continuous governing equations associated with boundary conditions, biological parameters and initial conditions were implemented into COMSOL Multiphysics<sup>®</sup> and solved using a spatio-temporal finite element method. The numerical results are validated using a reference experimental implant (canine micromotion implant) developed within the framework of an international collaboration (K. Sballo - Denmark, J.E. Bechtold - USA). Further details are described in [123].

The following diagram summarizes the pathways and the interactions between the different cells.

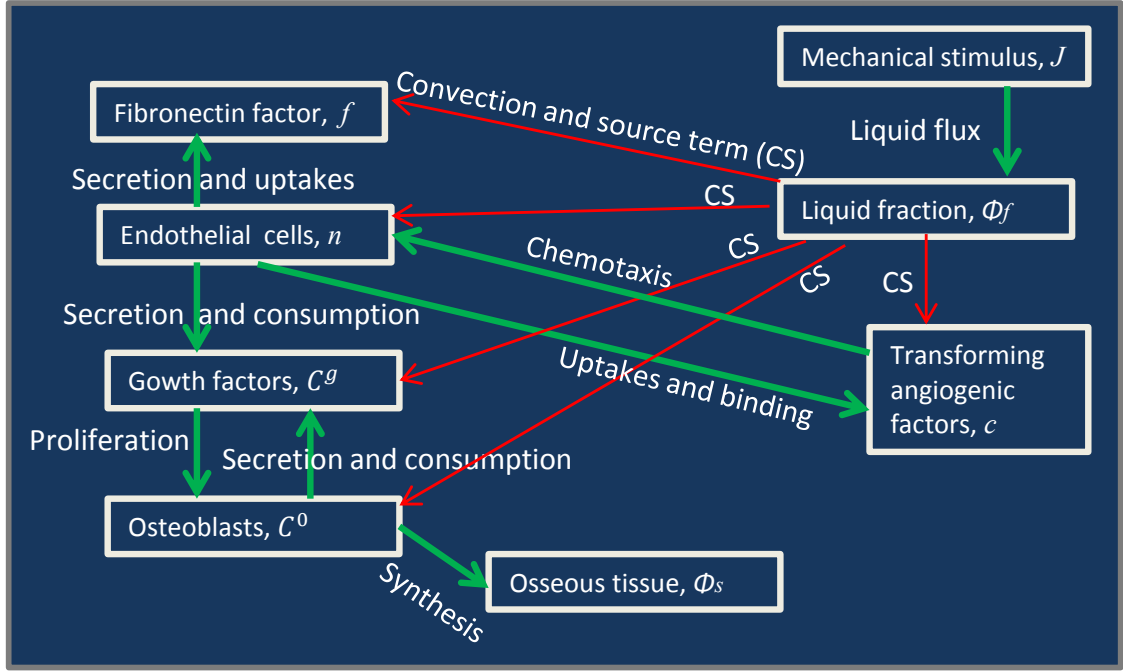


**Figure 3.3:** Diagram representing the main elements considered in the mathematical model of George Khalil et al. and their interactions.

### 3.1.4 Reaction-diffusion model by Pedro Moreo

The second model by Pedro Moreo et al. [2] takes into account the influence of implant surfaces roughness. The variables of the model are: Platelets, osteogenic cells, osteoblasts, generic growth factor 1, generic growth factor 2, fibrin network volume fraction, woven bone volume fraction, lamellar bone volume fraction and the implant surface roughness (surface roughness is described as a constant that influences the adsorption of proteins on the implant surface). Porosity is not considered in this model. Osteoblasts are assumed to remain on the surface of the bone matrix and therefore they have no flux (see equation (3.17)). Platelets are considered in this model instead of endothelial cells.

The mathematical formulations of the state variables of the system are:

#### Platelets

The temporal evolution of platelets is composed by the diffusion, taxis and source term. In the taxis term the platelets move toward the proteins which are attached to the implant surface.

$$\frac{\partial C}{\partial t} = [D_C \ C \ H_c C \ p] \ A_c C \quad (3.15)$$

### 3 Interaction between electrical components and cells

where  $C$  is the concentration of platelets cells,  $D_c$  is a linear diffusion coefficient,  $H_c$  is a constant,  $p$  is the concentration of protein,  $A_c$  is a decay rate.

#### Osteogenic cells

Osteogenic cells temporal evolution is governed by equation 3.16, where source, diffusion and convective terms are considered.

$$\frac{\partial m}{\partial t} = [D_m m - m(B_{m1} s_1 + B_{m2} s_2)] + f(s_1, s_2) - g(s_1) - A_m m \quad (3.16)$$

where  $m$  is the concentration of osteogenic cells,  $D_m$  the linear diffusion coefficient of  $m$ ,  $B_{m1}$  and  $B_{m2}$  are chemotaxis coefficients,  $s_1$  and  $s_2$  are concentrations of growth factors,  $f(s_1, s_2)$  is a proliferation term and it is a function of the dependence on  $s_1$  and  $s_2$ ,  $g(s_1)$  is the differentiation term influenced only by  $s_1$ ,  $A_m m$  is decay term.

#### Osteoblasts

In this model, osteoblasts are considered to remain on the surface of the bone matrix and therefore its conservation equation has only a source term.

$$\frac{\partial b}{\partial t} = g(s_1) - A_b b \quad (3.17)$$

where  $b$  is the concentration of osteoblasts and  $A_b b$  is the source term and here it represents the differentiation of osteoblasts to osteocytes.

#### Generic growth factors 1

Generic growth factors 1 is secreted by activated platelets. Their main role is to promote osteoblasts.

$$\frac{\partial s_1}{\partial t} = [D_{s1} s_1] + h(s_1, C) - A_{s1} s_1 \quad (3.18)$$

where  $s_1$  is the concentration of generic growth factor 1,  $D_{s1}$  is the diffusion coefficient of  $s_1$ ,  $h(s_1, C)$  is the secretion term of  $s_1$  by activated platelets,  $A_{s1} s_1$  is the decay rate of  $s_1$

#### Generic growth factors 2

Generic growth factors 2 is secreted by osteoblasts and osteogenic cells. Their main roles are to increase the proliferation of osteogenic cells and stimulate the production of woven bone.

$$\frac{\partial s_2}{\partial t} = [D_{s2} s_1] h(s_2, m, b) - A_{s2} s_2 \quad (3.19)$$

where  $s_2$  is the concentration of generic growth factor 2,  $D_{s2}$  is the diffusion coefficient of  $s_2$ ,  $h(s_2, m, b)$  is the secretion term of  $s_2$ , mainly secreted by osteoblasts  $b$  and osteogenic cells  $m$ ,  $A_{s2} s_2$  is the decay rate of  $s_2$ .

#### Fibrin network volume fraction

At the initial state the fibrin network volume fraction equals to one and it decreases gradually till it reaches zero.

$$\frac{\partial \nu_f}{\partial t} = -\tau(s_2) b \nu_f (1 - \nu_w) \quad (3.20)$$

### 3 Interaction between electrical components and cells

where  $\nu_f$  is fibrin network volume fraction,  $\nu_w$  is the woven bone volume fraction. The term  $\tau(s_2)b$  represents the production of the woven bone by osteoblasts under the stimulus of growth factor  $s_2$ .

#### Woven bone volume fraction

The fibrin network volume fraction is transformed to woven bone. The latter is remodeled to lamellar bone.

$$\frac{\partial \nu_w}{\partial t} = \tau(s_2)b\nu_f(1 - \nu_w) - \gamma\nu_w(1 - \nu_l) \quad (3.21)$$

the first term is described above, the second term represents the remodeling process of woven bone to lamellar bone.

#### Lamellar bone

At the end of the remodeling process, the woven bone is remodeled to lamellar bone.

$$\frac{\partial \nu_l}{\partial t} = \gamma\nu_w(1 - \nu_l) \quad (3.22)$$

The following diagram summarizes the pathways and the interactions between different cells involved in peri-implant healing.

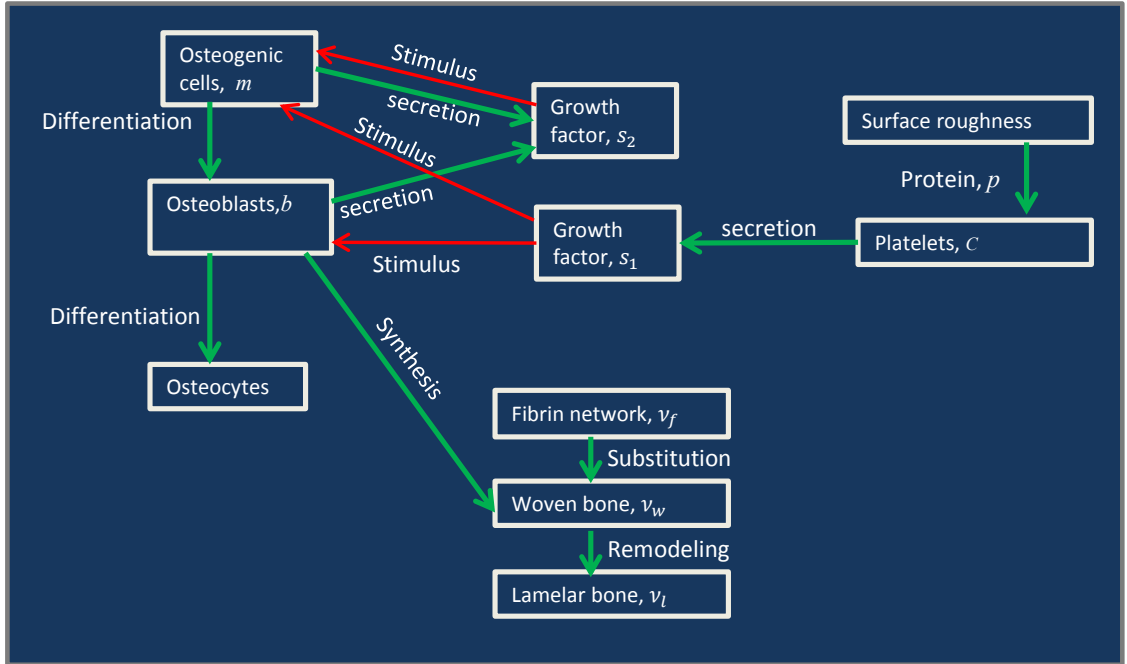


**Figure 3.4:** Diagram representing the main elements considered in the mathematical model of Pedro Moreo et al. and their interactions.

The following table summarizes the values of the parameters used in the numerical simulations, more details on the parameters could be found in [2].

### 3 Interaction between electrical components and cells

Parameter	Value	Parameter	Value
$D_c$	$1.365 \cdot 10^{-2}$ [mm <sup>2</sup> /day]	$A_b$	1.365 [day <sup>-1</sup> ]
$H_c$	0.333 [mm <sup>4</sup> /(day μg)]	$D_{s1}$	0.333 [mm <sup>2</sup> /day]
$A_c$	0.067 [day <sup>-1</sup> ]	$D_{s2}$	0.067 [mm <sup>2</sup> /day]
$D_m$	0.133 [mm <sup>2</sup> /day]	$A_{s1} = A_{s2}$	0.133 [day <sup>-1</sup> ]
$B_{m1}$	0.667 [mm <sup>2</sup> /day]	$\alpha_{c1}$	0.667 [ng/ml/day <sup>-1</sup> (cells/ml) <sup>-1</sup> mm <sup>2</sup> /day]
$B_{m2}$	0.167 [mm <sup>2</sup> /day]	$\alpha_{c2}$	0.167 [ng/ml/day <sup>-1</sup> (cells/ml) <sup>-1</sup> mm <sup>2</sup> /day]
$\alpha_{m0} = \alpha_m$	0.25 [day <sup>-1</sup> ]	$\alpha_{m2} = \alpha_{b2}$	0.25 [ng/ml/day <sup>-1</sup> (cells/ml) <sup>-1</sup> mm <sup>2</sup> /day]
$N$	$10^6$ [cells/ml]	$B_{c1}$	$10^6$ [μ/mm <sup>2</sup> ]
$A_m$	$10^{-3}$ [day <sup>-1</sup> ]	$B_{c2} = B_{m2} = B_{b2}$	$10^{-3}$ [ng/ml]
$\alpha_{mb}$	0.5 [day <sup>-1</sup> ]	$\alpha_w$	0.5 [day <sup>-1</sup> (cells/ml) <sup>-1</sup> mm <sup>2</sup> /day]
$B_m = B_{mb} = B_w$	10 [ng/ml]	$\gamma$	Determined from the numerical simulations

**Table 3.1:** The parameter values for platelets, osteogenic cells flux, osteogenic cells and osteoblasts kinetics, growth factors and bone formation.

Besides the physiological aspects of bone ingrowth on biomaterials, this model implements an important factor in the bone-implant healing process, which is the surface roughness.

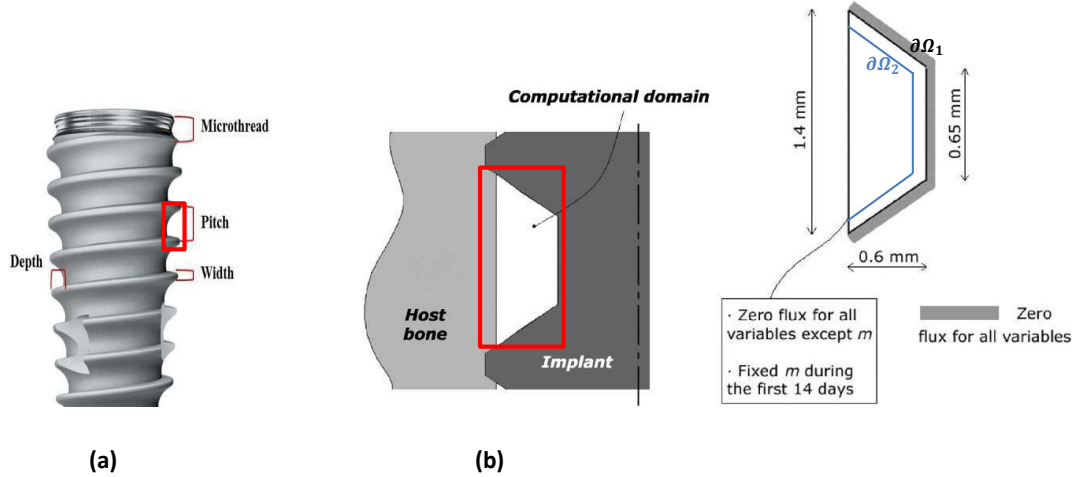


**Figure 3.5:** (a) Three dimensional dental implant (image from Neobiotech CMI IS-II active<sup>®</sup>). (b) Dimension of the computational domain implant-host bone cavity and the boundary conditions. Figure 3.5 is adapted and used with permission from [2].

We have used the model parameters presented in table 3.1 and the governing equations presented in subsection 3.1.4 to recreate the model and implement and solve it in COMSOL Multiphysics<sup>®</sup> version 5.1. In Pedro Moreo's model, the adsorbed protein distribution has been described as follows: At the rough implant surface, the protein concentration is equal to  $0.5 \mu\text{g}/\text{mm}^2$  at the surface, this represents domain  $\partial\Omega_1$ , and it equals to zero  $p = 0 \mu\text{g}/\text{mm}^2$  at a distance of 0.1 mm from the surface of the implant, this represents domain  $\partial\Omega_2$ . It was not mentioned how this distribution mathematically was modeled. We have considered the following system to model

### 3 Interaction between electrical components and cells

the protein distribution.

$$\begin{aligned} (\nabla \cdot p) &= 0 \\ p &= 0.5 \mu\text{g}/\text{mm}^2 \quad \partial\Omega_1 \\ p &= 0 \mu\text{g}/\text{mm}^2 \quad \partial\Omega_2 \end{aligned} \quad (3.23)$$

These formulations allow us to model a constant gradient of the proteins between domain  $\partial\Omega_1$  and  $\partial\Omega_2$ .

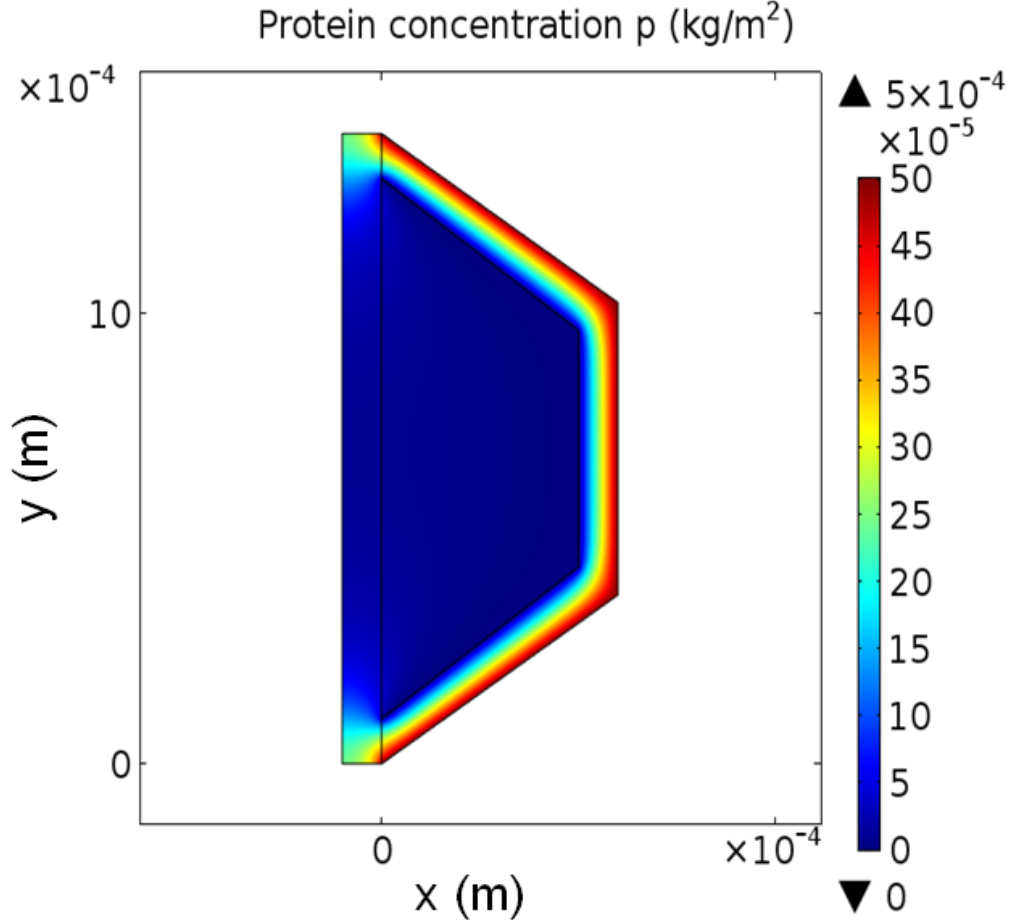


**Figure 3.6:** Concentration  $p$   $\text{kg}/\text{m}^2$  of the adsorbed proteins in case of an implant with rough surface.

From the simulation results (see figure 3.6) we can observe a linearly decreasing concentration of proteins  $p$  from  $0.5 \mu\text{g}/\text{mm}^2$   $\partial\Omega_1$  to  $0 \mu\text{g}/\text{mm}^2$   $\partial\Omega_2$ . This first model variable, proteins  $p$  is static. Among the transient states of the model we have implemented the platelets  $C$  and growth factors  $S_1$ .

Although there is a slight difference in the distribution of growth factors  $S_1$  between our simulations and the model from Pedro Moreo and its results (see figure 3.7), we can observe that both results show a high concentration of growth factors at

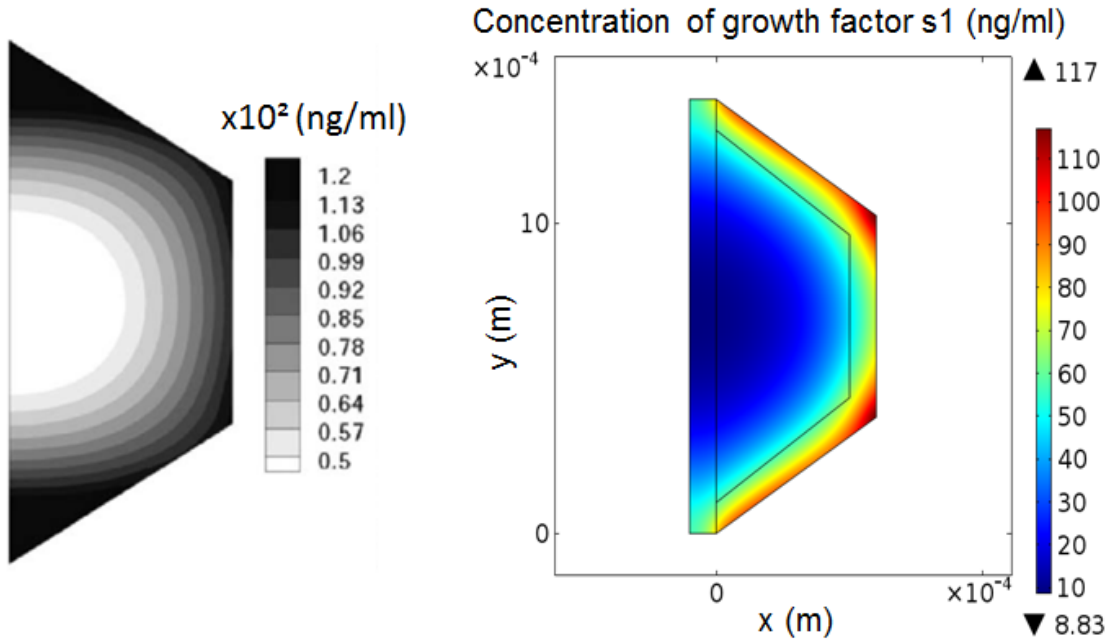


**Figure 3.7:** Distribution of the concentration of growth factor S1 after 14 days in case of a rough surface. The left and right figure show the results from Pedro Moreo’s model and our simulation result, respectively. Left figure is used with permission from [2].

the surface of the implant and low concentration near the host bone, after 14 days. Besides, the values fall in the same range. The reason for this slight difference is the different method that we used to model the protein  $p$  concentration which became necessary due to lacking information in the publication by Pedro Moreo et al., the second reason could be the implementation of the initial conditions (initial concentration of platelets, dimension of the domain which contains initial concentrations).

### 3.2 Effect of electrical stimulation on cells

The effect of the electrical stimulation on cells has been studied by many scientists. In their studies they have observed the behavior of the cells under different electrical stimulations. Alignment, elongation and migration of different kinds of cells were investigated. In the following table, some results of the interactions of different kinds of cells under electrical stimulations are presented, DC voltages are used [131].

### 3 Interaction between electrical components and cells

Cell type	Direction of migration	Electric field strength $E$ [V/m]	Velocity [ $\mu\text{m}/\text{h}$ ]
Articular chondrocytes	Cathode	600	13.74
Anterior cruciate ligament	Cathode	600	15
Osteoblasts	Cathode	100 – 1000	3 – 32
Osteoclasts	Anode	100 – 1000	72 – 140
3T3 fibroblasts	Cathode	60 – 600	10 – 22
Prostate cells [132]	Cathode	100	0.017
Keratinocytes	Cathode	100	48
Primary bovine and human	Anode	200	4.5
Neuronal stem/progenitor cells	Cathode	50–450	9–16

**Table 3.2:** Interactions of different kinds of cells under direct currents stimulation [131].

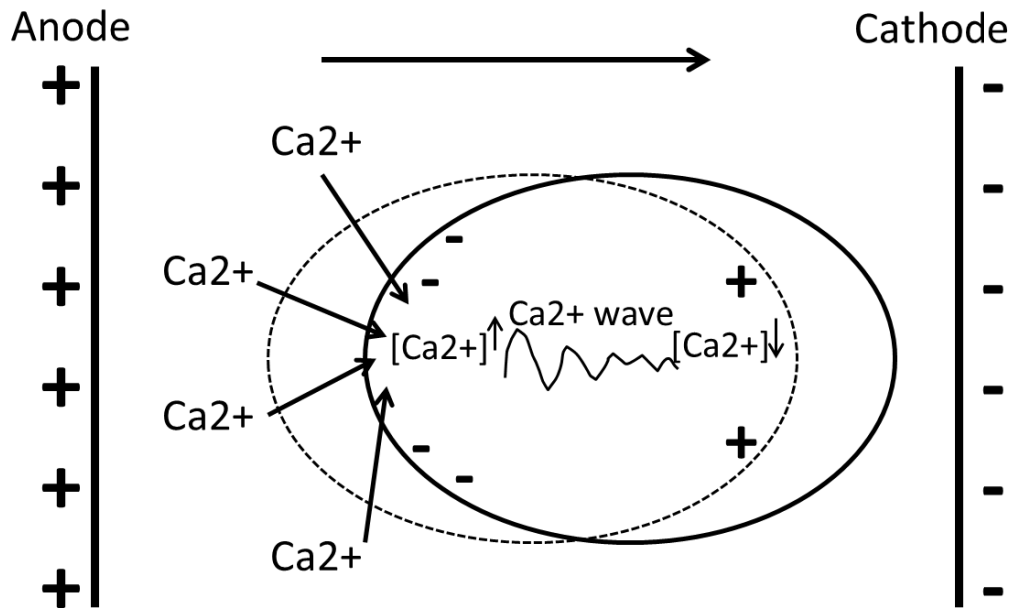


**Figure 3.8:** Response of a cell to electrical stimulation in case of negligible voltage-gated conductance of the cell membrane. The figure is adapted and used with permission from [3].

The mechanism of how cells sense and respond to external electrical stimulation is not well comprehended yet. Different types of cells respond to external electrical stimulation differently. This suggests that the effect of external electrical stimulation is dependent on the cell type. A recent study done by Mycielska et al. [3] explains how cells respond to DC voltages. The cell membrane is negatively charged in the resting state. When it is exposed to DC stimulus, in the case where voltage-gated  $\text{Ca}^{2+}$  channels are neglected, the cell membrane opposite to the anode hyperpolarizes and attracts  $\text{Ca}^{2+}$ . Near the anode, the intracellular level of  $\text{Ca}^{2+}$  is rising. The cell contracts at this side. The intracellular  $\text{Ca}^{2+}$  wave starts from the anode side. The other part of the membrane opposite to the cathode depolarizes.  $\text{Ca}^{2+}$  will flow out of the cell toward the cathode. The influx and efflux of  $\text{Ca}^{2+}$  leads to push-pull



effects, causing the directional movement of cells towards the cathode, see figure 3.8.

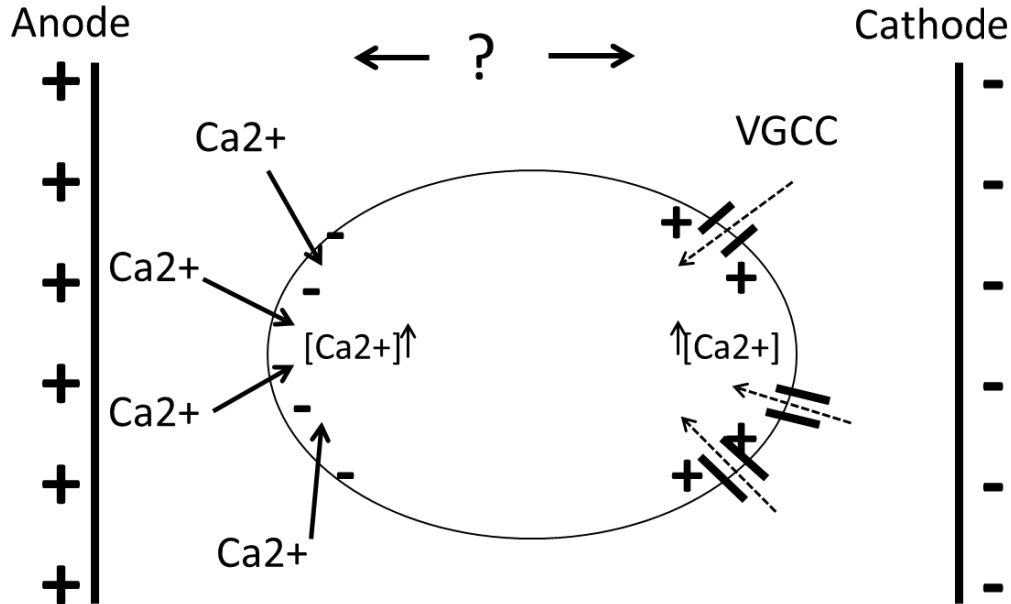


**Figure 3.9:** Response of a cell to electrical stimulation in case of voltage-gated conductance of the cell membrane. The figure is adapted and used with permission from [3].

In the other case where the voltage-gated  $\text{Ca}^{2+}$  channels are not neglected, see figure 3.9, the intracellular level of  $\text{Ca}^{2+}$  is rising on both sides, the anode and cathode side. The direction of cell movement is the direction of the resulting force applied in both directions. It has been reported that an applied DC electric field of 10 to 100 mV/mm across a cell of 10  $\mu\text{m}$  diameter causes the anode and cathode side of the membrane to hyperpolarize and depolarize successively by 5 mV. Furthermore,  $\text{Ca}^{2+}$  influx and efflux has also effects on cell adhesion. The probability of the cell to attach is higher in those parts where the  $\text{Ca}^{2+}$  concentration is decreasing and to detach where it is rising [3].

### 3.3 Mathematical modeling of cell sensing strategies

In this part, different types of partial differential equations (PDE) are derived based on the cell sensing strategies. These equations are time dependent second order PDEs. The mathematical formulations presented in this section have been developed by J. Painter et al [133] and they are based on five different sensing strategies strictly local, neighbour based, local average, gradient based and mixed based. We will use these strategies to derive the model equation of cells under electrical stimulation.

### 3.3.1 Cell response strategies to environmental cues

Understanding the different strategies which cells use to sense their surrounding environment may help to improve the modeling of its response. More details of the cell population modeling introduced in this section can be found in [133].

**Strictly local models** A strictly local model is called strictly local because the movement of cells is based on the information only provided at the local position. The model equation is a diffusion equation describing the transient behaviour of the cell concentration  $u$  :

$$\frac{\partial u}{\partial t} = D \frac{\partial^2 u}{\partial x^2} f(q) \quad u, \quad (3.24)$$

where  $u$  is the concentration of cells. For this kind of models the cells have the ability to sense only their local site.

**Neighbor based** In neighbor-based models the cells interact with the information presented at their neighboring sites. The local information is assumed to be not important for this model. The model equation can be mathematically written as:

$$\frac{\partial u}{\partial t} = \frac{\partial}{\partial x} \left[ g(q) \frac{\partial u}{\partial x} - u \frac{\partial g(q)}{\partial x} \right], \quad (3.25)$$

where  $g$  is a function of the external information  $q$  and  $u$  is the concentration of cells.

**Local average** The local average model considers the average information at the local site and at the neighboring site. The model equation is presented mathematically as:

$$\frac{\partial u}{\partial t} = \frac{\partial}{\partial x} \left( h(q) \frac{\partial u}{\partial x} \right), \quad (3.26)$$

where  $h$  is a function of the external information  $q$  and  $u$  is the concentration of cells. The type of the function  $h$  depends on the behavior of the cell population under the effect of the external information  $q$ .

**Gradient-based models** The gradient-based model takes into account that the cells sense the local difference in information between the neighboring and their present site. It can be interpreted mathematically as:

$$\frac{\partial u}{\partial t} = \frac{\partial}{\partial x} \left[ D \frac{\partial u}{\partial x} + u \frac{\partial \tau}{\partial q} \frac{\partial q}{\partial x} \right], \quad (3.27)$$

where  $D$  is diffusion coefficient and  $\tau$  is a function of the external information  $q$ . These kinds of models are widely used in chemotaxis, haptotaxis and phototaxis.

**Mixed models** The mixed models combine all the four strategies. The model equation is:

$$\frac{\partial u}{\partial t} = \frac{\partial}{\partial x} \left[ g(q) \frac{\partial}{\partial x} (f(q)u) - f(q)u \frac{\partial g(q)}{\partial x} + ug(q)f(q) \frac{\partial \tau}{\partial q} \frac{\partial q}{\partial x} \right], \quad (3.28)$$

where  $g$ ,  $f$  and  $\tau$  are functions of the external information  $q$ . For a simple model, these functions have the following forms:  $g = 1 - \frac{q}{T}$ ,  $\frac{\partial \tau}{\partial q} = \chi$  and  $f = \gamma q$ , where parameters  $T$ ,  $\chi$  and  $\gamma$  are constants.

These models will be used in chapter 4 and 5 to couple the electrical stimulation component generated by electro-stimulating systems with a population of bone cells. The surrounding information  $q$  will be replaced by the external electrical components.

### 3.4 Maxwell's equations for electrical stimulation at low frequency

This section gives a summary of Maxwell's equations, more detail are described in the book by Ursula van Rienen [18]. Maxwell's equations describe the coupling of time-varying electric and magnetic field and also their propagation and interaction with materials. Today they are written in the form of a coupled system of four partial differential equations. James Clerk Maxwell mainly unified the work of Michael Faraday, André -Marie Ampère and Carl Friedrich Gauss. He generalized Faraday's law of induction, see equation (3.31). He also added the displacement current density to Ampère's law, so that the variation in the electric field can also produce magnetic field, see equation (3.32). Maxwell's equations in differential form can be written as follows:

Gauss's law

$$\mathbf{D} = \rho \quad (3.29)$$

Gauss's law for magnetism

$$\mathbf{B} = 0 \quad (3.30)$$

Faraday's law of induction

$$\mathbf{E} = - \frac{\partial \mathbf{B}}{\partial t} \quad (3.31)$$

Ampère's law with Maxwell's addition

$$\mathbf{H} = \frac{\partial \mathbf{D}}{\partial t} + \mathbf{J} \quad (3.32)$$

where  $\rho$  is the electric charge density, and  $\mathbf{J}$  is the electric current density,  $\mathbf{E}$  and  $\mathbf{H}$  are the electric and magnetic field strength,  $\mathbf{D}$  and  $\mathbf{B}$  are the corresponding flux densities.

### 3 Interaction between electrical components and cells

In the linear materials the displacement  $\mathbf{D}$  and magnetic flux density  $\mathbf{B}$  are defined by the constitutive material equations

$$\mathbf{D} = \epsilon \mathbf{E} \quad (3.33)$$

$$\mathbf{B} = \mu \mathbf{H} \quad (3.34)$$

where  $\epsilon$  and  $\mu$  are the relative permittivity and the permeability of the material.

#### 3.4.1 Steady-state electric currents

Steady-state electric currents exist in conductors where constant electric potential difference is applied. The steady-state electric currents are described as follows [134]:

$$\mathbf{J}_L = 0 \quad (3.35)$$

$$\mathbf{E} = 0 \quad (3.36)$$

where  $\mathbf{J}_L = \sigma \mathbf{E}$  is the conduction current density and  $\sigma$  is the electric conductivity of the material. Equation (3.35) gets:

$$(\sigma \mathbf{E}) = 0 \quad (3.37)$$

Thus since the electric field  $\mathbf{E}$  is curl-free (irrotational), the following solution ansatz is valid

$$\mathbf{E} = -\nabla \phi \quad (3.38)$$

where  $\phi$  is the (scalar) electric potential. Considering equation (3.38), equation (3.37) transfers to

$$(\sigma -\nabla \phi) = 0 \quad (3.39)$$

in case that the conductivity is constant we arrive to Laplace equation:

$$\Delta \phi = 0 \quad (3.40)$$

where the Laplace operator in three dimensional Cartesian coordination equals to  $\Delta = \nabla^2 = \left[ \frac{\partial^2}{\partial x^2}, \frac{\partial^2}{\partial y^2}, \frac{\partial^2}{\partial z^2} \right]$

## 3.5 Coupling reaction-diffusion equations with electrical stimulation

Previous studies [2] and [123] have used reaction-diffusion systems to model bone ingrowth on implants without considering the electrical stimulation. We have derived

### 3 Interaction between electrical components and cells

similar models to include the effect of electrical stimulation produced by electro-stimulating implants.

Based on sensing strategies of cells presented in subsection 3.3.1, one can determine the reaction-diffusion equation of cells under electrical stimulation (ES). If we consider the gradient-based model, which means that the cells have the ability to sense the gradient of their local site and the neighboring site, the general equation results as:

$$\frac{\partial C}{\partial t} = (D \nabla \cdot (C + Cg(ES)p \nabla (ES))) + f(C, ES) \quad (3.41)$$

where  $D$  is diffusion coefficient,  $p$  is a directness parameter depending on the cell type. It takes the value 1 if the cell has the property to move against the gradient of the ES and -1 in the opposite case,  $C$  is the cell concentration,  $\nabla (ES)$  is a function that describes the sensing of cells to the gradient of  $ES$  with a certain sensitivity function  $g(ES)$ , is similar to the chemotactic sensitivity function in the Patlak-Keller-Segel (PKS) model [135],  $f$  is the source function. If we assume that the cells can sense the gradient of the potential, in this case our environmental cue  $ES$  equals the electric potential  $\phi$ . Then, the general model equation transforms to

$$\frac{\partial C}{\partial t} = (D \nabla \cdot (C + Cg(\phi)p \nabla \phi)) + f(C, ES) \quad (3.42)$$

we observe in this equation the coupling between the reaction-diffusion equation and the electric potential.

Considering now the strictly local model, the general model equation can be written as

$$\frac{\partial C}{\partial t} = D \frac{\partial^2 C}{\partial x^2} s(ES) C + f(C, ES) \quad (3.43)$$

in this case the cell will sense only the electric stimulation at its local site.

Assuming that the cells are able to sense only its neighboring ES, the model equation leads to

$$\frac{\partial C}{\partial t} = \frac{\partial}{\partial x} (g(ES) C \frac{\partial C}{\partial x} + U \frac{\partial g(ES)}{\partial x} C) + f(C, ES) \quad (3.44)$$

If we consider the local average strategy of sensing, the ES will be coupled this way

$$\frac{\partial C}{\partial t} = \frac{\partial}{\partial x} (h(ES) C \frac{\partial C}{\partial x}) + f(C, ES) \quad (3.45)$$

Mixing all the strategies the model equation becomes

$$\frac{\partial C}{\partial t} = \frac{\partial}{\partial x} [g(ES) C \frac{\partial (s(ES)C)}{\partial x} + s(ES)C \frac{\partial g(ES)}{\partial x} + Cg(ES)s(ES)b \frac{\partial ES}{\partial x}] + f(C, ES) \quad (3.46)$$

Thus we have arrived at different coupled reaction-diffusion models for different strategies. Each model can be studied separately. The stationary electric potential

### *3 Interaction between electrical components and cells*

equation can be solved separately from the transient equation for the cell sensing. In the next sections we have used the model equation based on the gradient based model equation because it is widely used for modeling cell behavior toward external stimulations like in chemotaxis [133].

## 4 Determination of model parameters from *In vitro* studies

This chapter describes *in vitro* experiments that we have conducted in order to estimate the parameters of the gradient based model 3.42. The osteoblast-like cell line MG-63 and primary human osteoblasts cells are stimulated in an electro-taxis system. The interactions of the cells with the ES are then observed. Based on the quantification of the speed and direction of the migration of the cells, the sensitivity of the cells to the electric field and the direction of the migration parameters are estimated. Furthermore, the electric currents and the electric field inside the electro-stimulating system is modeled and simulated in the finite element based software COMSOL MULTIPHYSICS<sup>®</sup> version 5.1, the migration of cells under the effect of the electric field is then simulated. The temporal evolution of the osteoblasts is observed at the last part.

### 4.1 Experimental setup

Electro-taxis is a phenomenon by which the migration of cells is directed under the influence of the electric field [136]. Our electro-taxis system consists of a chamber made of PLA, spacers, culture medium, agar-bridges, Silver/silver chloride electrodes and a power supply to generate external electric current across the cells.

#### 4.1.1 Silver chloride coating preparation

Silver/silver chloride electrodes Ag/AgCl have been used widely in industry and research. It is an attractive alternative to scientists because it is simple to be constructed, contains non-toxic substances, and is very reasonable regarding manufacturing prices [137]. In electro-taxis experiments, they have been used as a reference electrodes in [138], [139], [140], [141], [142] and [143]. There exist several techniques to coat the silver electrodes with AgCl. Among them three well known techniques, electrochemical coating or electro-deposition [144], [145], [146], and [147], screen-printing [137] and [148], and sputter-deposition [149], [150] and [151]. Other methods are also used like plasma modification processes [152].

For our experiments, we have used the electrochemical coating technique, which is a general and simple method described in [153]. We have chloridized silver wires (99.99 % purity) using direct current electric field (dcEFs) generated by laboratory

#### 4 Determination of model parameters from *In vitro* studies

power supply (EA-PS 3032-20 B, EA-Elektro-Automatik GmbH & Co. KG, Viersen, Germany). Two silver electrodes are inserted inside a beaker, containing saline medium NaCl, then a voltage of 10 V is applied between the electrodes for 10 minutes. A layer of AgCl is growing gradually at the positive electrode (anode) with respect to the counter electrode. The following reactions take place at the surface anode/electrolyte [154]



which results in the complete reaction



A grey thin layer of AgCl is deposited on the silver electrode. The grey layer increases gradually. After 10 min we have removed the wires from the beaker. We have repeated the same experiments with two new silver electrodes, one is used as an anode and the other as a cathode like we have done before. The two prepared electrodes with the deposited grey layer (AgCl) are then used directly in the experiments. They are used as reference electrodes, where they are in direct contact with the medium, which is used to fill the outer reservoirs. Since there are no free electrons to carry charges in the medium, the current will be flowing by charged ions such as  $Cl^-$  and  $Na^+$  [155]. Figure 4.1 summarizes the setup used to prepare Ag/AgCl electrodes.

##### 4.1.2 Electro-taxis chamber construction

The customized electro-taxis chamber described in figure 4.2 is adapted from [132], where it has been used to stimulate prostate cell line pRNS-1-1 and PNT2. This is a well-established method to study dcEFs stimulations of cells [156], [157] and [158]. This kind of setup avoids electrode processes, i.e. electrochemical processes during the ES of the cells. The chamber has the dimensions of 50 x 87.5 cm. It is designed in AutoCAD 2014 and then exported as an STL file to the Ultimaker 2+ 3D printer software. The layer resolution is set to 0.4 mm nozzle. The 3D printer has a build volume of 223 x 223 x 205 mm, which allows printing more than one chamber at the same time, and build and travel speed up to 24 mm<sup>3</sup>s<sup>-1</sup> and 300 mm s<sup>-1</sup>, respectively. A support is also printed in order to ensure the stability of the chamber inside the time lapse microscopy. The printing time is about two hours. Several chambers are printed and tested till we have arrived to a good chamber that matches the dimensions of the spacers, support and the time lapse microscopy.



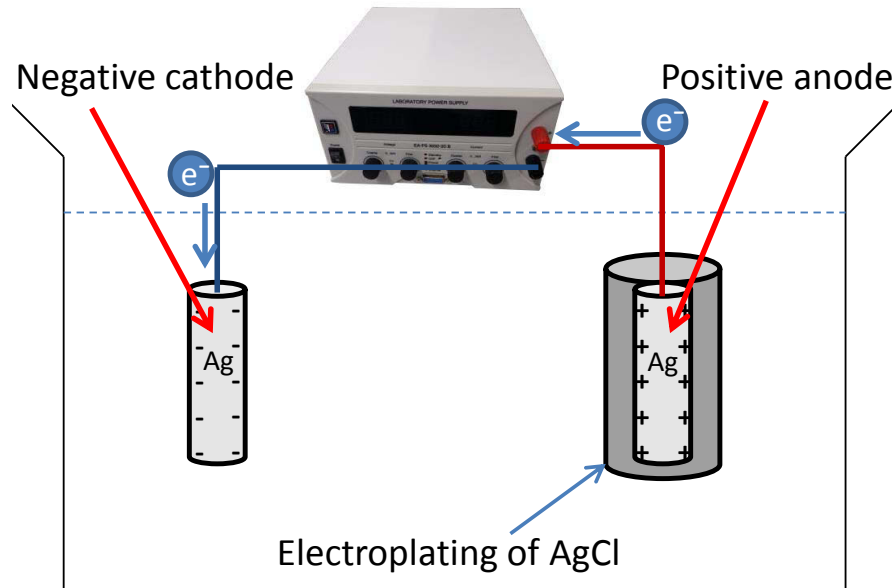


**Figure 4.1:** Electrodeposition of silver chloride AgCl on silver wire Ag. The equipments used for Ag/AgCl electrodes preparation are: Silver electrodes, beaker, saline medium, wires, crocodile clamp and power supply. A grey thin layer of AgCl is deposited on the Ag wires at the end of the preparation procedure for the electrodes.

The tubes and the chamber are made of poly-vinyl chloride (PVC) and polylactic acid (PLA), respectively. The chamber is sterilized. The tubes (presented with pink color in figure 4.3) are filled with 2 % agar gel. Agar bridges are used to conduct the current from the outer reservoirs to the inner reservoirs. The reservoirs are filled with culture medium. The circular openings facilitate the flow of current through the cells, which are seeded between the two inner reservoirs. The two prepared silver/silver chloride electrodes are placed in the outer reservoirs to provide adequate electric field strength between the two circular openings. The agar bridges are often used in electro-taxis experiments [132], [159], [160] and [161] to avoid direct contact of cells with the electrodes, which can cause pH change and cell contamination. Marina A1072 Silikonkleber transparent is used to glue the glass spacers to the electro-taxis chamber. The chamber is then soaked in distilled water for one night and subsequently it is dried. The cells are incubated for one night, and afterwards the unattached ones are removed. A voltage is applied between the electrodes to maintain certain electric field strength amplitude in the cell migration area. The experiments are conducted for a limited time depending on the applied voltage. This time limitation is because of the evaporation of water out of the medium during the experiments. A time-lapse microscope is used to track the cells movement. The pictures taken from the microscope are used to quantify the speed and orientation of cells.

4 Determination of model parameters from *In vitro* studies



**Figure 4.2:** 3D printed electro-taxis chamber (middle) and the corresponding support.  
The complete system is already in the bottom

#### 4 Determination of model parameters from *In vitro* studies

The following points summarize the main features of the *in vitro* experiments

- MG-63 cells P.18 in DMEM (Life Technologies) with 10 % FCS (Biochrom AG) and 1 % gentamycin (Ratiopharm)
- 2 % agarose (TopVision agarose, ThermoScientific, Waltham, MA, US) in Ringers solution (Braun, Melsungen, Germany)
- 25,000 cells cultured for 1 h in the electro-taxis chamber and then treated with Cell Light BacMam2.0 GFP Actin for 24 h
- Electrical stimulation; different values of voltages: 50, 100, 150, 200, 250 V
- 20x (EC Plan-Neofluar) objective (Carl Zeiss AG) under incubation at 30 C and 5 %  $CO_2$  in LSM 780 (Carl Zeiss AG)

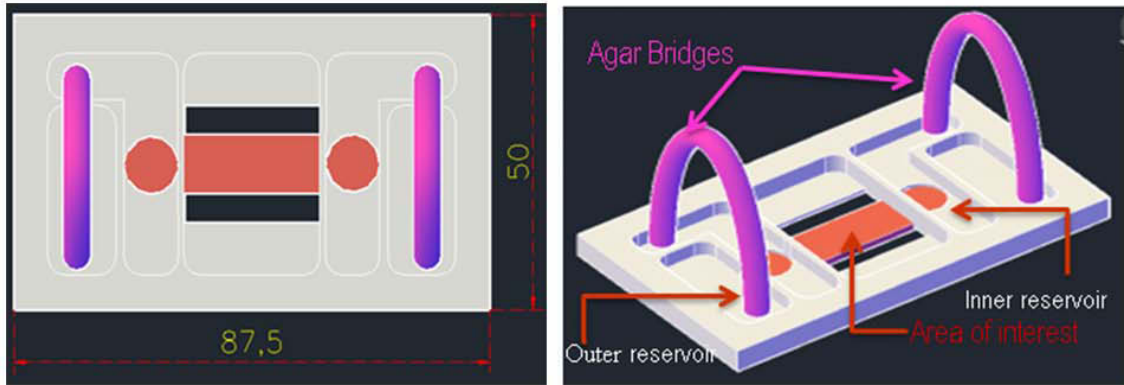


**Figure 4.3:** Electro-taxis chamber designed in AutoCAD 2014. The left figure shows a top-view of the electro-taxis chamber with dimensions in mm. The right figure shows a side-view of the same chamber, which mainly consists of agar bridges, polylactic acid (PLA) material, and culture medium.

#### 4.1.3 Voltage and pH measurements

Prior to the starting of the cell experiments, we have conducted some measurements of the voltage drop over time in order to investigate the effect of electrochemical reaction at the interface electrode/medium on the voltage stability. These kinds of measurements are important in order to ensure that the cells are stimulated with sufficiently high amplitude of the electric field strength during the cell experiments. We have used Analog Digital Multimeter TRMS-Multimeter C.A 5011 (Chauvin Arnoux, Kehl / Rhein, Germany) to measure the voltage between the both sides of the culture medium, see figure 4.5. The pH inside the area of interest is measured as well. The pH plays an important role in cell behavior. It is reported in [162]

#### 4 Determination of model parameters from *In vitro* studies

that an acidic pH of 6.8 increases the apoptosis of MG-63 cells. Another study [163] evaluated the osteoblasts function in Hepes-buffered medium at pH ranging from 6.8 to 8.2. They have concluded that the increase of pH values increases the glycolysis, collagen synthesis and alkaline phosphatase activity (AIPase).

The measurements presented here are conducted before culturing the cells because it would be not possible to do such measurements during cells experiments due to the coverage of the medium by cover slips. The obtained measurements are presented in table 4.1.

Time/Measurements	V0 [V]	V1 [V]	$\mathbf{E}$ [V/m]	$pH_i$	$pH_o$
0 min	15	0.56	22.4	8.30	8.30
30 min	15	0.56	22.4	8.39	8.49
90 min	15	0.56	22.4	8.49	7.79
150 min	15	0.53	21.2	8.41	8.39
210 min	15	0.45	18.0	8.41	6.49

**Table 4.1:** Results of the measured voltages and pHs. V0 and V1 are voltages measured between the electrodes and the circular opening, respectively.  $pH_o$  and  $pH_i$  are the measured pH values inside the outer reservoir and the area of interest, respectively (see figure 4.3).

From the results we can clearly see the benefits of the agar bridges. Almost a constant pH value is measured  $pH_i = 8.4$  in the area of interest, where the cells are cultured, which is not the case inside the outer reservoirs where the medium is in direct contact with the electrodes. After 210 minutes of applying a voltage of 15 V between the electrodes, the value of  $pH_o$  drops from 8.3 V to 6.49 V. We have also observed a drop of voltages between the circular openings from 0.56 V, in the initial state, to 0.45 V after 210 minutes. This small change is due to the growth of a resistive layer on the electrodes surface.

We have conducted some measurements to investigate the relationship between the applied voltage V0, and the obtained one V1. The following table shows the obtained results:

V0[V]	50	100	150	200	250
V1[V]	3	6	9	14	19
$\mathbf{E}$ [V/m]	120	240	360	560	760

**Table 4.2:** Relationship between output voltages V1, the input voltages V0 and the magnitude of the electric field strength  $\mathbf{E}$  inside the medium.

A function  $\mathbf{E} = f(V0)$  has been constructed, which takes V0 as an input and  $\mathbf{E}$  as an output, using curve fitting method. The polynomial  $f(V0)$  is of degree two, which provides a good fit to the monotonically increasing data. The coefficients for the polynomial  $f$  in descending power are 0.005333, 1.6 and 26.67. The corresponding

## 4 Determination of model parameters from *In vitro* studies

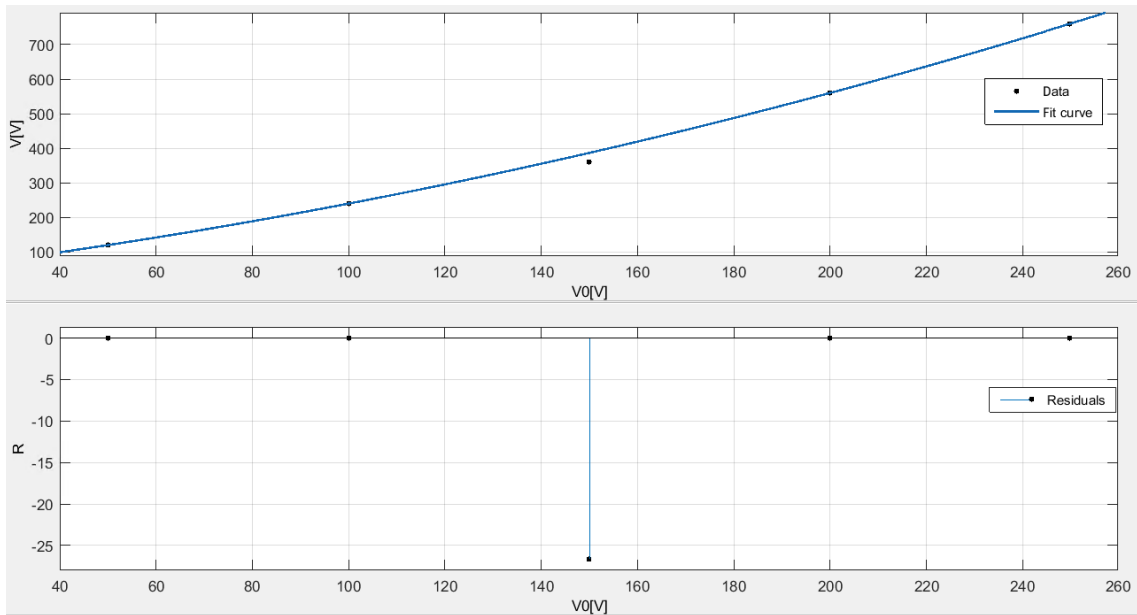


**Figure 4.4:** Curve fitting of the measured data. The upper plot shows the polynomial curves fitting points, the blue line is a second order polynomial. The lower plot shows a graphical display of the residuals relationship.

polynomial could be written as

$$\mathbf{E} = 0.005333 V_0^2 + 1.6 V_0 + 26.67 \quad (4.3)$$

In the curve Fitting Toolbox in MATLAB we have used the robust LAR (Least Absolute Residuals) method, which iterates through the function parameters until it minimizes the absolute difference of the residuals. The R-squared, which measures how well approximate the data are fitted to the polynomial, is equal to 0.9991. Together with the residual plot (see figure 4.4) we conclude that the polynomial presented in equation (4.3) provides a good approximation to the magnitude of the electric field  $\mathbf{E}$  given the input voltage  $V_0$ . This knowledge is important for predicting the measured electric field strength between the circular openings in case it is not possible to measure the electric field strength directly.

### 4.1.4 Accuracy in measurements

Accuracy in performing measurements is not only dependent on the accuracy of the measuring devices but also on the sensitivity of the mathematical formulation to describe the relationship between different measured quantities. In this part the measured quantities are the voltage  $V$  and the magnitude of the electric field strength  $\mathbf{E}$ .

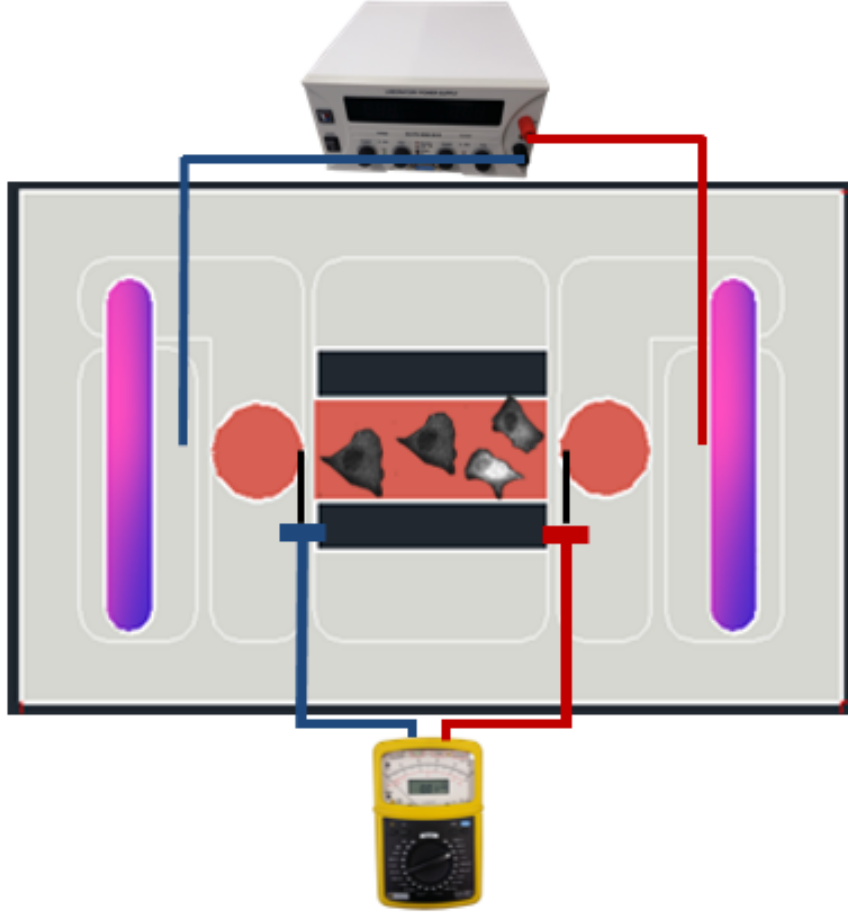


**Figure 4.5:** The used equipments for electro-taxis experiments. In addition to the electro-taxis chamber which has been described previously, we have used a multimeter to measure the voltage between the circular openings.

The magnitude of the electric field strength  $\mathbf{E}$  inside the culture medium, where the cells are cultured (see figure 4.5) is approximated as

$$\mathbf{E} = \frac{V}{d}, \quad (4.4)$$

where  $V$  is the measured voltage between the circular openings and  $d = 0.025$  m is the distance between them. Assuming an absolute error of  $\Delta V$  of voltage is made during the measurements, equation (4.4) would become

$$\mathbf{E}_{meas} = \frac{V + \Delta V}{d} \quad (4.5)$$

where  $\mathbf{E}_{meas}$  is the measured magnitude of the electric field strength. Equation (4.5) can be rewritten as

$$\mathbf{E}_{meas} = \frac{V}{d} + \frac{\Delta V}{d} \quad \mathbf{E}_{meas} = \mathbf{E} + \Delta E \quad (4.6)$$

#### 4 Determination of model parameters from *In vitro* studies

where  $\mathbf{E}$  is the exact value of the electric field strength. Substituting  $d = 0.025$  mm into  $\Delta \mathbf{E} = \frac{\Delta V}{d}$  we obtain

$$\Delta \mathbf{E} = 40\Delta V \quad (4.7)$$

To this extent, a measurement of a voltage of  $V = 10$  V with uncertainty of 1 V would result in an uncertainty of 40 V/m of the amplitude of the electric field strength. However, TRMS-Multimeter C.A 5011 has an accuracy about 0.5 %, which means a measurement of a voltage of  $V = 10$  V with this uncertainty of 0.5 % (0.05 V) leads to an uncertainty of 2 V/m of the amplitude of the electric field strength, which is tolerable for our application.

##### 4.1.5 Cell's observation

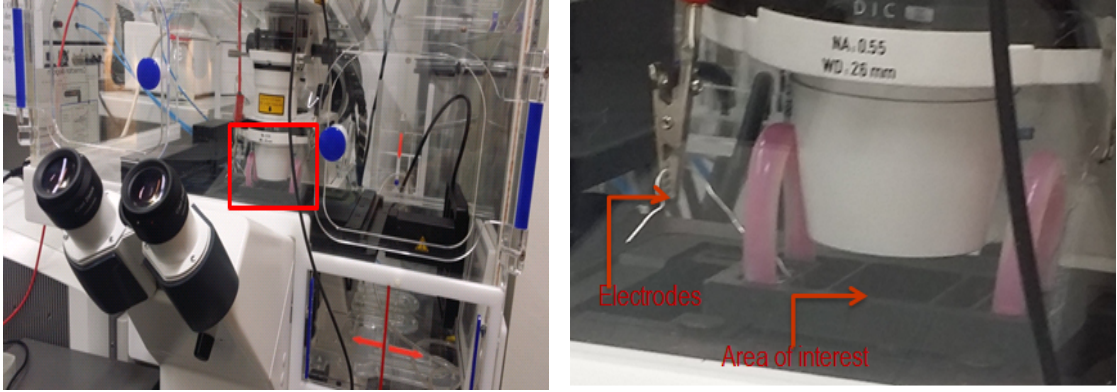


**Figure 4.6:** Electro-taxis chamber under time lapse microscopy, Carl Zeiss AG (Prof. Nebe Lab, Dept. of Cell Biology, Rostock University Medical Center).

In this part, some spatio-temporal evolution of the electro-stimulated MG-63 cells, which have been observed during the experiments, will be provided. A voltage of 50 V has been applied between the anode and the cathode. This voltage value results in an amplitude of the electric field strength of 120 V/m inside the culture medium. In other words, the MG-63 cells are stimulated with 120 V/m. After 90 min of ES we were not able to observe any change in cell morphology or motion (see figure 4.7). The setup has been checked and tested to ensure the current flow inside the electro-taxis chamber. The electro-taxis chamber has been taken out of the incubator (see figure 4.6), then all cable connections have been checked and voltages have been measured. After these tests, we could see that the electro-taxis chamber has been set up correctly. In the next step, we have performed the experiments somewhat longer for 120 min. Only a slight change of the cell shapes could be observed, see figure 4.7. These experimental results are not enough to be used as an input to estimate the parameters of the gradient model. The behavior of the MG-63 cells is passive. They

#### 4 Determination of model parameters from *In vitro* studies

have neither shown migration nor a change in orientation under the presence of the electric field.

We have performed further experiments to stimulate osteoblast-like cell line MG-63. The idea is to apply a higher stimulating voltage and to track more cells (by adjusting the zooming of the microscope), because some cells may respond to the ES but they could be outside of the scope since the zooming is relatively high, which may in turn decrease the probability to observe them. In other words, the higher the zoom, the lower the number of tracked cells. Thus, next a voltage of 150 V has been applied between the anode and the cathode which results in 360 V/m and we have reduced the zooming to a 10x objective.

From figure 4.8 we can observe that after 5 min, 60 min, 75 min, 90 min and 120 min of subjecting osteoblast-like cell line MG-63 to 360 V/m, cells retracted but did not elongate and did not move in the same or opposite direction with respect to the electric field. We have performed the experiments several times but we could not observe cell migration. Although the stimulation parameters that we have used are in the range reported in [164], we could not observe perpendicular or parallel alignment to the electric field vector within our first experiments described here. However the alignment of cells in response to DC stimulation has been reported many times in literature [165], [166], [167], [168] and [169]. In addition to passive alignment, elongation and migration of MG-63 cells are not observed as well in our experiments. This could be because the cells need more time to interact with the stimulating electric currents. Another reason could be the high concentration of cells which reduces the probability of cells to elongate and migrate due to limited space. The osteoblasts are laid directly on the cover glasses, which may inhibit their functionality since this differs from their situation in bone, where they lie on the surface of the extracellular matrix [170], which is rich of collagen [171]. In the next subsection we will try to mimic the *in vivo* environment of the cells by coating the cover glasses with collagen.



#### 4 Determination of model parameters from *In vitro* studies

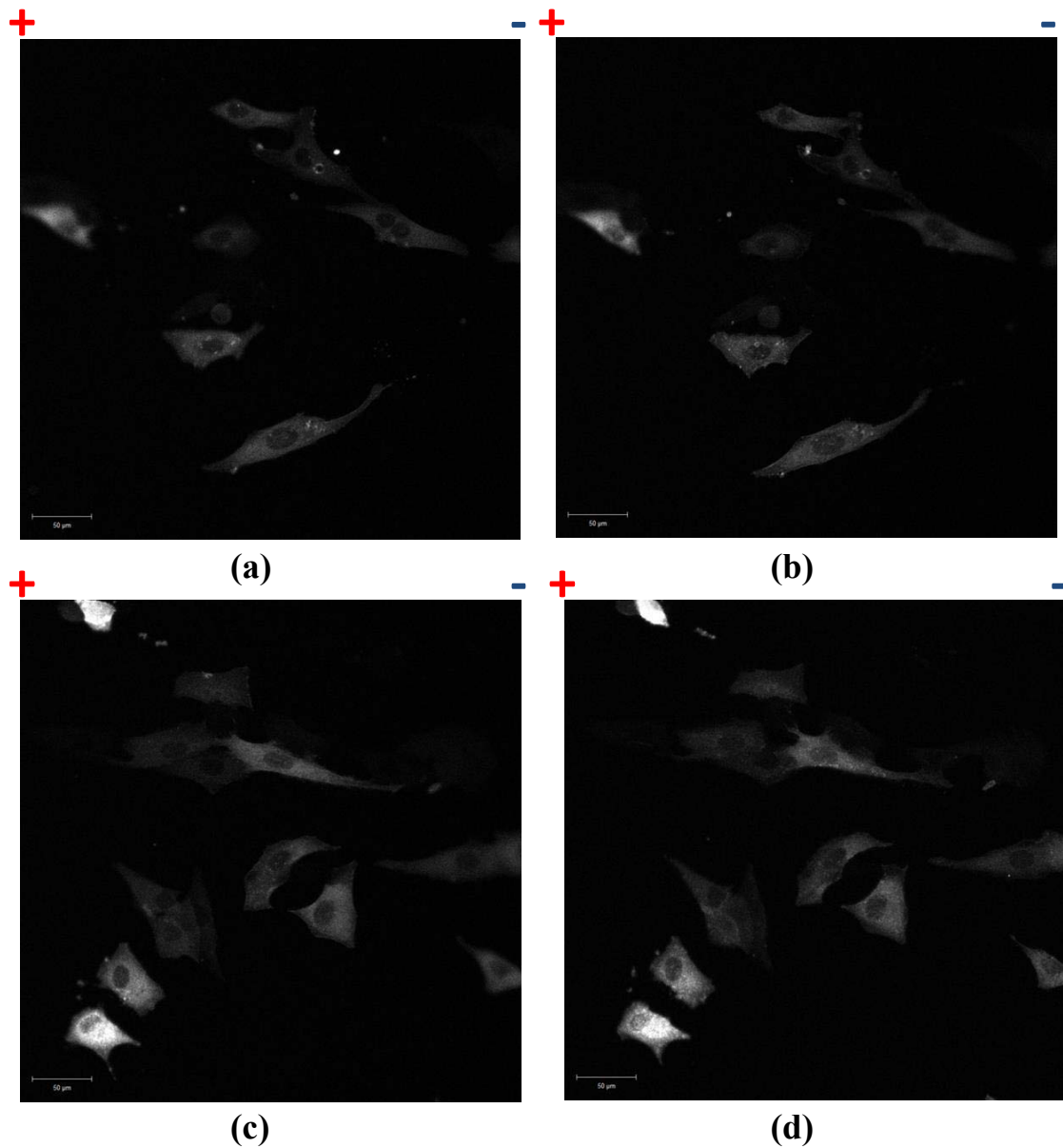


**Figure 4.7:** Visualization of osteoblast-like cell line MG-63 under time lapse microscopy (bars 50  $\mu\text{m}$ ). The cells are subjected to 120 V/m for 210 min. (a) cells in the initial or resting state, (b) after 90 min, (c) after testing and checking the cables connections and the voltage inside the culture medium, (d) after 210 min from the resting state. The signs + and - represent the location of the anode and the cathode, respectively. Figures are produced together with Caroline Mörke and Josefin Ziebert at Prof. Nebe Lab, Dept. of Cell Biology, Rostock University Medical Center.

4 Determination of model parameters from *In vitro* studies

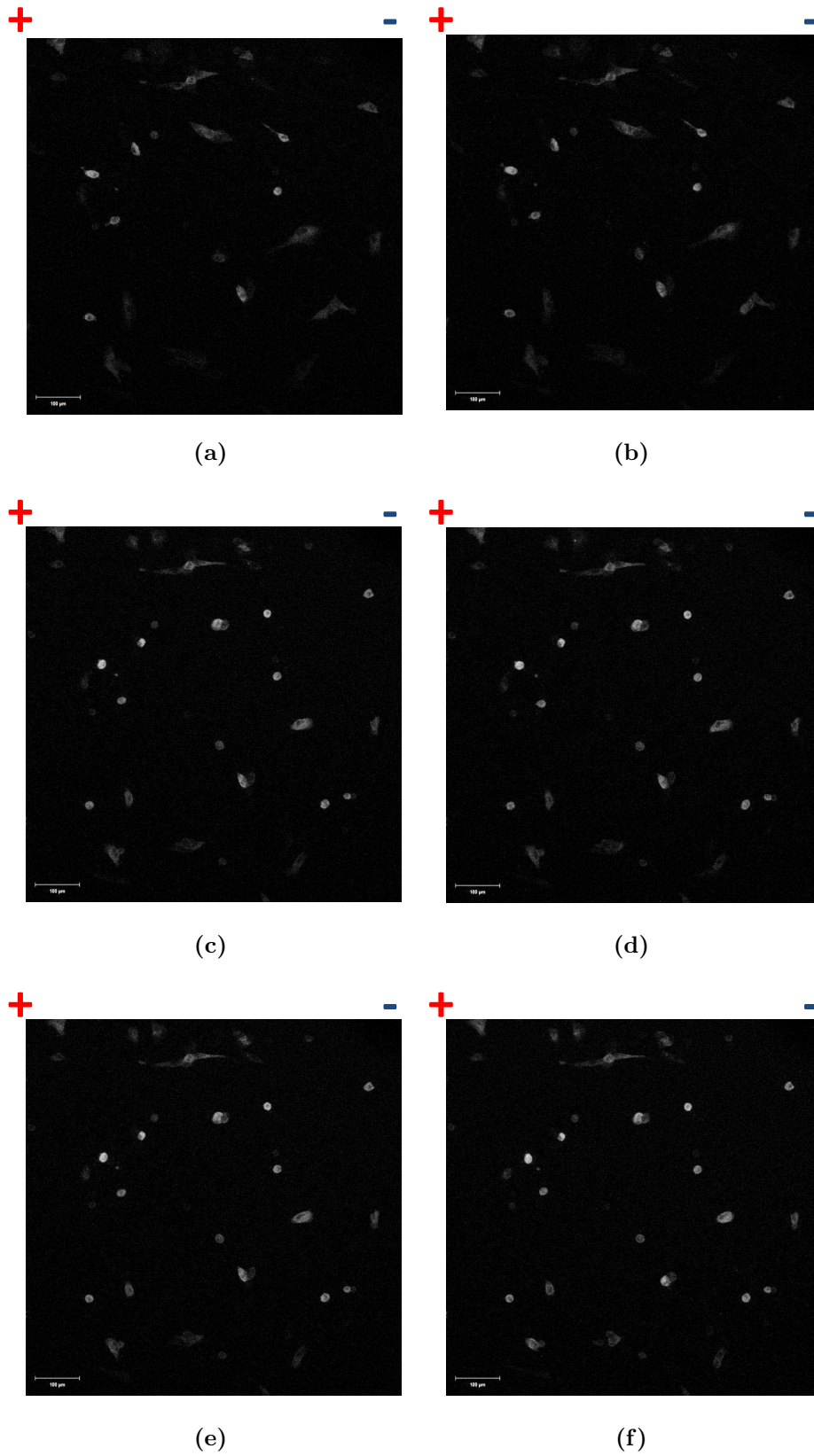


**Figure 4.8:** Visualization of osteoblast-like cell line MG-63 under time lapse microscopy (bars 100  $\mu\text{m}$ ). The cells are subjected to 480 V/m for 120 min. (a) control sample, (b) after 5 min, (c) after 60 min, (d) after 75 min, (e) after 90 min and (f) after 120 min<sup>3</sup>.

#### 4 Determination of model parameters from *In vitro* studies

**Modified electro-taxis chamber** Our previous electro-taxis chamber has some limitations. The experiments could be conducted for a maximum duration of two hours. We have collaborated with the Oscar Langendorff Institute of Physiology to extend our electro-taxis chamber. The modified electro-taxis chamber (see figure 4.9) is mechanically stable. It is made of PEEK (polyether ether ketone), which is a biocompatible material. The chamber has bigger reservoirs that can carry more medium. It is easy to handle and can be used for several times. Instead of using silicon glue, 12 screws are used to fix the upper and the bottom parts, this fixation prevents medium leakage. Experiments could be conducted up to 7 hours.

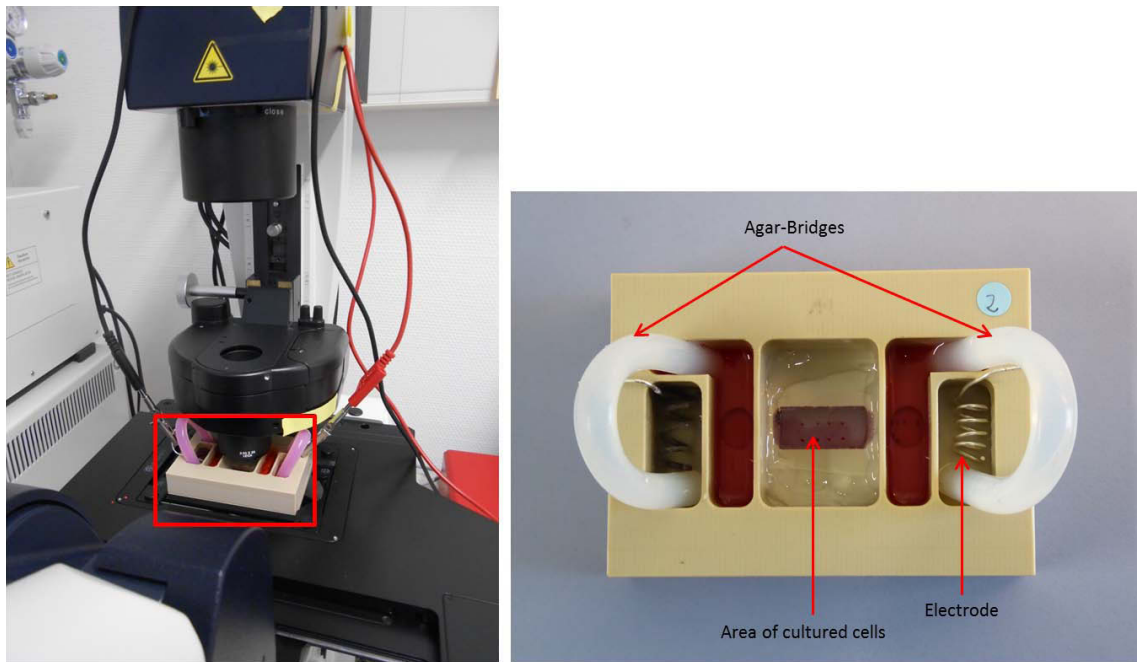


**Figure 4.9:** Modified electro-taxis chamber under Leica DMI 6000 microscope, (laboratory of Prof. Köhling Oscar Langendorff Institute of Physiology). Left figure shows the electro-taxis chamber integrated to the microscope and the power supply. Right picture illustrates the modified chamber with the electrodes, empty bridges, culture medium and cover glasses. The right figure is used with permission from [175].

We have performed further experiments on osteoblasts of the MG-63 cells, the experimental setup is summarized as follows

- MG-63 cells (osteosarcoma cell line) cultured in Dulbeccos Modified Eagle Medium (DMEM, Life Technologies) with 10 % fetal calf serum, 1 % amphotericin B, 1 % penicillin-streptomycin and 1 % hepes-buffer

<sup>3</sup>Figures are produced together with Caroline Mörke and Josefin Ziebert at Prof. Nebe Lab, Dept. of Cell Biology, Rostock University Medical Center.

#### 4 Determination of model parameters from *In vitro* studies

- 2 % agarose (TopVision agarose, ThermoScientific, Waltham, MA, US) in Ringers solution (Braun, Melsungen, Germany)
- Coverslips are coated with rat tail collagen (Advanced Biomatrix, San Diego, CA, USA)
- 15,000 cells are cultured over night in galvanotaxis chamber under standard cell culture conditions (5 % CO<sub>2</sub> and 37 C)
- Electrical stimulation: 60 V for 4 hr
- Photos taken with Leica DMI 6000 and LAS X software: 20x objective
- Image editing with ImageJ software
- The measured pH inside the culture medium before and after the experiments are 8.3 and 7.4, successively

The cells are subjected to a magnitude of electric field strength of  $E = 141.8 \text{ V/m}$ . This value is obtained from substituting  $V = 60 \text{ V}$  in equation (4.3). The experiments are conducted for four hours. The movement of the cells inside the microscope field is tracked using ImageJ. ImageJ is an open source tool, it has many features e.g. image processing and analysis [172]. We have selected 11 cells to be tracked. The results of the experiments are shown in figure 4.10.

A random movement of MG-63 cells is observed. However, a slight retraction of some cells (number 1 and 11) are noticed. The behavior of the cells toward the ES is not clear. Cells marked with numbers 3, 8, 11 show directional movement toward the anode. Cells marked with numbers 1, 4, 7, 9 show directional migration toward the cathode. However the direction of migration of cells marked with numbers 2, 5, 6, 10 is undirected or passive. This random migration of 11 tracked osteoblast-like cell line MG-63 in the same environmental conditions and observation field is not predictable. One reason could be that osteoblast-like cell line MG-63 needs longer time of ES to migrate. We do not have the facilities that allow us to perform further experiments for longer time. It is not possible to refill the reservoirs regularly because the shear forces might affect the cell behavior. The agar bridges have to be changed after some hours from starting the experiments otherwise there will be no current flow towards the cells because they begin to melt, also air bubbles are created inside the tubes when the agarose gel heats up. We have tried to overcome these limitations but unfortunately we could not keep the track of the same cells before and after changing the agar bridges because the chamber needs to be moved from the focus of the microscope. Another issue would be applying higher voltages but that would increase the temperature of the medium, due to Joule heating effect  $T \propto VI$ , and shorten the possible duration of the experiments.

#### 4 Determination of model parameters from *In vitro* studies

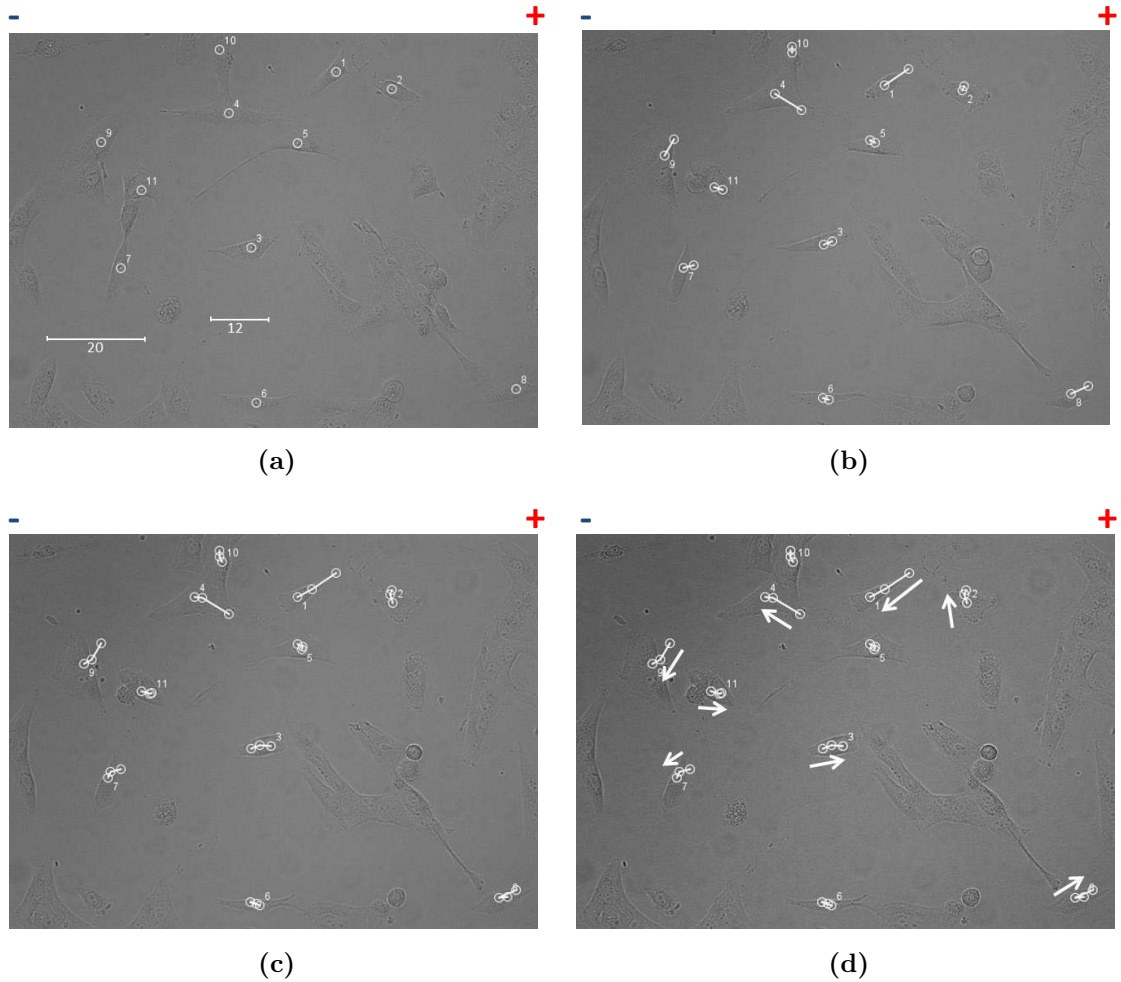


**Figure 4.10:** Visualization of osteoblast-like cell line MG-63 under time lapse microscopy (bars 20  $\mu\text{m}$ ). The cells are subjected to 141.8 V/m for 240 min. The number of tracked cells is 11. (a) cells in the initial or resting state, (b) after 120 min, (c) after 240, (d) after 240 min with the indication of the direction of migration. The signs + and - represent the anode and the cathode, respectively. Figures are produced together with Josefin Ziebert at the laboratory of Prof. Köhling Oscar Langendorff Institute of Physiology.

***In vitro* experiments with primary human osteoblasts** Osteoblasts cell line are often used in cell experiments because they are available from different suppliers and show stable results while repeating experiments several times [173]. Although MG-63 cells are used as a model for normal human osteoblasts they do not completely mimic each other. It is reported in [174] that primary human osteoblasts are more influenced by the Mg-based extracts compared to osteoblast-like cell line (MG-63, U2OS, and SaoS2). This assumes that primary osteoblasts are more sensitive to Mg-based implants.

To this extent, we have conducted further experiments stimulating primary human osteoblasts instead of osteoblast-like cell line MG-63. In the following experiments we would like to investigate whether the electric field could influence primary human osteoblasts.

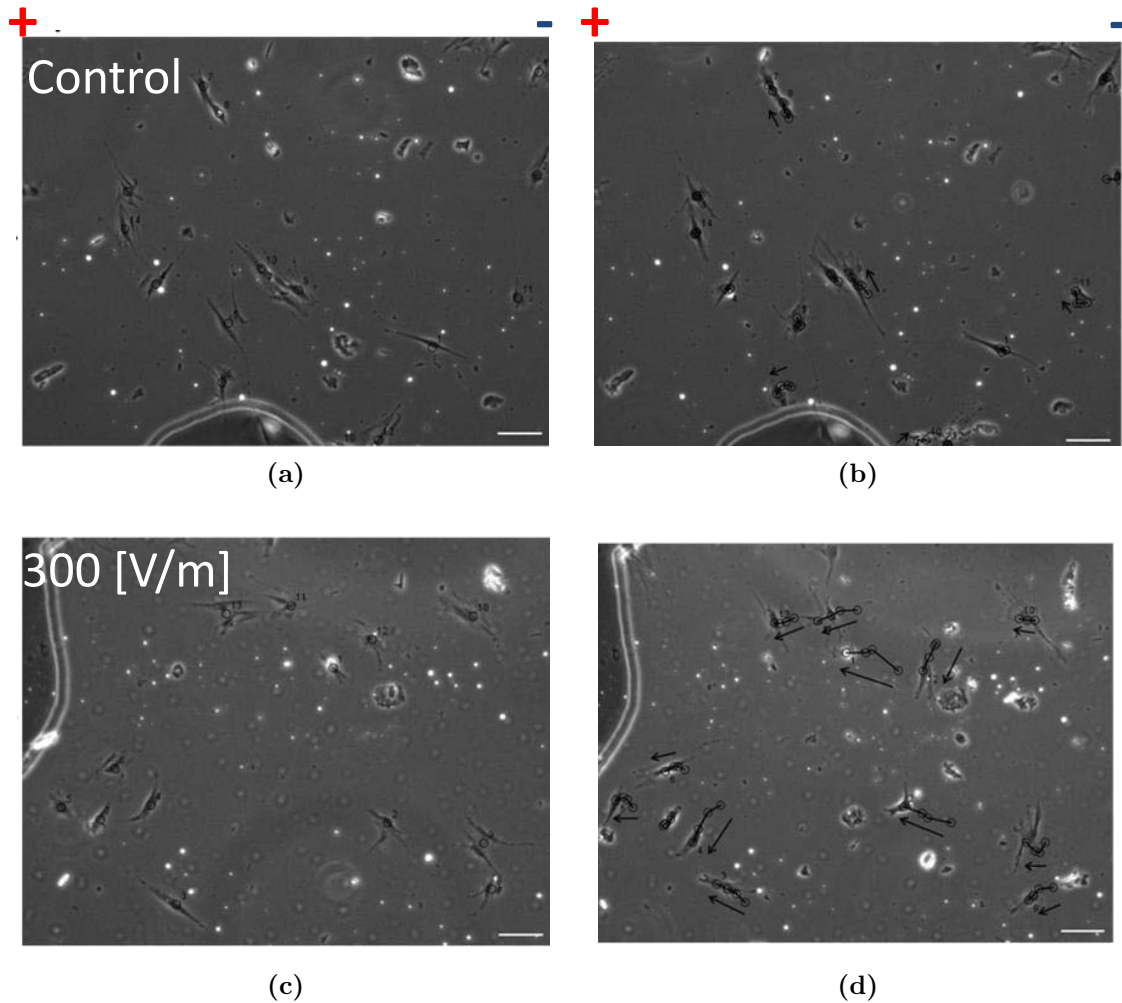
Primary human osteoblasts have been isolated from femoral hips of patients, who have received a total hip implant, after obtaining patient's agreement and approval of the Local Ethical Committee (A 2010-10), further information could be found in [175]). Primary cells are larger in comparison to MG-63 cells [176]. We have kept the same environments and setup of the previous experiment. An electric field strength of 300 V/m is used to stimulate the cells. The duration of the experiment is six and a half hours. The number of tracked cells is 13 and for the control sample is 15.

Figure 4.11 shows the experimental results. After six and a half hours of ES, the primary human osteoblasts show directional movement. The cells migrate toward the anode. This direction of migration corresponds to the direction of the stimulating electric field. The cells migrated with an average speed of 6.4  $\mu\text{m}/\text{h}$ .

In contrast, primary human osteoblasts in the absence of ES show a random behavior. Cells marked with 1, 2, 3, 4, 5, 7, 12, 13, 14 and 15 slightly have moved. Cells marked with 6, 8, 9, 11 have moved toward the anode. The cell marked with 10 has migrated toward the cathode.



#### 4 Determination of model parameters from *In vitro* studies



**Figure 4.11:** Visualization of primary human osteoblasts under time lapse microscopy (bars  $100 \mu\text{m}$ ). (a) is the control sample at the initial state, (b) is the control sample after 6.5 hours. The number of tracked cells is 15, (c) is the sample subjected to  $300 \text{ V/m}$  at the initial state, (d) is the sample subjected to  $300 \text{ V/m}$  after 6.5 hours. The number of tracked cells is 13. The signs + and - represent the anode and the cathode, respectively. Figures are produced together with Josefin Ziebert at the laboratory of Prof. Köhling Oscar Langendorff Institute of Physiology.

## 4.2 Numerical simulation of electrical components

The electric field strength and its distribution are important factors in electro-taxis experiments. Previous work [177] shows cell migration dependencies on amplitude and direction of the electric field strength. In this section, the methods and approaches used to study numerically the electrical components inside the electro-taxis chamber are provided.

### 4.2.1 Customized electro-taxis chamber

The three dimensional electro-taxis chamber is first designed in AutoCAD 2014, see subsection 4.1.2, and then imported as STL file to COMSOL MULTIPHYSICS® version 5.1. Silver material, which is a very good electric conductor, is assigned to

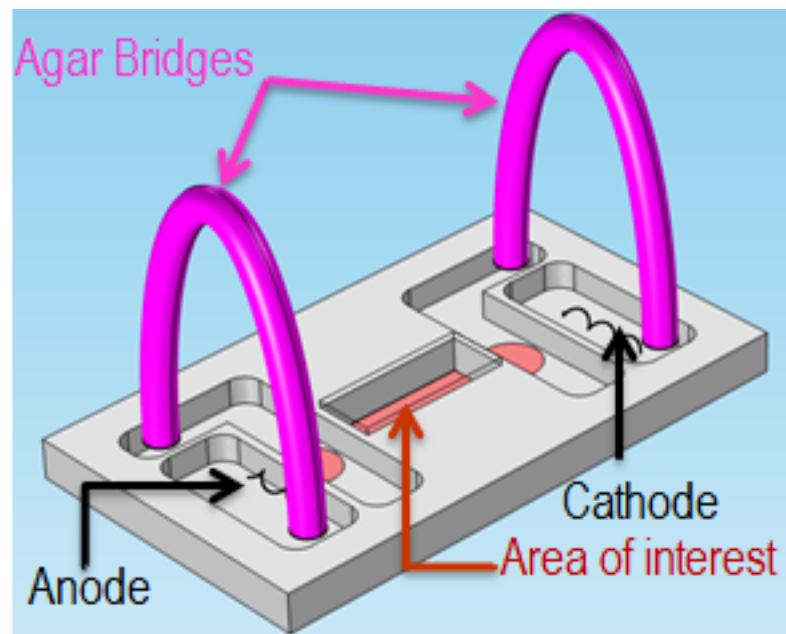


**Figure 4.12:** Three dimensional electro-taxis chamber with electrodes imported to COMSOL MULTIPHYSICS® version 5.1. The chamber consists of agar bridges highlighted in pink, the body of the chamber, which is made out of PLA, highlighted in grey, silver electrodes (anode and cathode) and the area of interest where the cells are cultured.

both electrodes. New materials for the PLA chamber and the culture medium are defined. A high conductivity of  $55 \cdot 10^6$  S/m is assigned to the pure silver material [178]. A relatively low conductivity of 1.6 S/m is assigned to our culture medium, which is based on the study presented in [179]. In [179], the electrical conductivity of five *in vitro* cultured media at different temperature are measured using a four terminal conductivity-measurement method. The media are: 0.9 % saline, standard



#### 4 Determination of model parameters from *In vitro* studies

culture Minimum Essential Medium containing Hanks salts and 25 *mM* HEPES buffer (MEM); MEM with 1 % horse serum; MEM with 10 % horse serum; and horse serum alone. MEM with 1 and 10 % horse serum also contains 0.6 % additional glucose, 2 *mM* glutamine, and 1 % penicillin/streptomycin. In their measurements they have obtained conductivity values  $\sigma_m$  ranging from 1.21 S/m to 2.00 S/m. An electric conductivity of 1.7 S/m is assigned to the agar-bridges. This value is based on the measurements made in [180], where they have measured the electrical conductivity of six different agar-bridges: two percentage by weight (2wt %) Agarose, 2wt % Agarose containing 0.1 mol of KCl, MKNO<sub>3</sub>, KI, MC<sub>s</sub>Cl and CaCl<sub>2</sub>. The obtained electrical conductivity is ranging from 1.135 S/m to 20.46 S/m. The PLA material is considered as an insulator and therefore it has very low conductivity of about 10<sup>-40</sup> S/m. The following table summarizes the electric conductivities of the components of the electro-taxis chamber.

	PLA	Silver electrodes	Culture medium	Agar-bridges
Electric conductivity [S/m]	10 <sup>-40</sup>	55 · 10 <sup>6</sup>	1.6	1.7

**Table 4.3:** Electric conductivities of the components of the electro-taxis chamber, i.e. PLA, silver electrodes, culture medium and agar-bridges.

We impose insulating boundary conditions at the boundaries surrounding the conducting materials. Thus, the boundary conditions are given as follows:

$$\mathbf{n} \cdot \mathbf{J} = 0, \quad (4.8)$$

where  $\mathbf{n}$  is a unit vector normal to the surface of the insulator and  $\mathbf{J}$  is the current density. The normal component of  $\mathbf{J}$  is vanishing and only the tangential component is nonzero.

A potential of 25 V is assigned to the anode. The cathode is connected to ground. The stationary solver defined in the electric currents interface is used to run the simulations or compute the solution. The model is solved on a 64-bit Windows computer (3.4 GHz Intel Xeon, 2 processors, 256 GB RAM). For the solution of the resulting linear system, we use the GMRES iterative scheme with incomplete LU factorization as preconditioner, see [181] for more informations. By default, quadratic Lagrange shape functions are used for second order PDE within COMSOL MULTIPHYSICS<sup>®</sup> version 5.1.

#### 4.2.2 Convergence study

A convergence study is performed in order to reach good accuracy for moderate computational effort. A tetrahedral mesh is used for the finite element modeling. The relative error RE of the estimated concentration of osteoblasts inside the circular

#### 4 Determination of model parameters from *In vitro* studies

opening near the cathode results in 0.4 % for a mesh with  $0.22 \cdot 10^6$  degrees of freedom (which is the number of nodes multiplied by the number of dependent variables). The relative error RE is calculated as follows  $RE = (\text{concentration of cells inside the circular opening of the finest mesh} - \text{concentration of cells inside the circular opening of the current mesh}) / \text{concentration of cells inside the circular opening of the finest mesh}$ . The finest mesh that is used for the convergence study has  $2.14 \cdot 10^6$  degrees of freedom. The mesh is refined at the short edges and smaller faces by choosing a small value of the minimum element size, in our case the minimum element size is set to 0.35 mm. This value of the minimum element size must be smaller than the smallest edge or face of the model to avoid warnings when generating the mesh. The following table summarizes the convergence study

Number of degrees of freedom	$0.05 \cdot 10^6$	$0.22 \cdot 10^6$	$0.74 \cdot 10^6$	$1.03 \cdot 10^6$	$2.14 \cdot 10^6$
Concentration of osteoblasts inside the circular opening [cells/ml]	$2.1657 \cdot 10^5$	$2.1625 \cdot 10^5$	$2.1586 \cdot 10^5$	$2.1560 \cdot 10^5$	$2.1539 \cdot 10^5$
Relative error RE [%]	0.54	0.40	0.22	0.10	0.00

**Table 4.4:** Convergence study.

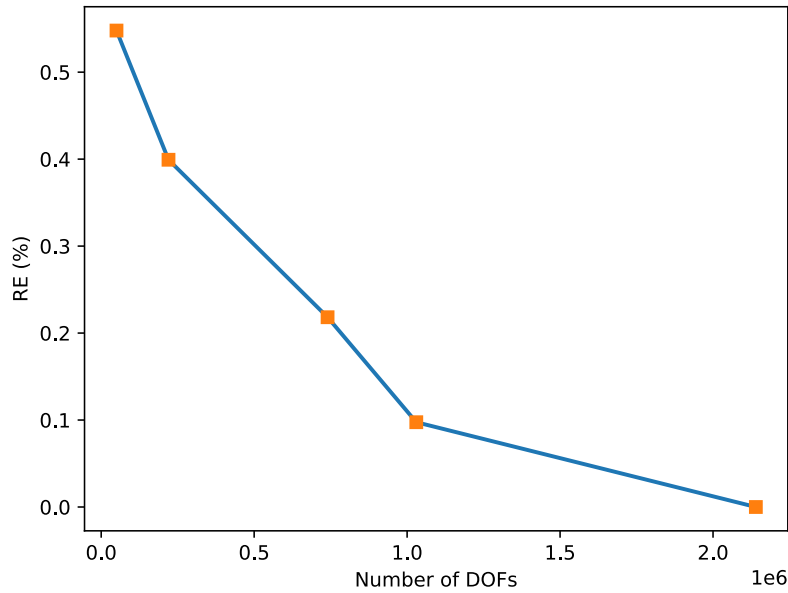


**Figure 4.13:** This graph shows the relative error RE of the estimated concentration of osteoblasts inside the circular opening as function of the degrees of freedom.

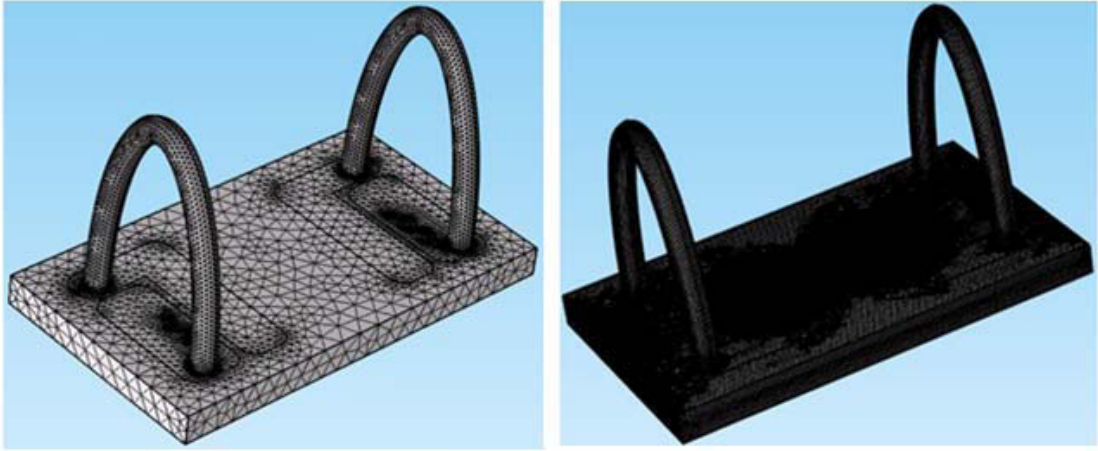


**Figure 4.14:** Discretization of the CAD model. Left: mesh chosen for the simulations; right: finest mesh that is used for our convergence study.

### 4.2.3 Visualization of the stimulating electric field

After running the simulation, we are now able to observe the distribution of the electric field strength and the current density. The current flows from the anode to the cathode. In between it passes first through the agar-bridges to the inner reservoirs, then to the medium where the cells are cultured and then back to the cathode through the inner reservoir and the agar-bridges as it is presented in the figure below.

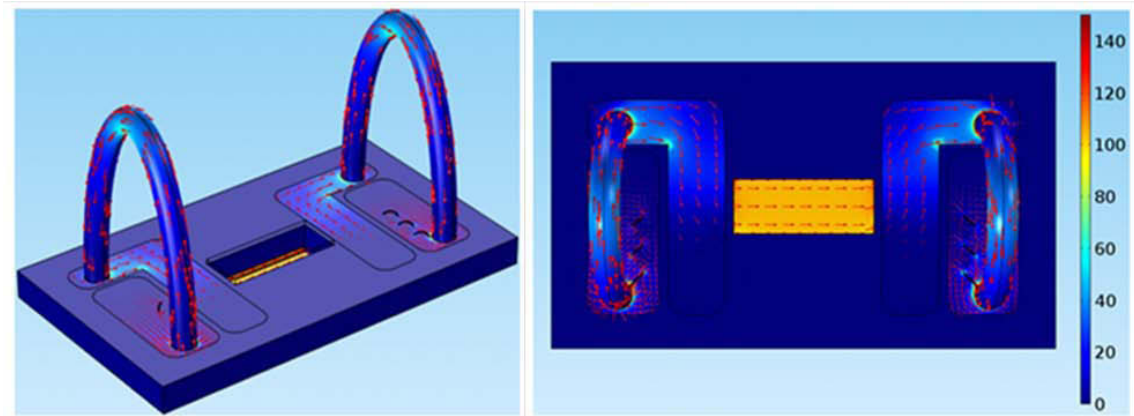


**Figure 4.15:** Distribution of the electric field amplitude  $\mathbf{E}$  in V/m (coloured scale) and the current density  $\mathbf{J}$  in A/m<sup>2</sup> (red arrows) inside the electro-taxis chamber. The applied voltage between the electrodes is 25 V.

The electric field is homogeneous and constant inside the area where the cells are cultured, which means, the applied Lorentz force on each single cell are identical in strength and direction. However, the value of the amplitudes of the electric field

#### 4 Determination of model parameters from *In vitro* studies

strength  $\mathbf{E}$  varies in the measurements and thus are different from the ones obtained from the simulations. Table 4.5 illustrates this difference. Higher magnitudes of the electric field strength are observed in the simulation than in the experimental results. The reason behind this difference is that the simulation model has not considered the resistance originating from electrochemical reactions at the interface between electrode and culture medium. These reactions result in a resistive thin layer of silver chloride. In section 4.3, the model is augmented accordingly.

$V_{meas}$ [V]	50	100	150	200	250
$\mathbf{E}_{meas}$ [V/m]	120	240	360	560	760
$\mathbf{E}_{sim}$ [V/m]	202.5	405.2	607.7	810.2	1012.8
$\Delta \mathbf{E}$ [V/m]	82.5	165.2	247.7	250.2	252.8
$\varepsilon_{\mathbf{E}}$ [%]	68.8	68.8	68.8	44.7	33.3

**Table 4.5:** The obtained magnitude of the electric field strength from both, the simulation and experimental measurements.  $V_{meas}$ ,  $\mathbf{E}_{meas}$ ,  $\mathbf{E}_{sim}$ ,  $\Delta \mathbf{E}$  and  $\varepsilon_{\mathbf{E}}$  are the applied voltage at the electrodes, the measured electric field, simulated electric field, absolute error and relative error, respectively. We use the measured field amplitude as the real value in order to calculate the relative error  $\varepsilon_{\mathbf{E}} = (\mathbf{E}_{meas} - \mathbf{E}_{sim}) / \mathbf{E}_{meas}$ . We observe that the relative error takes values between 68.8 % and 33.3 %, which are quite high. This indicates that the implementation of some factors that affect the behavior of our system are still missing. In section 4.3, these factors are addressed.

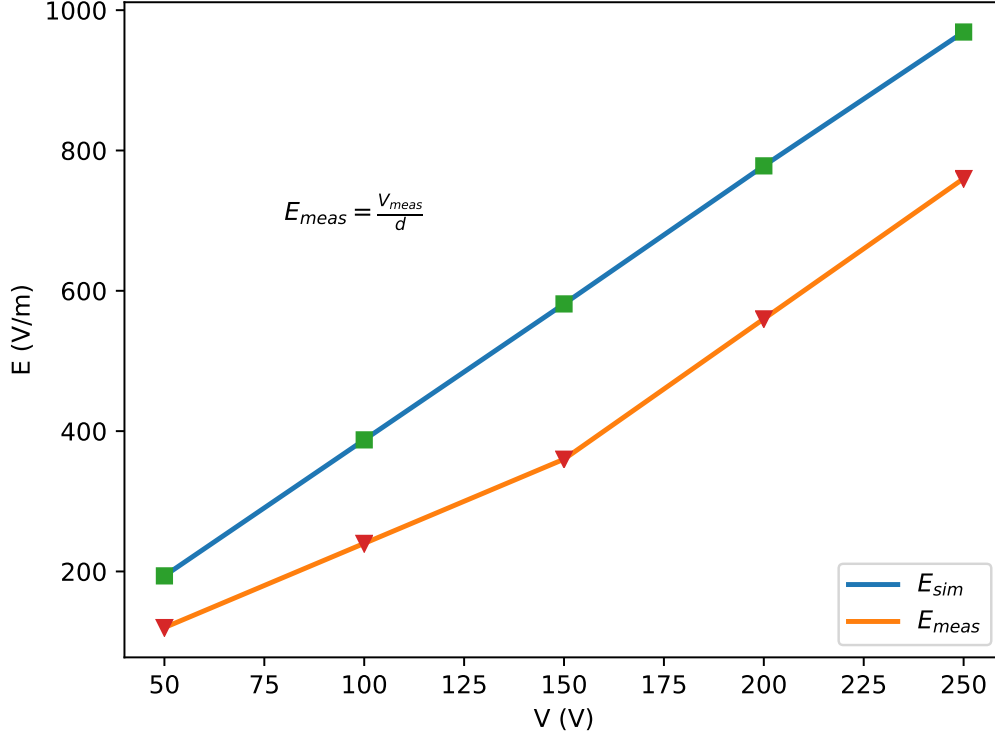


**Figure 4.16:** This graph shows the comparison between the simulated magnitude of electric field strength  $\mathbf{E}_{sim}$  and the measured ones  $\mathbf{E}_{meas}$  inside the culture medium. The  $x$ -axis represents the applied voltage between the electrodes  $V$  V/m and the  $y$ -axis represents the magnitude of the electric field strength  $\mathbf{E}$  V/m inside the area of interest. The formula presented in the figure shows how we calculate the measured magnitude of electric field strength from the measured voltage between the circular openings.

#### 4.2.4 Impedance and thickness of silver chloride layer

Many studies have focused on the characterization of the impedance and thickness of the silver chloride (AgCl) layer that builds up at the interface between the electrodes and the electrolyte [182], [183] and [184], which results from electrochemical reactions happening at the silver/electrolyte interface. During the electro-taxis experiments on bone cells, the AgCl layer behaves as a resistive layer which leads to a drop of the electric field and current in the vicinity of the electrode and thus to a lower electric current flowing through the electro-taxis system. Accordingly, we have observed a difference between the measured electric field amplitudes  $\mathbf{E}_{meas}$  and the simulated ones  $\mathbf{E}_{sim}$ , depending on the applied voltage. The relative error reaches up to  $\varepsilon_{\mathbf{E}} = 68\%$ . The reason of this difference is the voltage drop, which is resulting from the resistive layer of the silver chloride being created at the surface silver/electrolyte

#### 4 Determination of model parameters from *In vitro* studies

as mentioned previously. The aim of this section is to take into consideration the effect of the resistive layer (AgCl) on the amplitude of the electric field strength inside the culture medium. The thickness of the AgCl layer is taken from the literature as described below. A parametric study is conducted (see section 4.4) to determine the resistivity of the AgCl layer. Then, for validation, the obtained results are compared to values reported in literature.

The thickness of the AgCl layer is dependent on the concentration of the medium, the applied electric current and the duration of the electro-deposition of the AgCl on the silver electrode. The average thickness of the deposited AgCl layer observed in experiments is reported in [185] and [183] to be 20  $\mu\text{m}$  and in [186] a range from 4  $\mu\text{m}$  to 18  $\mu\text{m}$  is given. The layer was characterized using scanning electron microscopy. In our simulations, we have assigned 20  $\mu\text{m}$  of thickness to the AgCl layer and assumed it to be uniformly distributed.

Different values of the resistivity of the AgCl layer has been measured in various studies. In [187], the resistivity of the formed AgCl layer ranges from 8.34  $\cdot 10^2 \Omega\text{m}$  to 5  $\cdot 10^3 \Omega\text{m}$  depending on the concentration of potassium chloride (KCl) inside the medium and on the electric current density, which is used in anodizing AgCl. In [182], the resistivity ranges from 1.42  $\cdot 10^3 \Omega\text{m}$  to 3.34  $\cdot 10^3 \Omega\text{m}$ , which is dependent on the solution and the thickness of the AgCl layer. In the study [188], they have reported a resistivity range between  $10^3 \Omega\text{m}$  and  $10^5 \Omega\text{m}$  and observed that the resistivity of AgCl decreases with the increase of temperature and frequency. During the growth of the AgCl layer on the silver electrode, the resistivity of the AgCl layer has been calculated depending on the concentration of sodium chloride (NaCl) inside the solution and the electric current density [183]. The range reported lies between  $10^3 \Omega\text{m}$  and  $10^4 \Omega\text{m}$ . Thus, in these studies, different ranges of the AgCl layer resistivity have been reported taking in consideration different parameters and environmental conditions. It is important to conduct such a research on the resistivity of the AgCl layer in order to compare it to our results of the simulated resistivity of the AgCl.

### 4.3 Equivalent circuit for AgCl layer

Generally, when a metal is in direct contact with a salt solution, an electric double layer (EDL) is created at the interface metal/electrolyte due to the electrochemical reactions [189]. The EDL refers to two layers with opposite charges, either negative or positive. The first layer consists of electrons located at the outer surface of the metal or the conductor. The second layer consists of adsorbed ions and a region of diffused ions, which occurs due to electrostatic forces [190].

The EDL behavior is highly dependent on the type of metal. There exist two main categories of metal: ideally polarized (ideally nonreversible) and ideally non-polarized (ideally reversible) [191]. In the first category, when a voltage is applied

#### 4 Determination of model parameters from *In vitro* studies

between the electrodes no charges pass through the electrode/medium interface. However, they will be accumulated in the EDL and there is a proportional relationship with the applied voltage. Besides, there will be no electric current flowing between the two sides of the EDL except for the displacement current. The second category is in contrast with the first one, the current flows freely through the interface electrode/medium. Silver/silver chloride and platinum electrodes are considered ideally nonpolarized and ideally polarized, respectively [192] and [193]. This aspect of polarizability have been first introduced by F.O. König in 1934 [194]

Generally, the interfacial zone is represented by an EDL capacitor ( $C_{dl}$ ), an interfacial resistance called faradaic resistance ( $R_f$ ) and a medium resistance  $R_m$ . The equivalent circuit provides a clear understanding of the concept of the EDL. The equivalent circuit for the first category is shown in figure 4.17 where only the EDL capacitor  $C_{dl}$  is considered. For the second category,  $C_{dl}$  acts like an open circuit and therefore only the faradaic resistance  $R_f$  is counted [4].

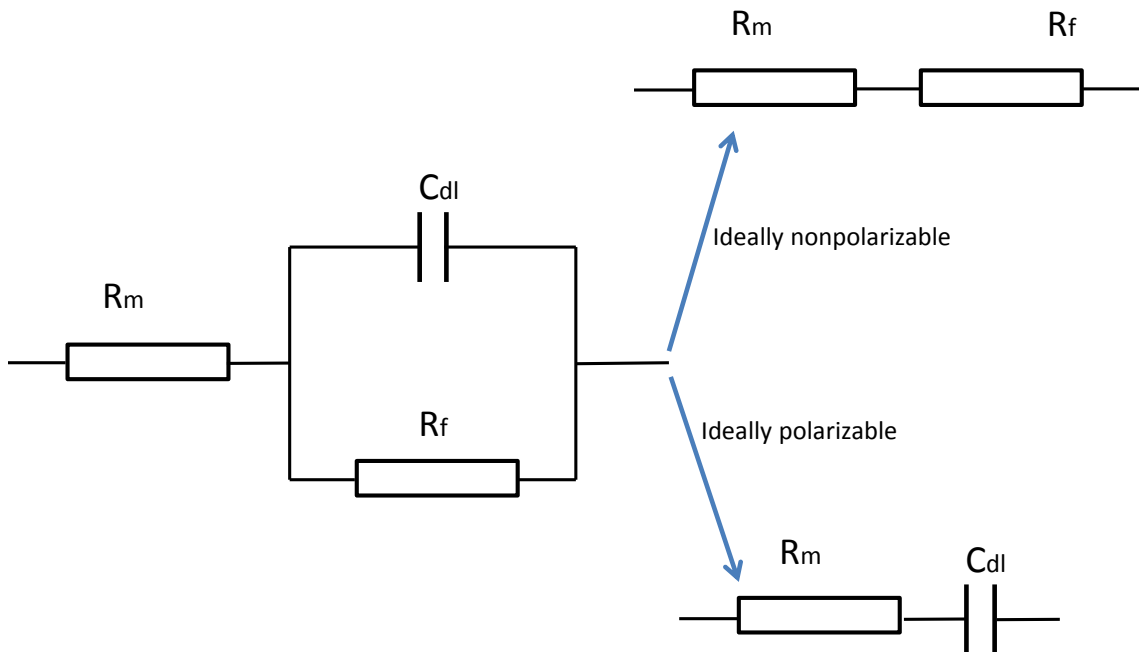


**Figure 4.17:** Equivalent circuit of the electric double layer in case of ideally polarizable and nonpolarizable electrodes adapted from [4]. In general the equivalent circuit for the EDL is composed of  $R_f$  and  $C_{dl}$ . In case of an ideally polarizable or nonpolarizable electrode it is approximated to  $C_{dl}$  and  $R_f$ , respectively.

## 4.4 Parametric study

We have included the faradaic resistance in our model. The faradaic resistance is assigned to both silver electrode surfaces with a layer thickness of  $20 \mu\text{m}$ . For simplicity this resistivity is assumed to be isotropic and to have no dependency on the applied voltage. We have conducted a parametric study in order to optimize the model prediction of the amplitude of the electric field strength  $\mathbf{E}_{sim}$ . First, we have assigned random values of resistivity to the AgCl layer, then we have run the simulations for applied voltages of 50, 100, 150, 200 and 250 V. Based on the comparison of the obtained electric field from the simulations and the measurements, we have determined a range for the resistivity of the AgCl layer where the parametric study has been conducted  $R_f \in [10^3, 2.8 \cdot 10^3]$ . Ten values of resistivity are studied from this interval:  $10^3, 1.3 \cdot 10^3, 1.5 \cdot 10^3, 1.8 \cdot 10^3, 2 \cdot 10^3, 2.1 \cdot 10^3, 2.2 \cdot 10^3, 2.3 \cdot 10^3, 2.5 \cdot 10^3$  and  $2.8 \cdot 10^3$  all values are in  $\Omega\text{m}$ , further details are given in table 4.6.

Based on figure 4.19, we can observe the adaptation of the electric field calculations to obtain values close to the measured values. We have assumed a linear dependency between the applied voltages and the resulting electric field. In other words, the resistivity of the AgCl is assumed to be constant. However, we can see that the  $\mathbf{E}_{meas}$  has two different values of slope, the first one belongs to the region where  $V$  takes values below 150 V and the second one belongs to the region where  $V$  is greater than 150 V. The average relative error is calculated for each value of resistivity (see figure 4.19 (a)) using the following equation

$$\varepsilon = \frac{\sum_{i=1}^n \varepsilon_i}{n} \quad (4.9)$$

where  $\varepsilon$  is the average relative error,  $\varepsilon_i$  is the relative error corresponding to each applied voltage  $i$ ,  $n = 5$  is the number of the applied voltages. The smallest  $\varepsilon$  is equal to 0.0717 (see figure 4.19 (a)), which is highlighted by a red point. This average relative error corresponds to the AgCl resistivity of  $R_{f6} = 2.1 \cdot 10^3 \Omega\text{m}$ .



#### 4 Determination of model parameters from *In vitro* studies

$R_f$ [ $\Omega\text{m}$ ]	$\mathbf{E}_{sim}$ [V/m]				
	50 [V]	100 [V]	150 [V]	200 [V]	250 [V]
1.0 $10^3$	152.6	305.2	457.9	610.5	763.1
1.3 $10^3$	142.3	284.5	426.8	569.1	711.4
1.5 $10^3$	136.1	272.2	408.3	544.5	680.6
1.8 $10^3$	127.8	255.6	383.5	511.3	639.1
2.0 $10^3$	122.8	245.6	368.5	491.3	614.2
2.1 $10^3$	120.5	240.9	361.4	481.9	602.4
2.2 $10^3$	118.2	236.4	354.7	472.8	591.1
2.3 $10^3$	116.1	232.1	348.1	464.1	580.2
2.5 $10^3$	111.9	223.8	335.7	447.7	559.6
2.8 $10^3$	106.3	212.5	318.7	425.0	531.2

**Table 4.6:** Parametric study. The simulated electric field amplitudes  $\mathbf{E}_{sim}$  are obtained for each combination of the applied voltage and the AgCl resistivity  $R_f$ , which takes values between  $1.0 \cdot 10^3$  and  $2.8 \cdot 10^3 \Omega\text{m}$ .

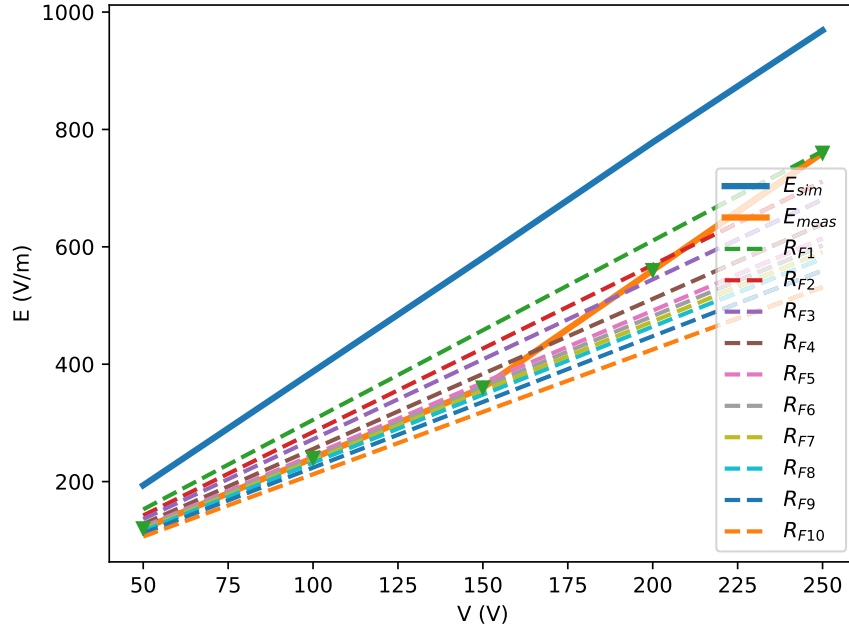


**Figure 4.18:** Results of the parametric study.  $\mathbf{E}_{sim}$  and  $\mathbf{E}_{meas}$  show a gap between the measured and simulated electric field values. The improvement in the estimated electric field values is achieved using different values of the resistivity  $R_f$  of the AgCl. Using the resistance of  $R_{f6}$  for the numerical simulations results in the best linear approximation of the measured values.

#### 4 Determination of model parameters from *In vitro* studies

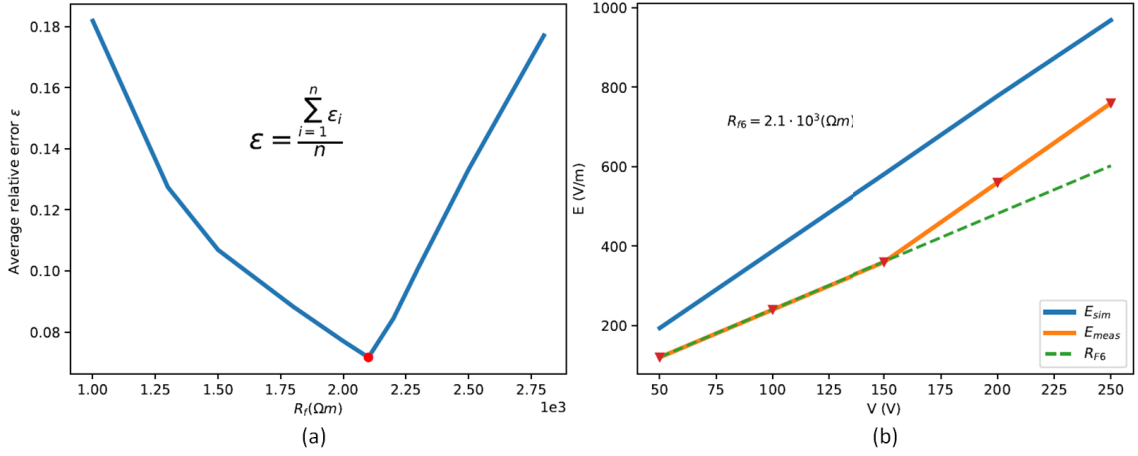


**Figure 4.19:** Results of the parametric analysis. Figure (a) shows the averaged relative error. The smallest relative error is highlighted by the red point. Figure (b) shows the improvement of the prediction of the simulated electric field value inside the culture medium.

After implementing the effect of the resistive layer in our simulation model, we have reduced the relative error from 68.8 % to 0.4 % in the first region where  $V$  takes values below 150 V. In the second region where  $V$  is greater than 150 V, the error is reduced from 39 % to 17 %. Besides, the obtained AgCl layer from the parametric analyses falls in the range reported in literature, see section 4.2.4. From table 4.7 we can conclude that our simulation model now provides a good representation of the electro-taxis chamber. It can be usefully applied to predict the electric field distribution given the value of the applied voltage and the geometrical and electrical properties of the electro-taxis chamber, medium and agar-bridges. However, for higher applied voltages the prediction of  $\mathbf{E}_{sim}$  is still not optimal because the resistive layer is assumed to be constant and independent on the applied voltage. In this case, a more complex model of the resistive layer of AgCl is needed to obtain better results.

$\mathbf{E}_{meas}$ [V/m]	120	240	360	560	760
$\mathbf{E}_{sim}$ [V/m]	202.5	405.2	607.7	810.2	1012.8
$\mathbf{E}_{new}$ [V/m]	120.5	240.9	361.4	481.9	602.4
$\epsilon \mathbf{E}_{old}$ [%]	68.8	68.8	68.8	44.7	33.3
$\epsilon \mathbf{E}_{new}$ [%]	0.42	0.38	0.39	13.95	20.74

**Table 4.7:** Improvements of the model. After conducting the parametric analysis, the prediction of  $\mathbf{E}_{sim}$  is improved.  $\mathbf{E}_{new}$  is the new computed electric field amplitude inside the culture medium after the improvement. The relative error is reduced to 0.4 % in the first region and to 17 % in the second region.

After the implementation of the AgCl layer and the improvements of the amplitude of the electric field strength inside the culture medium, we have simulated our

#### 4 Determination of model parameters from *In vitro* studies

experiments again ( $\mathbf{E}_{meas} = 300 \text{ V/m}$ ) aiming to adapt the simulation environment to the experimental one. The amplitude of the stimulation field is  $\mathbf{E}_{sim} = 300 \text{ V/m}$  inside the culture medium (see figure 4.20).

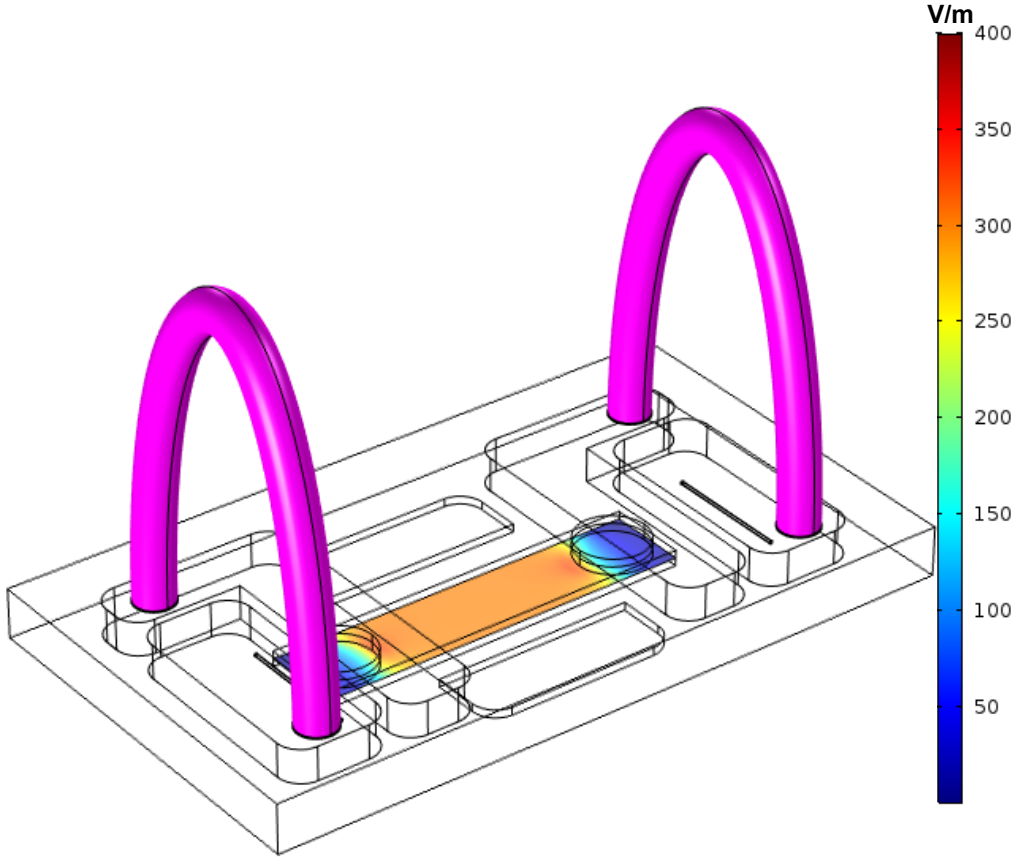


**Figure 4.20:** Simulation of the electric field inside the electro-taxis chamber after including a resistive layer at the electrode with resistivity value calibrated based on the experimental measurements, see figure 4.11.

### 4.5 Avoiding negative concentrations

Negative concentrations are a common problem in numerical simulations when solving reaction-diffusion systems [195]. These negative values are nonphysical in many applications like modeling heat transfer and transport of chemical species. Besides, they may lead to the growing of nonphysical oscillations of the numerical solution [196].

A solution to eliminate these negative values is to consider a positive limit value of the state variable  $C$ , if  $C$  is negative then  $C$  is assigned the value  $eps$ , where  $eps$

#### 4 Determination of model parameters from *In vitro* studies

is a small positive number. This solution is easy and straightforward but it is not applicable to our system as this is not conservative when considering this approach, which means that the following equation is not satisfied in all time steps:

$$M = \int_{CV} \rho dV \quad (4.10)$$

where  $\rho$  is the density and  $M$  is the total mass within the control volume  $CV$ .  $M$  must be constant in all time steps when the source and sink terms are zero and so-called "non-flux boundaries" are assumed within the control volume, in other words no influx or outflux takes place within the control volume [197].

We have also noticed from the simulation results a negative concentration during our experimental simulations with reaction-diffusion systems. We used an analytical approach in order to overcome this problem. In the analytical approach we have introduced a logarithmic transformation, which is often applied for such kind of problem see e.g. [198].

$$C = e^{C_t} \quad C_t = \ln(C), \quad (4.11)$$

where  $C_t$  is the new transformed variable. The cells concentration  $C$  is always positive as it is introduced in equation (4.11). From equation (4.11), the concentration  $C$  takes positive values because the exponential of the new variable  $C_t$  is always positive. The following equations are derived from equation (4.11):

$$\frac{\partial C}{\partial t} = e^{C_t} \frac{\partial C_t}{\partial t}, \quad (4.12)$$

$$C = e^{C_t} \quad C_t \quad (4.13)$$

Inserting equations (4.12) and (4.13) into equation (4.17) introduced further below we get the following:

$$\frac{\partial C_t}{\partial t} = \frac{1}{e^{C_t}} (e^{C_t} D \quad C_t \quad e^{C_t} kp\mathbf{E}) \quad (4.14)$$

after solving equation (4.14), the transformed variable  $C_t$  is inserted in equation (4.11) in order to obtain the original cells concentrations  $C$ .

Initial and no-flux boundary conditions are presented as following:

$$C_{t0} = \ln(C_0), \quad (4.15)$$

$$\mathbf{n} (e^{C_t} D \quad C_t \quad e^{C_t} kp\mathbf{E}) = 0 \quad (4.16)$$

## 4.6 Numerical simulation of bone cell population

In this section, the simulation of the reaction-diffusion model of human osteoblasts in the presence of the electrical stimulus is described and studied for the electro-taxis

#### 4 Determination of model parameters from *In vitro* studies

chamber. The temporal evolution of the population of human osteoblasts inside the culture medium is studied numerically (see figure 4.23). The model parameters, sensitivity function, directness parameter and initial concentration are estimated from the experiments (see figure 4.11). The resistive layer of AgCl forming at the silver electrodes interface is included in the model.

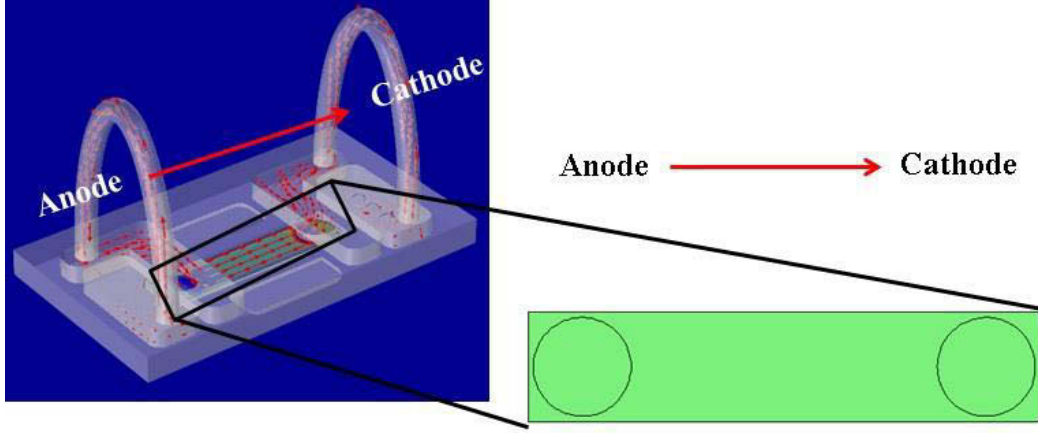


**Figure 4.21:** Electro-taxis chamber. Left: flow of electric current inside the area of interest where the cells are cultured, right: uniform concentration of human osteoblasts at the initial state.

#### 4.6.1 Model parameters

The reaction-diffusion equation (3.41) described in section 3.5 is rather general. Specifically, for our experimental simulation we have chosen the functions as follows: (i)  $g(ES) = k$ , which is the sensitivity constant. This function can be chosen as a saturation function if electro-taxis experiments are conducted for different electric field strengths where the saturation point  $E_{sat}$ , the point where speed of cells reaches its limit, for the speed of cells is determined. (ii) The external ES is chosen to be the electric potential  $\phi$ , "ES" =  $\phi$ . (iii) Since the experiments are made for a relatively short time, we may assume that there is no cell decay and proliferation, which means that the source function  $f(C, ES) = 0$ . Thus, we arrive at the following specific case:

$$\frac{\partial C}{\partial t} = (D \nabla^2 C - Kp\mathbf{E}), \quad (4.17)$$

these kinds of equations are often used to model chemotaxis, haptotaxis or phototaxis. In our case, we have used it to model electro-taxis. Further, similar to chemotaxis [199] :

$$Kp\mathbf{E} = \mathbf{u}, \quad (4.18)$$

#### 4 Determination of model parameters from *In vitro* studies

where  $\mathbf{u}$  is the speed of cells. From equation (4.18) we can calculate the sensitivity constant if we know the speed of migration from the experiments.

For primary human osteoblasts cells, the migration velocity obtained from our experiments is  $\mathbf{u} = 6.4 \mu\text{m/h}$  when they are stimulated with an electric field  $\mathbf{E} = 300 \text{ V/m}$ . Inserting these values into equation (4.18) we get  $k = 5.9278 \cdot 10^{-12} \text{ m}^2\text{s}^{-1}\text{V}^{-1}$ . At time zero, the concentration of human osteoblasts is equal to  $C_0 = 2 \cdot 10^3 \text{ cells/ml}$ ,  $p$  equals -1 because the cells move toward the anode,  $D$  is equal to  $2 \cdot 10^{-9} \text{ cm}^2\text{s}^{-1}$ , this value is chosen to be in the range of magnitude reported in [200]. The following table summarizes the parameters used:

Parameter	Human osteoblasts cells
Diffusion coefficient [ $\text{cm}^2\text{s}^{-1}$ ]	$D = 2 \cdot 10^{-9}$
Sensitivity constant [ $\text{m}^2\text{s}^{-1}\text{V}^{-1}$ ]	$k = 5.9278 \cdot 10^{-12}$
Parameter $p$	$p = -1$
Initial concentration [cells/ml]	$C_0 = 2 \cdot 10^3$

**Table 4.8:** Reaction-diffusion model parameters

We impose no-flux boundary conditions at the boundaries surrounding the area of interest. The no-flux boundary conditions are presented as following:

$$\mathbf{n} \cdot (D \nabla C - Ck p \mathbf{E}) = 0, \quad (4.19)$$

where  $\mathbf{n}$  is a unit vector normal to the no-flux boundary. Since the experiments are done in the so-called two-dimensional electro-taxis method, which means that the cells can only move in the  $x - y$  plane, we set the diffusion coefficient  $D$  and the electric field strength  $\mathbf{E}$  in  $z$ -direction to zero.

After applying the ES to human osteoblasts, a remarkable effect of the electric field on the cells migration can be observed (see figure 4.22). From the temporal evolution of the concentration of human osteoblasts we can draw conclusions about the movement of cells. The ES pushes the cells to move toward the direction of the anode. The concentration inside the circular opening at the initial state is  $2 \cdot 10^3 \text{ cells/ml}$  for both circular openings. At the left circular opening (near the anode), the evolution of the population of human osteoblasts  $C_A$  after 5, 24, 48, 72, 96, 120 and 240 h is as follows:  $2.0086 \cdot 10^3$ ,  $2.0405 \cdot 10^3$ ,  $2.0803 \cdot 10^3$ ,  $2.1200 \cdot 10^3$ ,  $2.1600 \cdot 10^3$ ,  $2.2002 \cdot 10^3$  and  $2.4068 \cdot 10^3 \text{ cells/ml}$ . A corresponding decrease in cell concentration  $C_C$  happens at the right circular opening (near the cathode) with  $1.9914 \cdot 10^3$ ,  $1.9607 \cdot 10^3$ ,  $1.9247 \cdot 10^3$ ,  $1.8909 \cdot 10^3$ ,  $1.8590 \cdot 10^3$ ,  $1.8284 \cdot 10^3$  and  $1.6922 \cdot 10^3 \text{ cells/ml}$ , compare figure 4.23 . In the middle of the culture medium, we notice a uniform concentration. This does not mean that the cells are not migrating toward the anode, however the amount of the influx is equal to the outflux in this region.

4 Determination of model parameters from *In vitro* studies

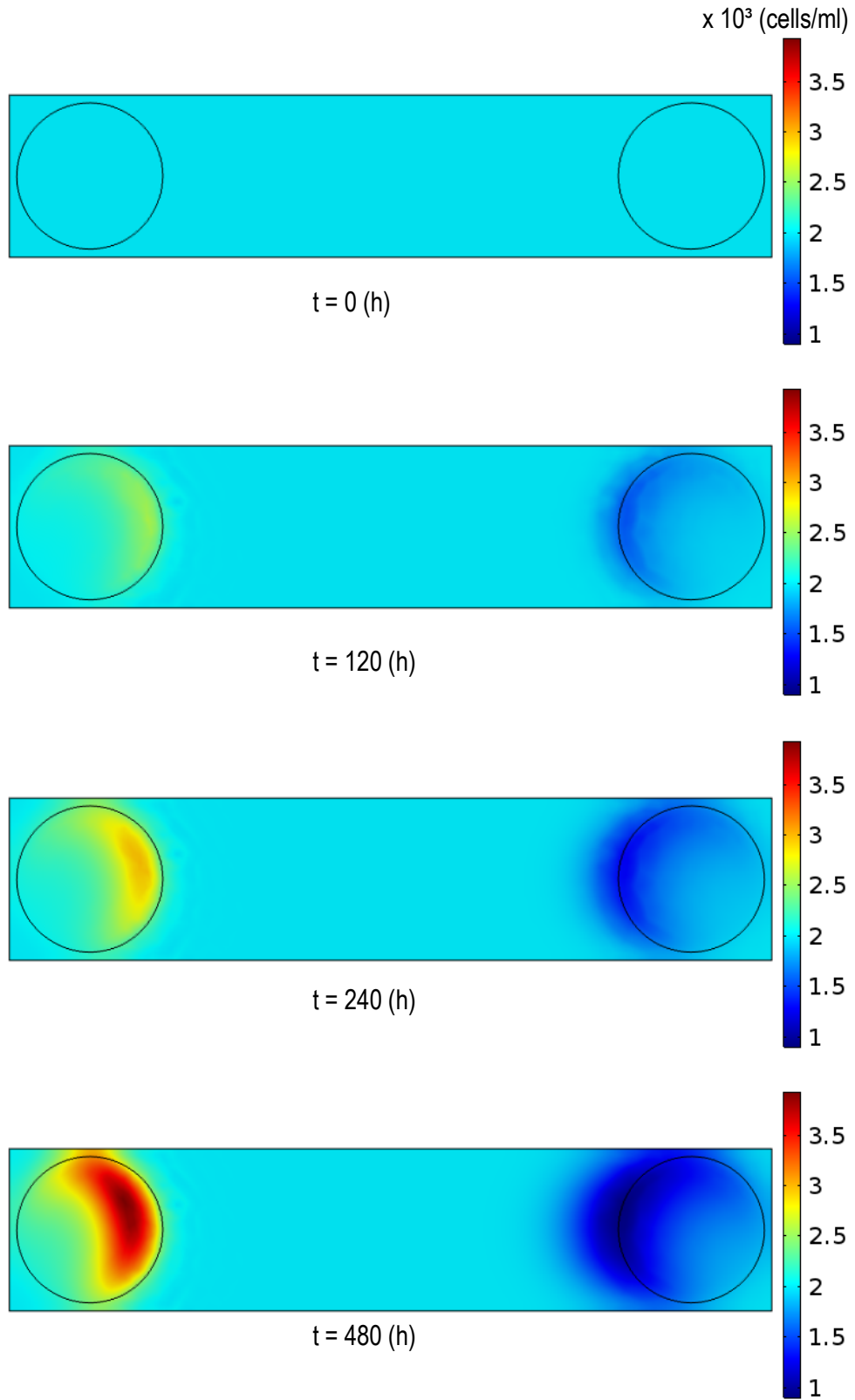


**Figure 4.22:** Temporal evolution of primary human osteoblasts inside the culture medium.

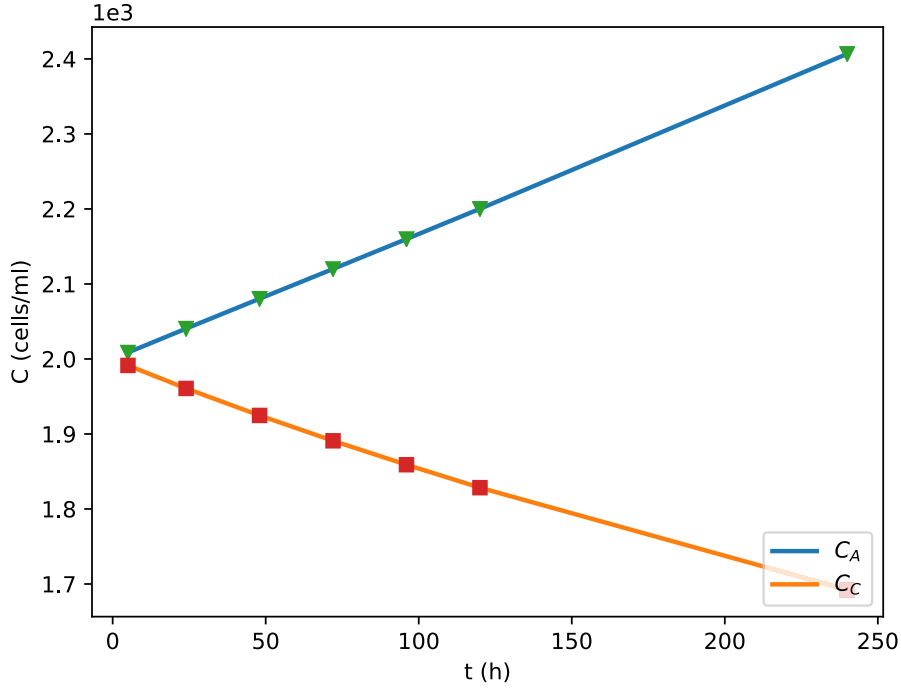


**Figure 4.23:** This graph resumes the temporal evolution of the population of primary human osteoblasts inside the circular opening near the anode ( $C_A$ ) and near the cathode ( $C_C$ ) as a function of time  $t$ .

#### 4.6.2 Comparison of both numerical models

We kept the same characteristics of the simulation environment for both methods, in the original form and logarithmic transformation introduced in subsection 4.5. We have quantified and compared the population of primary human osteoblasts cells for both methods (see figure 4.24). The table 4.9 resumes the temporal evolution of the population of human osteoblasts inside the circular opening near the anode ( $C_{tA}$ ) and near the cathode ( $C_{tc}$ ) for the logarithmic transformation.

From the simulation results we notice a small difference between the primary human osteoblasts concentration for both methods, the original method and the transformed one. This difference is due to the numerical error resulting from discretization of the exponential functions presented in equation (4.14). This relative error is equal to  $2.1174 \cdot 10^{-5}$  and thus negligible. In general one can say that the logarithmic transformation provides an alternative to the original form. However it is difficult to derive in case of more complex reaction-diffusion models. The following graphs illustrate the difference between results of the two methods.



#### 4 Determination of model parameters from *In vitro* studies

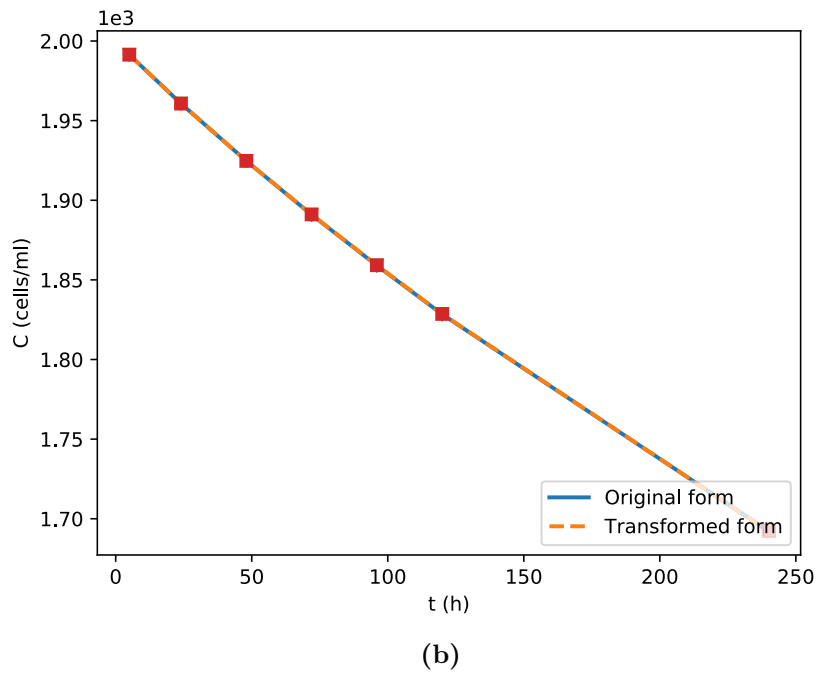
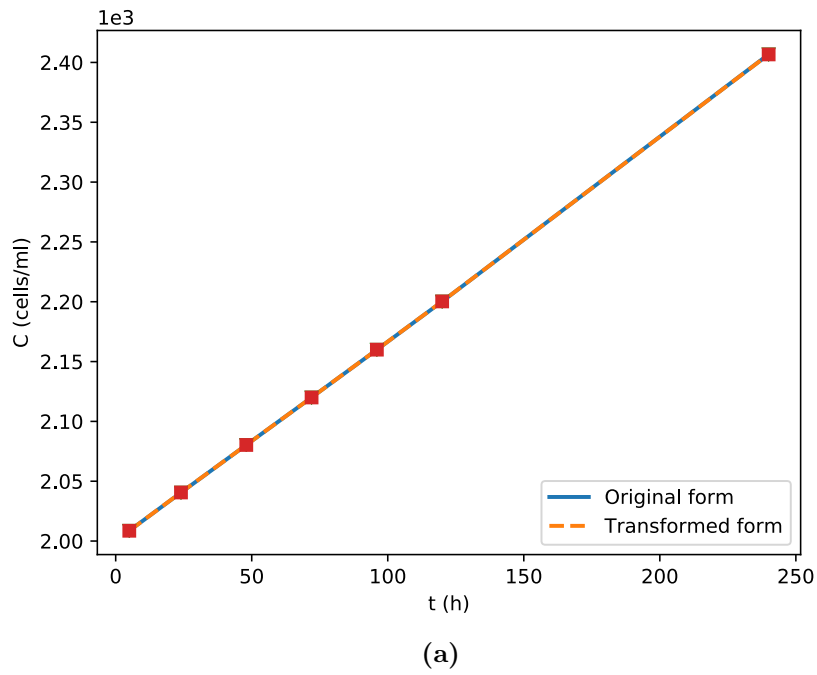


**Figure 4.24:** Comparison between the original method and the transformed one. Figures (a) and (b) show the temporal evolution of the population of primary human osteoblasts inside the circular opening near the anode and the cathode, respectively, for both methods.

#### 4 Determination of model parameters from *In vitro* studies

Time [h]	$C_{tA}$ [cells/ml]	$C_{tC}$ [cells/ml]
0	2.0000 $10^3$	2.0000 $10^3$
5	2.0086 $10^3$	1.9914 $10^3$
24	2.0406 $10^3$	1.9607 $10^3$
48	2.0803 $10^3$	1.9247 $10^3$
72	2.1200 $10^3$	1.8911 $10^3$
96	2.1600 $10^3$	1.8592 $10^3$
120	2.2003 $10^3$	1.8286 $10^3$
240	2.4067 $10^3$	1.6922 $10^3$

**Table 4.9:** Temporal evolution of the population of primary human osteoblasts in case of logarithmic transformation method.

## 5 Numerical study of *in vivo* electro-stimulating system

The aim of this chapter is to study the influence of an electro-stimulating dental implant on bone cells. Platelets migration and interaction within a realistic 3D model adapted from an electro-stimulating dental implant is studied. A DC voltage of 3.1 V is applied at the electrodes. The electric field distribution around the electro-stimulating dental implant is simulated. A high concentration of platelets around the implant surface is achieved after one day of healing. Based on these results, it is shown that osseointegration of dental implants in bone could be enhanced and accelerated by means of ES. Partial results of the presented work have been submitted at [202]

### 5.1 Mathematical framework

Here, the system of partial differential equations which couples the electric components of the external ES and the evolution of the platelet concentration is described. Firstly, the external ES is mathematically modeled (see section 3.4). Secondly, the mathematical model for platelets sensing and responding to external ES is adapted from the formulations presented in section 3.5 and it is modeled as follows:

$$\frac{\partial C}{\partial t} = (D_c \nabla^2 C + C g_c(ES) p_c \nabla \cdot \nabla (ES)) + f(C, ES) \quad (5.1)$$

where  $C = C(x, t)$  is the concentration of platelets at time  $t$  and spatial position  $x$ ,  $D_c$  is the platelet's diffusion coefficient,  $g_c(ES, \dots)$  is the sensitivity function of platelets to an external ES. The sensitivity function depends on the environmental cues, for example, cell types concentrations, medium viscosity and external stimulus. For simplicity, it is chosen to depend only on the external ES. The sensitivity function is similar to the chemotactic sensitivity function in the Patlak-Keller-Segel (PKS) model [135].  $p_c$  is a constant depending on the cell type. It takes the value 1 if the cell has the property to move against the gradient of the ES and -1 in the opposite case.  $f(C, ES)$  is the source term which depends on cell concentration and ES. Only apoptosis is considered for the platelets source term. Equations (5.1) and (3.41) are derived from the gradient-based model, which is used extensively in chemotaxis, haptotaxis or phototaxis. Platelets may detect and respond to the local gradient of the electric potential. The function  $g_c(ES)$  must be positive in order to ensure

that platelets move towards a high electric field, i.e. in our case to the negative pole (cathode). It is reported in literature [201] that platelets migrate towards a titanium dental implant, which is negatively charged [109]. In order to reduce the complexity of the system we choose:  $g_c(ES) = k_c$ , which is the sensitivity constant,  $f(C, ES) = -A_c C$ , where  $A_c$  is the decay rate,  $ES = \phi$ , where  $V$  is the electric potential. These simplifications are inserted in equation (5.1). The electric field strength equals the negative gradient of the potential according to equation (3.38). Therefore, equation (5.1) is simplified to

$$\frac{\partial C}{\partial t} = (D_c \nabla^2 C - C k_c \rho_c \mathbf{E}) - A_c C, \quad (5.2)$$

where  $\mathbf{E}$  is the electric field strength.

## 5.2 3D dental implant design

In this section, we have modeled a 3D dental implant which is adapted from the one that is described in literature [120]. The electro-stimulating dental implant is inserted into the mandible of a dog as shown in Fig. 5.2(a) [120]. The study described in this chapter is published in a conference paper [202]. As a first approach, we propose a 3D model composed of the electronic dental implant, made of titanium, and the surrounding tissue. Figure 5.1(a) shows the dimensions of the electro-stimulating implant. The upper part has a diameter of 5.5 mm and a height of 6.5 mm. The reference electrode has a diameter of 3 mm and a height of 9 mm. Figure 5.2(b) shows the tissue surrounding the implant, i.e. saliva, cortical bone, cancellous bone and blood. The voltage applied at the electrodes is 3.1 V. Zirconium dioxide (ZrO<sub>2</sub>) is chosen as insulator because of its biocompatibility; its electric conductivity is  $10^{-12}$  S/m and its relative permittivity is 29. The dielectric tissue properties is taken from Gabriel et al. [203]. Table 5.1 summarizes the dielectric properties of the surrounding tissues.

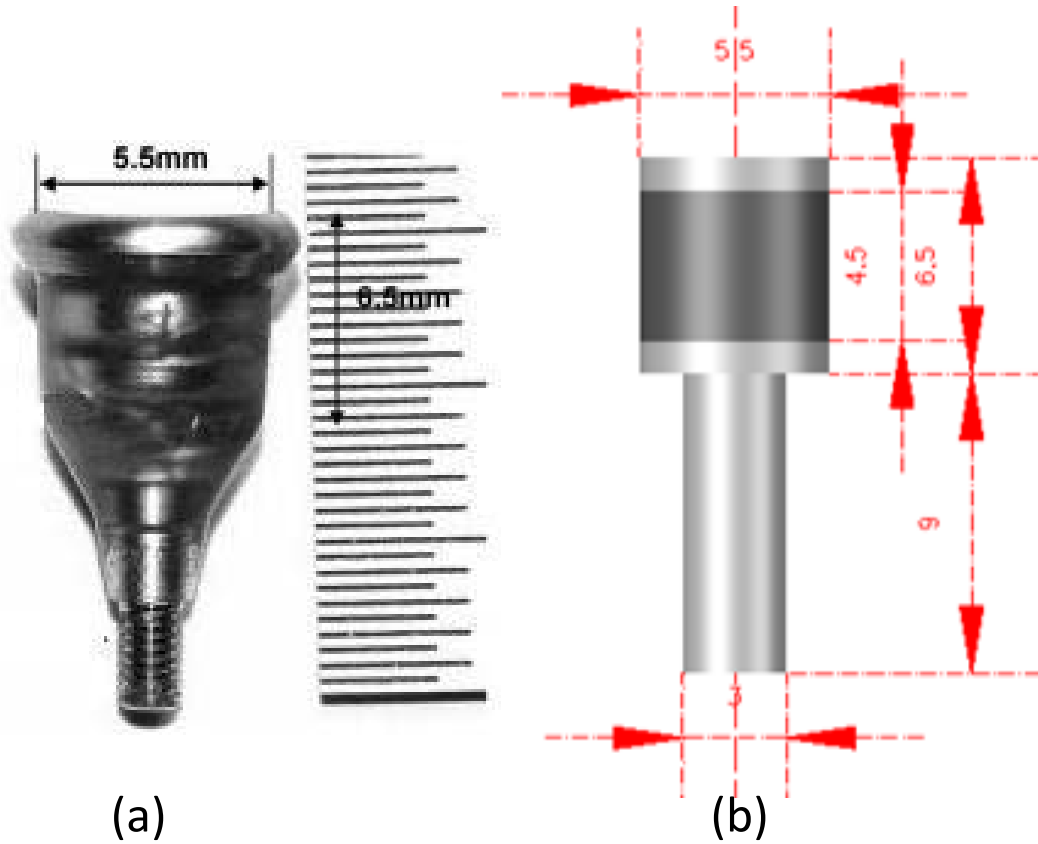


**Figure 5.1:** Electro-stimulating dental implant. (a) A real dental implant (courtesy of J. K. Song, used with permission from [120]). (b) Simplified three dimensional 3D model of the electro-stimulating dental implant designed in COMSOL MULTIPHYSICS® version 5.1 [202] .

Material	Conductivity $\sigma$ [S/m]	Relative permittivity $[\epsilon_r]$
Cortical bone	0.020045	25,119
Cancellous bone	0.078902	4,020,200
Saliva	1.5	99
Blood	0.7	2,560

**Table 5.1:** Dielectric properties of the surrounding tissues used in the simulation. The following tissues are considered: Cortical and cancellous bone, saliva and blood.

Equation 5.2 is solved inside the blood domain, i.e. in the cavity between the host bone and the dental implant surface. Zero flux of platelets is assumed at the implant surface and at the boundaries between the blood and both, the cortical and cancellous

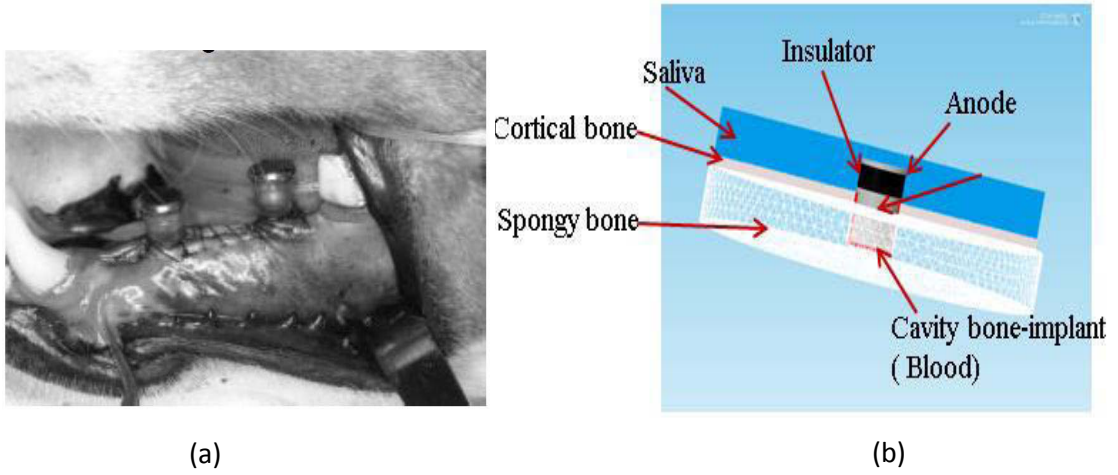


**Figure 5.2:** Electro-stimulating dental implant and the surrounding tissues. (a) and (b) are the 3D electro-stimulating dental implant in the *in vivo* experiment, with the surrounding tissue (courtesy of J. K. Song, used with permission from [120]) and in the abstract model [202], respectively .

bone. The average value of platelets in human blood [204] is  $3 \cdot 10^8$  cells/ml. This value is chosen as initial concentration. The diffusion coefficient of the platelets  $D_c$  is  $1.58 \cdot 10^{-9} \text{ cm}^2\text{s}^{-1}$  [205]. Assuming that after four days of endosseous healing, only a residual fraction of 50 % of the initial concentration of platelets remains [204], the platelet's decay rate  $A_c$  is estimated as  $0.18 \text{ day}^{-1}$ . Due to the lack of experiments on the platelet migration under the effect of DC voltage, the sensitivity constant  $k_c$  is determined by means of numerical simulations such that the platelet concentration around the implant falls in the range of simulation results reported in [2], where they have studied the effect of implant-surface roughness on endosseous healing; a rough implant-surface has a high negative charge density [109]. This procedure led to the value of  $7 \cdot 10^{12} \text{ m}^2\text{V}^{-1}\text{s}^{-1}$  for  $k_c$ . The model formulation is implemented in COMSOL Multiphysics<sup>®</sup>. A convergence study is performed in order to reach good accuracy for moderate computational effort. The relative error of the estimated platelet concentration around the dental implant results in  $5 \cdot 10^{-4}$  cells/ml. The chosen mesh for the simulation has  $538 \cdot 10^3$  degrees of freedom. The finest mesh used for the convergence study had  $18 \cdot 10^6$  degrees of freedom.

### 5.3 Electric field distribution

Figure 5.3 shows the electric field distribution obtained for an applied voltage of 3.1 V at the electrodes. Figure 5.3 (a) shows a cross section of the electric field

distribution around the electronic dental implant. The red arrows show the direction of the electric field, which is, of course, from the anode to the cathode. The high electric field strength at the sharp edges of the cathode and the anode is because of the so-called edge effect appearing at the sharp edges in this simplified model. In a practical implant one would avoid such sharp edges. Figure 5.3(b) shows a cross section-zoomed view of the electric field strength at the area of interest (cavity domain). The cavity domain extends 0.6 mm from the side of the reference electrode and has 1 mm distance from the bottom. There is a high magnitude of the electric field strength of 70 V/m near the reference electrode surface, at the region opposite to the cancellous bone, and it gradually decreases until it reaches 50 V/m at the boundary cavity-cancellous bone. A low magnitude of electric field strength of 14 V/m is found near the reference electrode surface, at the region opposite to the cortical bone. One assumes amplitudes (absolute values) of the electric field strengths between 5 V/m and 70 V/m between bone and implant as beneficial for bone formation and regeneration [206].

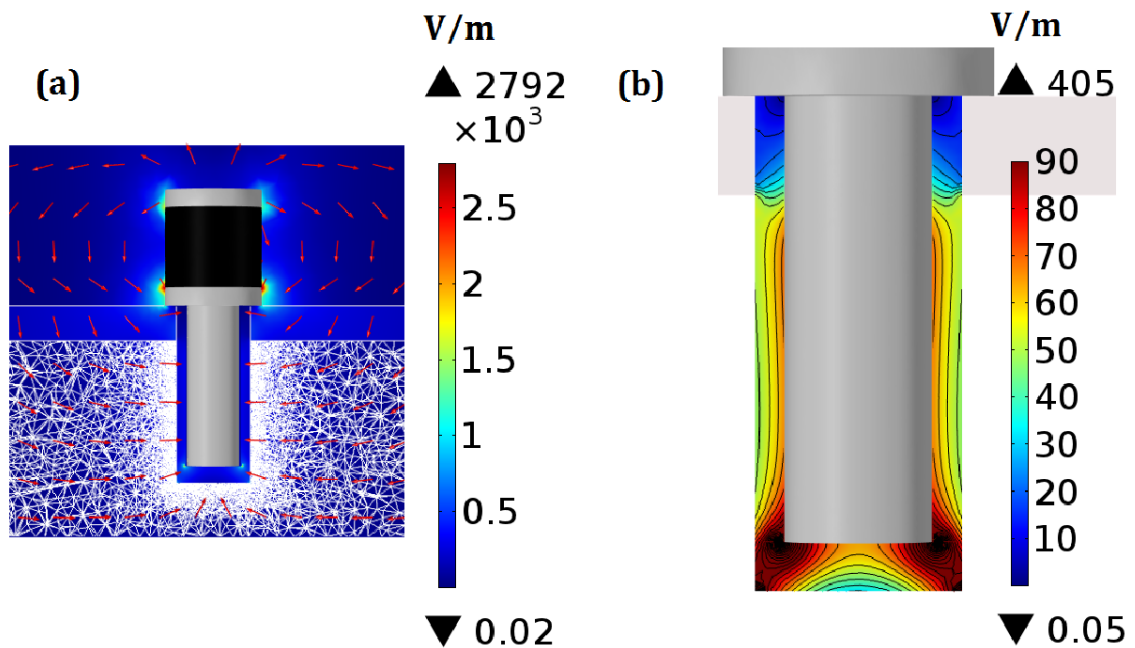


**Figure 5.3:** Electric field strength amplitude V/m distribution around the dental implant: (a) Cross section of the complete simulation model with highlighted mesh in the cancellous bone, arrow plot of the electric field strength distribution (red arrows), (b) cross section-zoomed view of absolute value of the electric field strength in the cavity in the bone around the electronic implant [202].

## 5.4 Evolution of platelets concentration

From the simulation results, we notice a difference of platelet concentrations between the control sample and the sample under the presence of the external ES at the early stages of the healing process. The initial concentration of platelets is uniform and equal to  $3 \cdot 10^8$  cells/ml for both samples, at time  $t = 0$ .

Figure 5.4(a, b) shows the concentration of platelets for the control sample (a) and for the sample under the effect of the external ES (b), each after one day of healing. A quite uniform concentration of platelets can be observed for sample (a) because of the random and slow movement of platelets caused by the diffusion coefficient  $D_c$ . However, a very high concentration of platelets is observed for sample (b) near the surface of the dental implant, especially at the edges. An average concentration of  $3.1507 \cdot 10^8$  cells/ml is calculated for a 0.01 mm thick layer around the implant. This value is relatively high in comparison to the value of  $8.693 \cdot 10^7$  cells/ml at the boundaries between cancellous bone and blood. A quite uniform distribution of platelets is observed around the region between the cortical bone and the dental implant. Figure 5.4(c, d) shows the concentration of platelets for the control sample (c) and the sample under the effect of the external ES (d), each after four days of healing. In Fig. 5.4(c) it can be observed that four days after the insertion of the implant the external ES leads to an increase in the number of platelets near the implant surface. The average concentration at the 0.01 mm thick layer is  $2.4664 \cdot 10^8$  cells/ml, which is high compared to the control sample, where the concentration of the platelets is almost uniform and equal to  $1.505 \cdot 10^8$  cells/ml. This migration of platelets towards the implant surface is expected, since the constant  $p_c = 1$ , which means platelets like to move towards higher electric field strength. In Fig. 5.4(c), besides the uniform distribution of platelets, 50 % of the platelets remains which is in accordance with the half-life rate reported in [204]. A small difference in half-life rate of platelets of 0.1 % has been determined, when the tissue is exposed to ES. In consequence, ES slightly decreased the rate of decay after four days of healing. To this extent, the electric field strength distribution may play an important role in apoptosis of platelets.

## 5.5 Discussion

The parameter estimation of the decay rate of platelets  $A_c$  is in accordance with the half-life time reported in [204]. Platelets sensitivity to the electric potential gradient is presented by the parameter  $k_c$ . First results are obtained assuming  $k_c = 7 \cdot 10^{12} \text{ m}^2 \text{ V}^{-1} \text{ s}^{-1}$ . In the simulation results, the magnitude of the electric field strength is higher near the surface of the implant opposite to the cancellous bone. In contrast, this high field is not noticed near the surface opposite to the cortical bone. This is because cancellous bone has a higher electric conductivity than cortical bone. At the



## 5 Numerical study of *in vivo* electro-stimulating system

early stages of the endosseous healing, a high concentration of platelets at the regions with high magnitude of the electric field strength (near the surface of the implant) is achieved. This high concentration is caused by the promotion of the migration of platelets by the electric field. That does facilitate the activation of platelets in the region of interest. After its activation, platelets start synthesizing the growth factors PDGF and TGF-, which stimulate the recruitment, migration, and proliferation of bone marrow-derived cells. Furthermore, it is reported that PDGF is a chemotactic factor for osteogenic cells [95].

5 Numerical study of *in vivo* electro-stimulating system

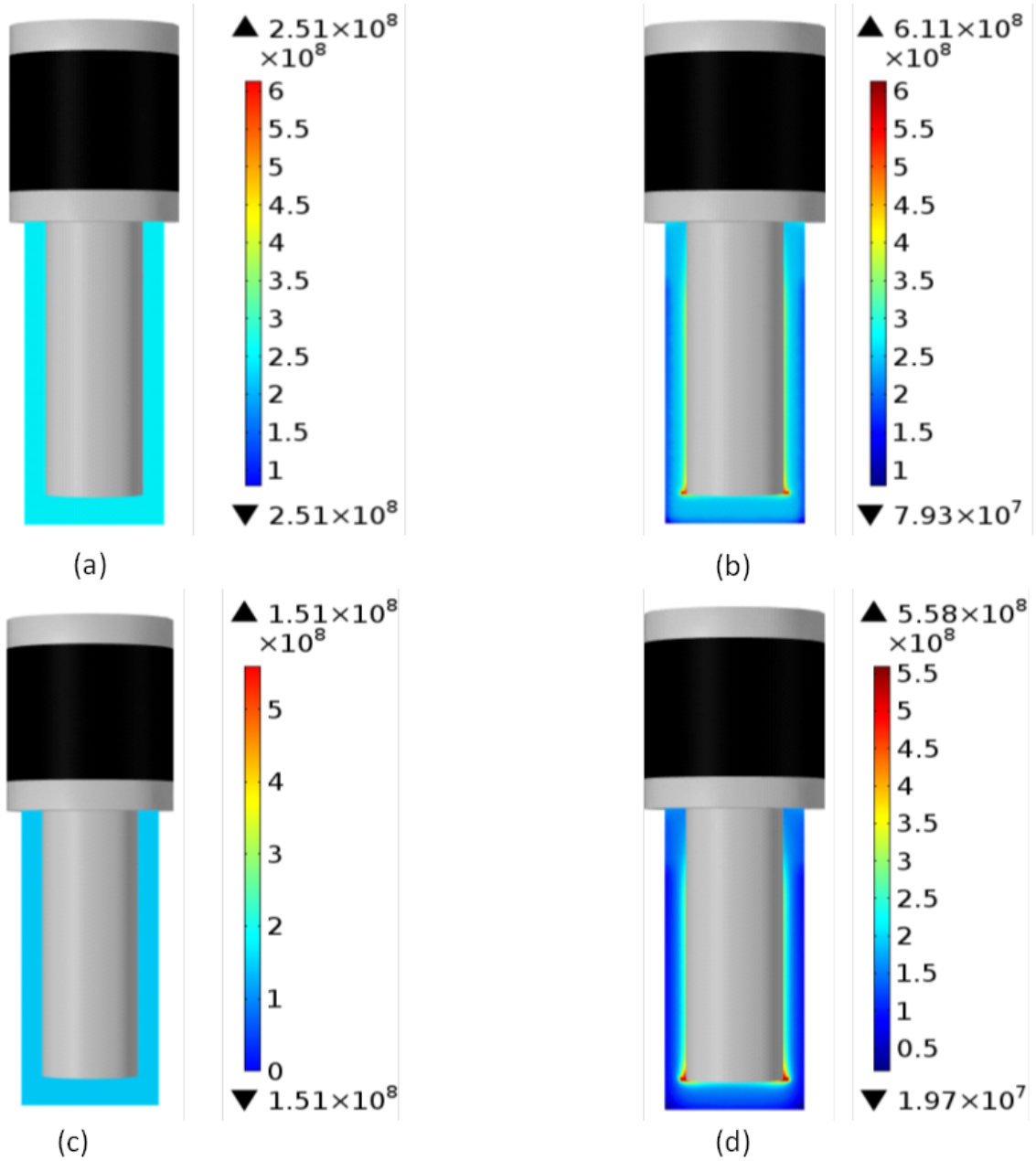


**Figure 5.4:** Density of platelets  $C$  cells/ml one day (top figure) and four days (below figure) after placement of the implant in the case of an implant without ES (a, c) and with the ES (b, d) [202].

## 6 Conclusions and outlook

### 6.1 Conclusions

Electrical stimulation is of great importance especially because of the key role it plays in promoting several physiological processes, such as fracture, peri-implant and wound healing [5]. In orthopedics, the use of electrical stimulations techniques has become significant in clinical applications since the discovery of the electric properties of the bone in the 1950s [6].

Bone healing requires a complex physiological process. Osteoblasts migration, adhesion, differentiation and proliferation play an important role in bone healing [19]. It is reported that osteoblasts respond to mechanical stimulation [20] as well as electrical stimulation [21]. However, the mechanism of the response is not well understood. The discovery of endogenous potentials by Luigi Galvani in the 18th century [22] had inspired many scientists to investigate the natural potential existence in different kinds of tissues and to apply an external electrical stimulation to enhance its functionality.

At the cellular level, the mechanism of how cells sense and respond to external electrical stimulation remains poorly understood. ES plays an important role in cellular physiology. It can interfere in cell growth, apoptosis, proliferation and migration. Focusing on electro-taxis where in most cases DC voltage is applied, cells move towards the cathode; examples of such cells are human keratinocytes [23], bovine vascular endothelial cells [24], osteoblasts [10], chondrocyte and anterior cruciate ligament fibroblasts [25]. However, it is also reported in literature that some kind of cells move towards the anode; such as keratocyte fragments [26] and osteoclasts [10].

The primary focus of the current study is to model and simulate the interactions between bone cells and electro-stimulating systems using partial differential equations. Initially, peri-implant healing is described and discussed. Secondly, a mathematical model of the coupling of reaction-diffusion models and electrical stimulation is discussed. The mathematical formulation is based on the fundamental conservation law and the different strategies of cell sensing of their external environment. Experiments are conducted in the labs in order to stimulate osteoblast-like cell line MG-63 and primary human osteoblasts. The obtained results from the experiments are used as an input to the mathematical model. Equivalent to the experimental setup, an *in silico* model i.e. a numerical model for computer simulations is implemented in some finite element-based software. Furthermore, studies are conducted to optimally

## 6 Conclusions and outlook

adapt the numerical model to the real world conditions, i.e. to minimize the relative error between the obtained results from the experimental measurements and the *in silico* model. The effect of the electric field on osteoblasts is observed. From *in vitro* to *in vivo* system, an electro-stimulating dental implant is simulated including the surrounding tissues. The first response of platelets to electrical signals is investigated. First results show that electrical stimulation could increase the number of adhered platelets to the surface of the implant, therefore improve bone ingrowth on implant surfaces.

### 6.1.1 Coupling reaction diffusion equations with electrical stimulation

According to [133], cells can sense and respond to their surrounding environments using different strategies (strictly local, neighbor based, local average, gradient based and mixed strategy). We can derive from each strategy a partial differential equation which can be used as a model to predict the interaction of the cells with an external stimulus. In our research we have assumed that the cells sense and respond to the external electrical stimulation based on the gradient strategy. The latter is widely used in chemotaxis, haptotaxis and phototaxis.

Maxwell's equations and the derived equations for the stationary current problems are described in section 3.5. These equations are implemented together with the gradient based model of the cells in the finite element-based software COMSOL MULTIPHYSICS<sup>®</sup> version 5.1.

### 6.1.2 Electro-taxis chamber construction

We have constructed an electro-taxis system in order to be able to conduct experiments on osteoblasts, hence stimulate the migration of osteoblasts using electrical stimulation. The electro-taxis chamber is designed in AutoCAD 2014 and printed in Prof. Hartmut Ewald lab using 3D printer Ultimaker 2+ 3D model. The agar bridges are prepared by filling the tubes, made of poly-vinyl chloride (PVC), with 2 % agar gel. The silver chloride coating is prepared by using the electrochemical coating technique. The resulted Ag/AgCl electrodes are used as stimulating electrodes in our experiments.

Measurements of the voltage and pH inside the electro-taxis chamber are performed. From the results we have clearly seen the benefits of agar bridges. Almost a constant pH is measured  $\text{pH}_i = 8.4$  in the area of interest, where the cells are cultured. However, in the area inside the outer reservoirs, where the medium is in direct contact with the electrodes, the  $\text{pH}_0$  decreased. After 210 minutes of applying a voltage of 15 V between the electrodes, the  $\text{pH}_0$  drops from 8.3 to 6.49. We have also observed a drop of voltages between the circular openings from 0.56 V, in the

## 6 Conclusions and outlook

initial state, to 0.45 V after 210 minutes. This small change is due to the growth of a resistive layer on the electrodes surface.

### 6.1.3 *In vitro* studies

In our experiments we have investigated two types of osteoblasts, osteoblast-like cell line MG-63 and primary human osteoblasts. The behavior of the MG-63 cells in the beginning was passive. They did not show migration and directness in the presence of the electric field although the stimulation parameters we have used are in the range reported in [164], we could not observe also any perpendicular or parallel alignment to the field vector. This could be due to the fact that the cells need more time to interact with the stimulating electric currents. Another reason could be the high concentration of cells which reduces the probability of cells to elongate and migrate. The osteoblasts cells are laid directly on the cover glasses, which may inhibit their functionality because in the bone, they used to lie on the surface of extracellular matrix [170], which is rich in collagen [171].

In the second part of the experiments, we have collaborated with the physiology department to extend our electro-taxis chamber. The modified electro-taxis chamber is mechanically stable. Experiments could be conducted up to 7 hours. The spacers are coated with collagen. The cells concentration is reduced to 15000 cells/ml.

A random movement of MG-63 cells is observed. However, a slight retraction of some cells are noticed. The behavior of the cells toward the electrical stimulation is not clear. Some cells showed directional movements toward the anode, other cells showed directional migration toward the cathode. However the direction of migration of other cells is undirected or passive. This random migration of the tracked MG-63 cells in the same environments conditions and observation field is not predictable. One reason could be that MG-63 cells need longer time of electrical stimulation to migrate. We do not have the facilities that allow us to perform further experiments for longer hours. It is not possible to refill the reservoirs regularly because the shear forces may affect the cells behavior. The agar bridges had to be changed after some hours from the start of each experiment otherwise there could be no current flowing towards the cells because they begin to melt, also air bubbles were created inside the tubes when the agarose gel heated up. We have tried to overcome these limitations but unfortunately we could not keep the track of the same cells before and after the modifications because the chamber needed to be moved from the focus of the microscope.

Osteoblast-like cell line MG-63 are often used in cells' experiments because they are available from different suppliers and show stable results while repeating experiments several times [173]. Although MG-63 cells are used as a model to primary human osteoblasts but they don't totally mimic them. In the third part we have investigated the electro-taxis of primary human osteoblasts.

After six hours and a half of electrical stimulation, primary human osteoblasts

showed directional movement. The cells migrated toward the anode. This direction of migration corresponds to the direction of the stimulating electric field. The cells migrated with an average speed of  $6.4 \mu\text{m}/\text{h}$ . However, primary human osteoblasts in the absence of the electrical stimulation showed a random behavior.

### 6.1.4 Electric field strength and cells populations simulations

Three dimensional electro-taxis chamber with electrodes is designed in AutoCAD 2014 and then imported to COMSOL MULTIPHYSICS<sup>®</sup>. The electrical conductivities of the components of the electro-taxis chamber, PLA, silver electrodes, culture medium and agar-bridges are taken from literature. A convergence study is performed and the chosen mesh for the simulation has  $0.22 \cdot 10^6$  degrees of freedom. The simulation results are compared to our experimental measurements. We have observed a difference between the measured electric field amplitudes and the simulated ones, depending on the applied voltage. The relative error reached up to  $e_E = 68 \%$ . The reason of this difference is the voltage drop, which results from the resistive layer of the silver chloride which is created at the surface silver/electrolyte as mentioned previously. We have improved our model by implementing the resistive layer of silver chloride on both electrodes. The thickness of the layer is taken from literature  $20 \mu\text{m}$ . A parametric study is performed to define the resistivity of the Ag/Cl layer, the smallest average relative error is equal to 0.071. This average relative error corresponds to the AgCl resistivity of  $R_{f6} = 2.1 \cdot 10^3 \Omega\text{m}$ . This value falls in the range reported in literature. We could rather achieve a good approximation of the electric field amplitudes after modelling the electric double layer by the resistive layer.

The reaction-diffusion model of primary human osteoblasts in the presence of the electrical stimulus is simulated. The temporal evolution of the population of primary human osteoblasts inside the culture medium is observed. The model parameters, sensitivity function, directness parameter and initial concentration are estimated from our *in vitro* experiments. The resistive layer of AgCl formed at the silver electrodes interface is implemented. After applying the electrical stimulation to the primary human osteoblasts, a remarkable effect of the electric field on the cells migration could be observed. From the temporal evolution of the primary human osteoblasts concentration we could draw conclusions about the movement of cells. The ES pushes the cells to move toward the direction of the anode.

### 6.1.5 *In vivo* studies

In this part, we have modeled a 3D dental implant which is adapted from the one that is described in literature [120]. The electro-stimulating dental implant is inserted into the mandible of a dog. We propose a 3D model composed of the electronic

## 6 Conclusions and outlook

dental implant, made of titanium, and the surrounding tissue, i.e. saliva, cortical bone, cancellous bone and blood.

Platelets sensitivity to the electric potential gradient is presented by the parameter  $k_c$ . First results are obtained assuming  $k_c = 7 \cdot 10^{-12} \text{ m}^2 \text{V}^{-1} \text{s}^{-1}$ . In the simulation results, the magnitude of the electric field strength is higher near the surface of the implant opposite to the cancellous bone. In contrast, this high field is not noticed near the surface opposite to the cortical bone. This is because cancellous bone has a higher electric conductivity than cortical bone. The parameter estimation of the decay rate of platelets  $A_c$  is in accordance with the half-life time reported in [204]. At the early stages of the endosseous healing, a high concentration of platelets at the regions with high magnitude of the electric field strength (surface of the implant) is achieved. This high concentration is caused by the promotion of the migration of platelets by the electric field. That does facilitate the activation of platelets in the region of interest. After its activation, platelets start synthesizing the growth factors PDGF and TGF- $\beta$ , which stimulate the recruitment, migration and proliferation of bone marrow-derived cells. Thus, they promote bone formation.

## 6.2 Outlook

### 6.2.1 The effect of surface roughness and topography on bone cells

Surface topography and roughness play a very important role in biomaterials. Beside the mechanical stability that they provide to implants [207], they also have a remarkable effect on single cell activity. Different average surface roughness of titanium have been experimentally shown to have an influence on differentiation of primary osteoblasts, which have been derived from human mandibular. An average roughness of  $3 \mu\text{m}$  is a convenient parameter in promoting osteoblasts differentiation [208]. In another study [209], they were able to determine the optimal surface roughness for the attachment, differentiation and proliferation of bone cells. Beside the surface roughness, electrical stimulation could be investigated as a second parameter. Based on the previous work on optimal surface roughness, adding the ES to the experimental system could be a challenge to find the optimal parameter combination for better osseointegration of bone cells on metallic implants. Different surface topographies could be used to determine their specific impact (in the sense of advantages) on osteoblasts. A random surface is generated, see figure A.6 using COMSOL MULTIPHYSICS<sup>®</sup> version 5.1 to illustrate the procedure of this part. Similarly, specific surface topographies obtained from atomic-force microscopy (AFM) could be imported to the original model. Special care has to be taken to ensure a good quality of the mesh especially around the sharp edges. A correlation between the specific surface roughness and the electric field strength could be determined as well

as to the biological activity of osteoblasts. The aim is to derive some general rules.

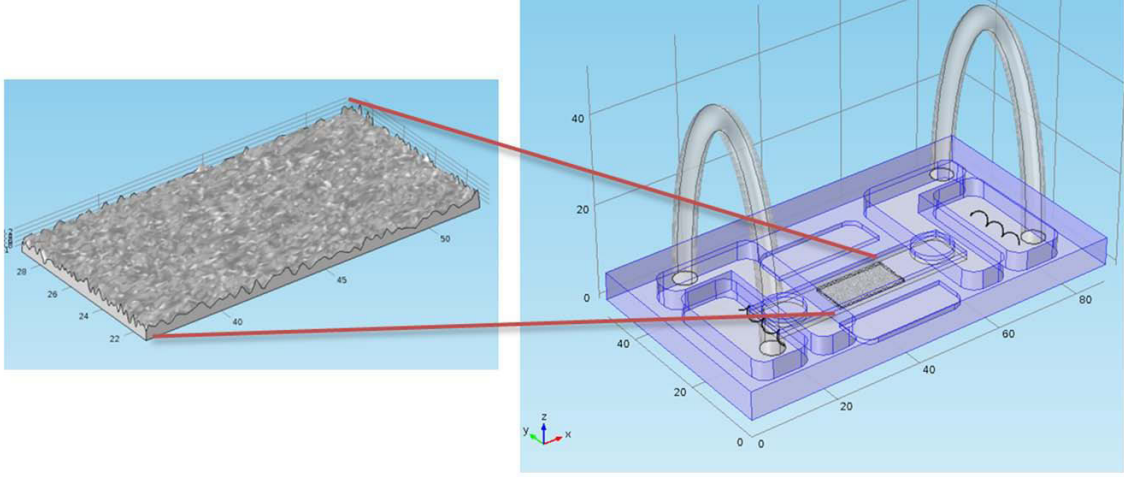


**Figure 6.1:** Generation of three-dimensional rough surface using COMSOL MULTIPHYSICS® version 5.1. B: Adding the rough surface to the original stimulating system.

### 6.2.2 Numerical studies on osteoblasts using a reaction-diffusion model

The results obtained from the previous experiments could be used as an input for this research. The effect of electrical stimulation on primary osteoblasts have to be mathematically modeled. Reaction-diffusion equations, see equation (6.1) are used to describe the migration, differentiation and proliferation of the cells. The electric field strength obtained from the simulation of the electro-taxis chamber could be used as an input into the reaction-diffusion equation, which is described as follows:

$$\frac{\partial C}{\partial t} = (D \nabla^2 C + Cg(ES, R)p(ES)) + f(C, ES, R) \quad (6.1)$$

with the concentration of cells  $C = C(x, t)$  at time  $t$  and the spatial position  $x$ , the cells diffusion coefficient  $D$ , the sensitivity function of the cells to external electrical stimulation ( $ES$ ) and surface roughness  $g(ES, R)$ , which in general is dependent on the environmental cues. The function  $g(ES)$  increases with the increase of the magnitude of the electric field strength up to a certain point, where the increase in electrical field strength has no more influence on the speed of the cells. After that point, the electric field could have an inverse effect on the speed of cells. Surface roughness  $R$  should be then included as an extra factor ( $g(ES, R)$ ). The parameters presented in equation (6.1) could be estimated from the experimental results. The sensitivity function  $g(ES, R)$  is modeled as a logistic function in order to define the



## 6 *Conclusions and outlook*

relationship between the electric field strength and surface roughness on one side and the speed, proliferation and differentiations of cells on the other side. The parameters of both functions,  $g(ES, R)$  and  $f(C, ES, R)$ , which holds apoptosis, proliferation and differentiation of osteoblasts, could be determined depending on the findings of the experiments. Different mathematical forms of reaction-diffusion models could also be investigated. Equation (6.1) describes a model based on the assumption that the cells sense the gradient of its surrounding, other sensing strategies could be also investigated like strictly local, neighbor based, local average and mixed model sensing strategies, see section 3.3.1.

# A Appendix

## A.1 The main steps followed to model a combined stationary and transient system

The following section provides the main steps followed to model combined stationary and transient system in COMSOL MULTIPHYSICS<sup>®</sup> version 5.1.

### Adding global parameters

The parameters used in the model can be defined in a top level (global parameters). These parameters can be used in geometry operations, mesh generators, physics interface and evaluating results<sup>4</sup>.

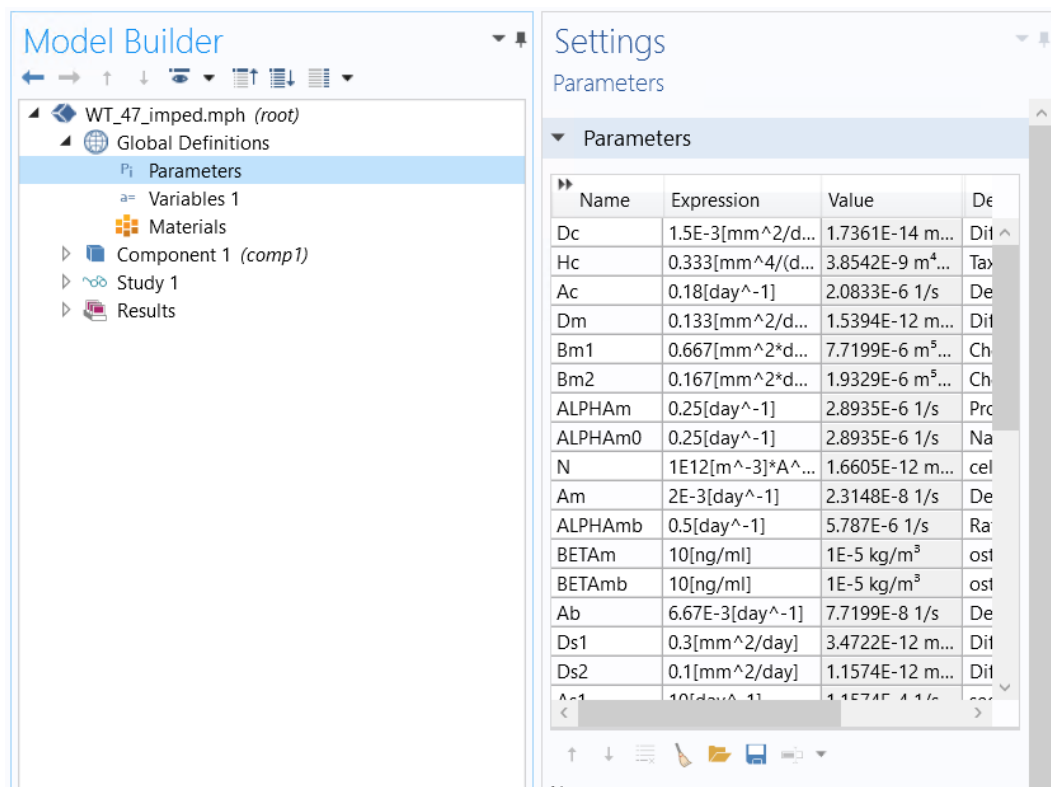
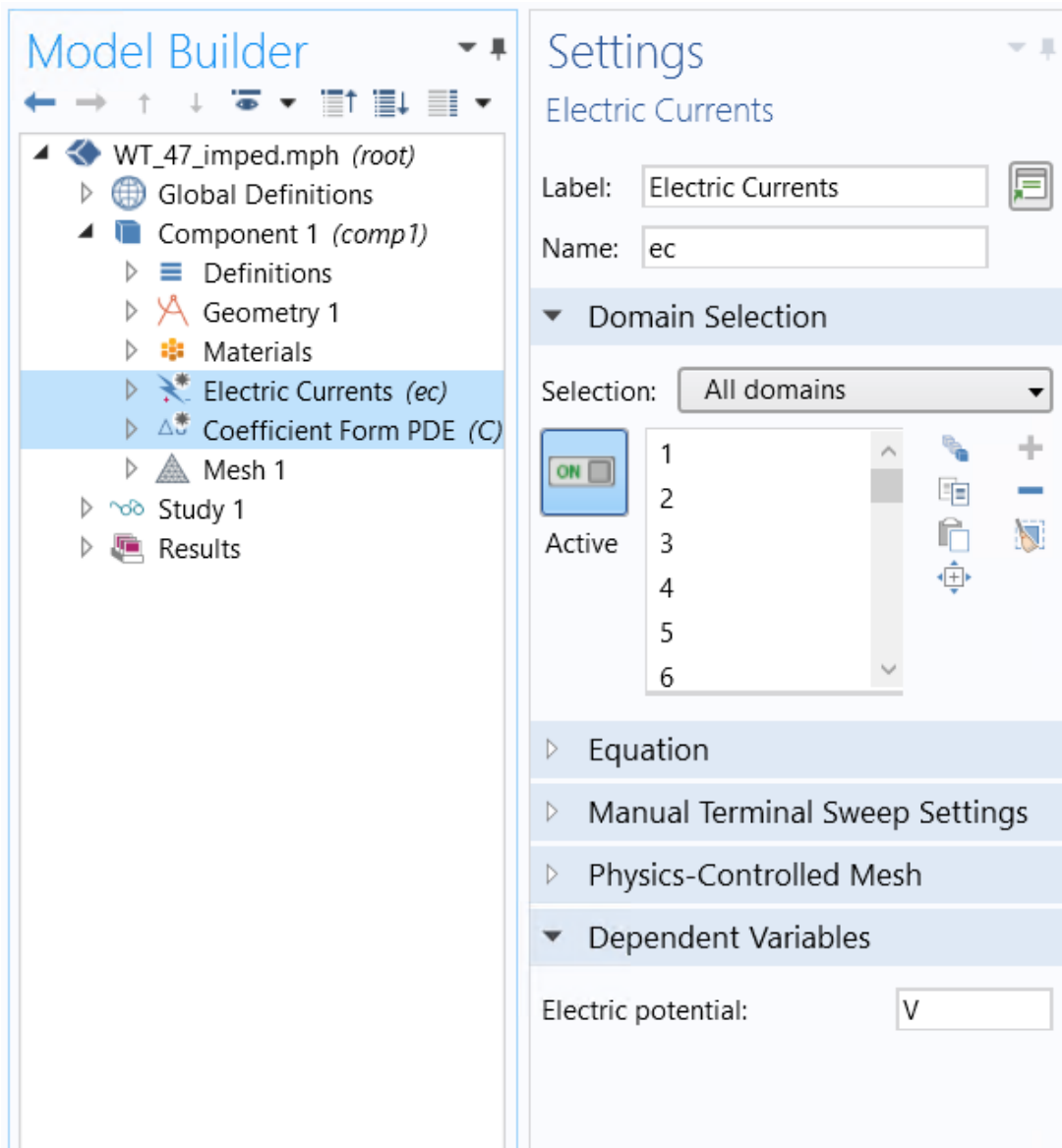


Figure A.1: Global parameters.

<sup>4</sup>[http://elliott:8090/docserver/#!/com.comsol.help.comsol/comsol\\_ref\\_definitions.12.009.html?type=ext](http://elliott:8090/docserver/#!/com.comsol.help.comsol/comsol_ref_definitions.12.009.html?type=ext)

### Adding physics interfaces

Here, we add the appropriate physics to the component. The electric currents (ec) interface is used to model the electric current flow in the electro-taxis system. It can be added from the AC/DC branch. The coefficient form PDE (C) is used to model the temporal evolution of primary human osteoblasts inside the culture medium. It can be found under the mathematics PDE interfaces branch. The physics interfaces are shown below.



**Figure A.2:** Adding physics interfaces. Electric currents (ec) and coefficient form PDE (C) interfaces are highlighted.

## A Appendix

The whole computational domain is defined by selecting the domains for the electric currents interface. The boundaries for the terminal, electric insulator and ground are selected. The applied voltage can be assigned to the terminal and ground. In the electro-taxis system, a potential of 25 V is assigned to the anode (terminal). The cathode is connected to ground (0 V). At the electric insulator no electric current flows into the boundary<sup>5</sup>.

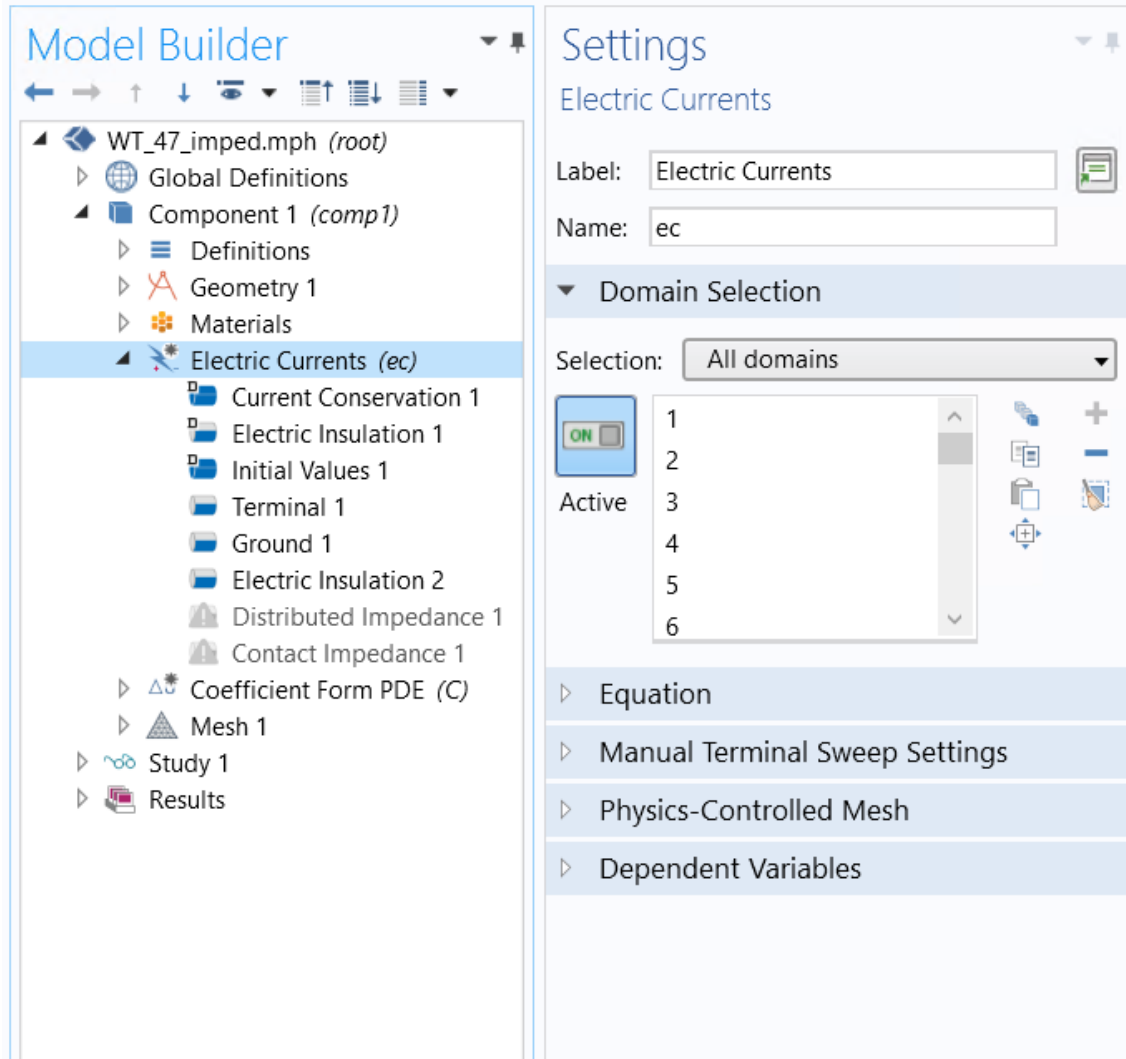


**Figure A.3:** The electric currents interface (ec).

The whole computational domain is defined by selecting the domains for the coefficient form PDE (C) interface. The nodes: coefficient form PDE, zero flux, and initial

<sup>5</sup>[http://elliott:8090/docserver/#!/com.comsol.help.acdc/acdc\\_ug\\_electric\\_fields.07.48.html?type=ext](http://elliott:8090/docserver/#!/com.comsol.help.acdc/acdc_ug_electric_fields.07.48.html?type=ext)

## A Appendix

model builder are added by default. The values zero flux boundaries are selected, which means zero flux of primary osteoblasts cross the boundaries <sup>6</sup>. A uniform concentration of the primary human osteoblasts is defined at the initial state. Values or expressions can be entered for the PDE coefficients, e.g. diffusion coefficient.

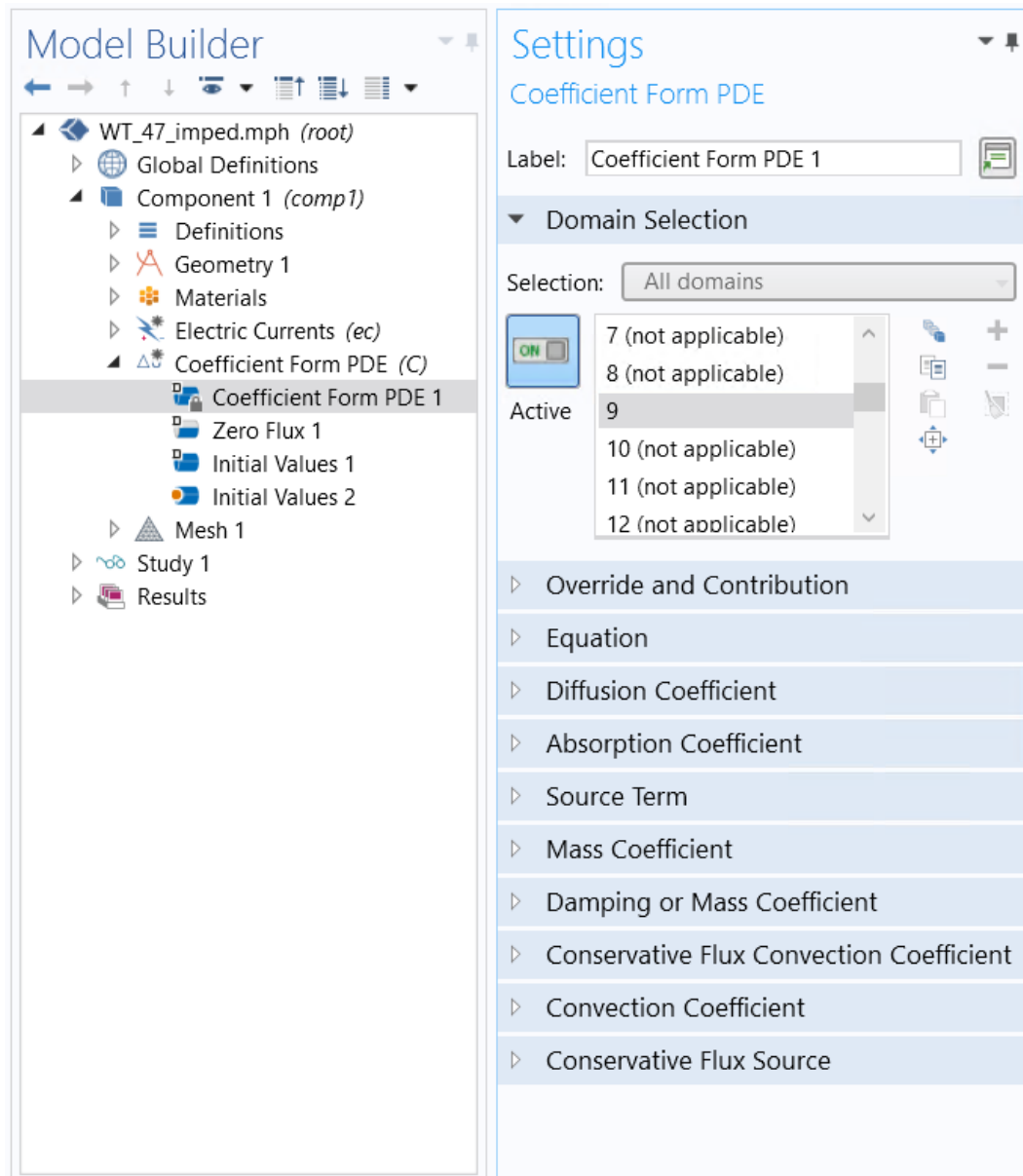


**Figure A.4:** The coefficient form PDE (C) interface.

<sup>6</sup>[http://elliott:8090/docserver/#!/com.comsol.help.comsol/comsol\\_ref\\_equationbased.23.035.html?type=ext](http://elliott:8090/docserver/#!/com.comsol.help.comsol/comsol_ref_equationbased.23.035.html?type=ext)

### Mesh generation

After importing the geometry and defining the physics, the next step is to generate the mesh. Before building the mesh, we can choose the type and the size of the mesh elements. The mesh is refined at the short edges and smaller faces by choosing a small value of the minimum element size, in our case the minimum element size is set to 0.35 mm. This value of the minimum element size must be smaller than the smallest edge or face of the model to make sense and thus also avoid warnings when generating the mesh.

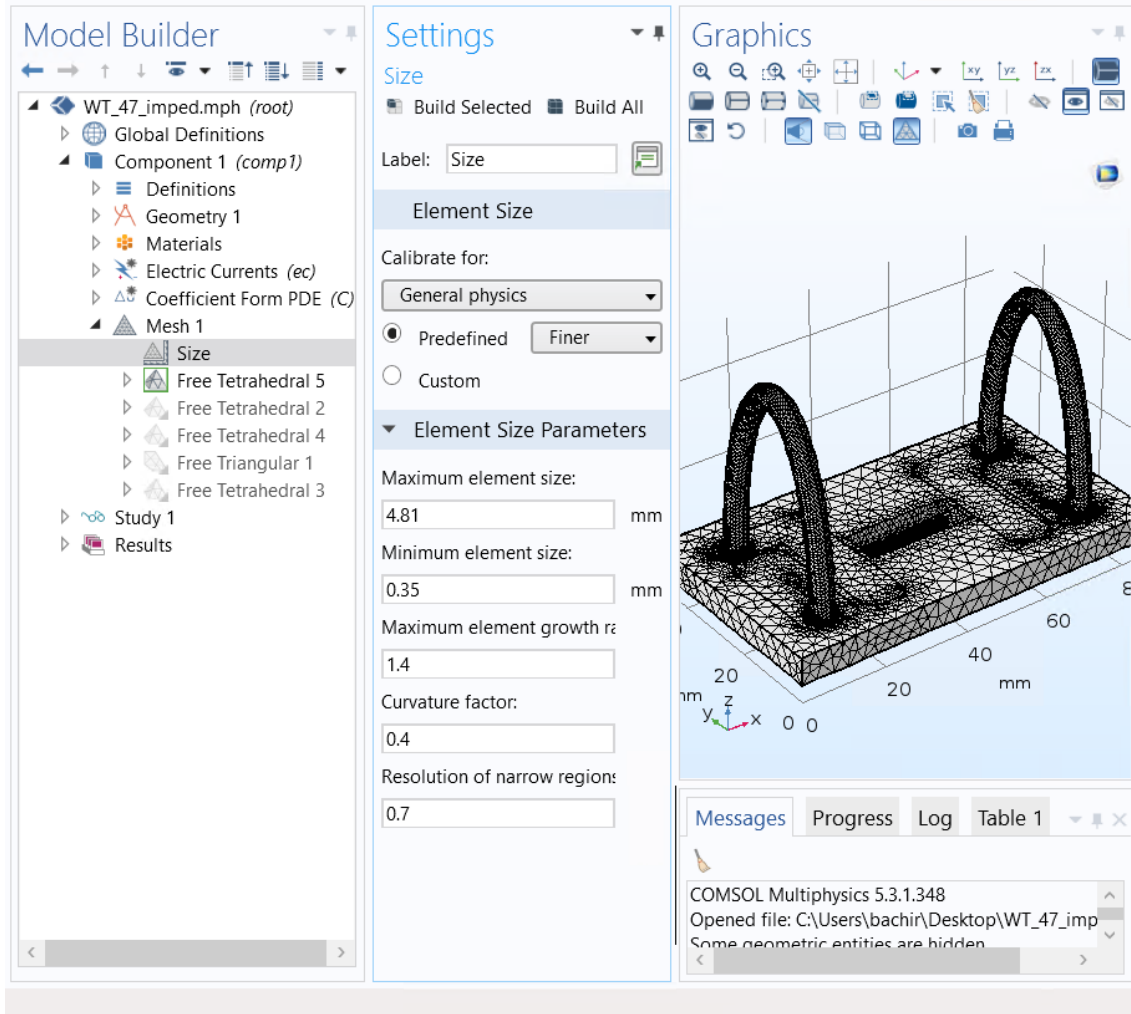


Figure A.5: Mesh generation.

### Defining the study steps

Finally, we define how to solve the model. This is done in the study node. We use the parameter sweep in case we want to study the influence of a parameter on the solution, e.g. the resistivity of the silver chloride AgCl layer. Two study steps are

## A Appendix

defined in order to solve the stationary and transient problem separately. The order of study steps is important, stationary problem is solved first and next the transient problem. In the solver configuration node we can define the solver configuration for each study.

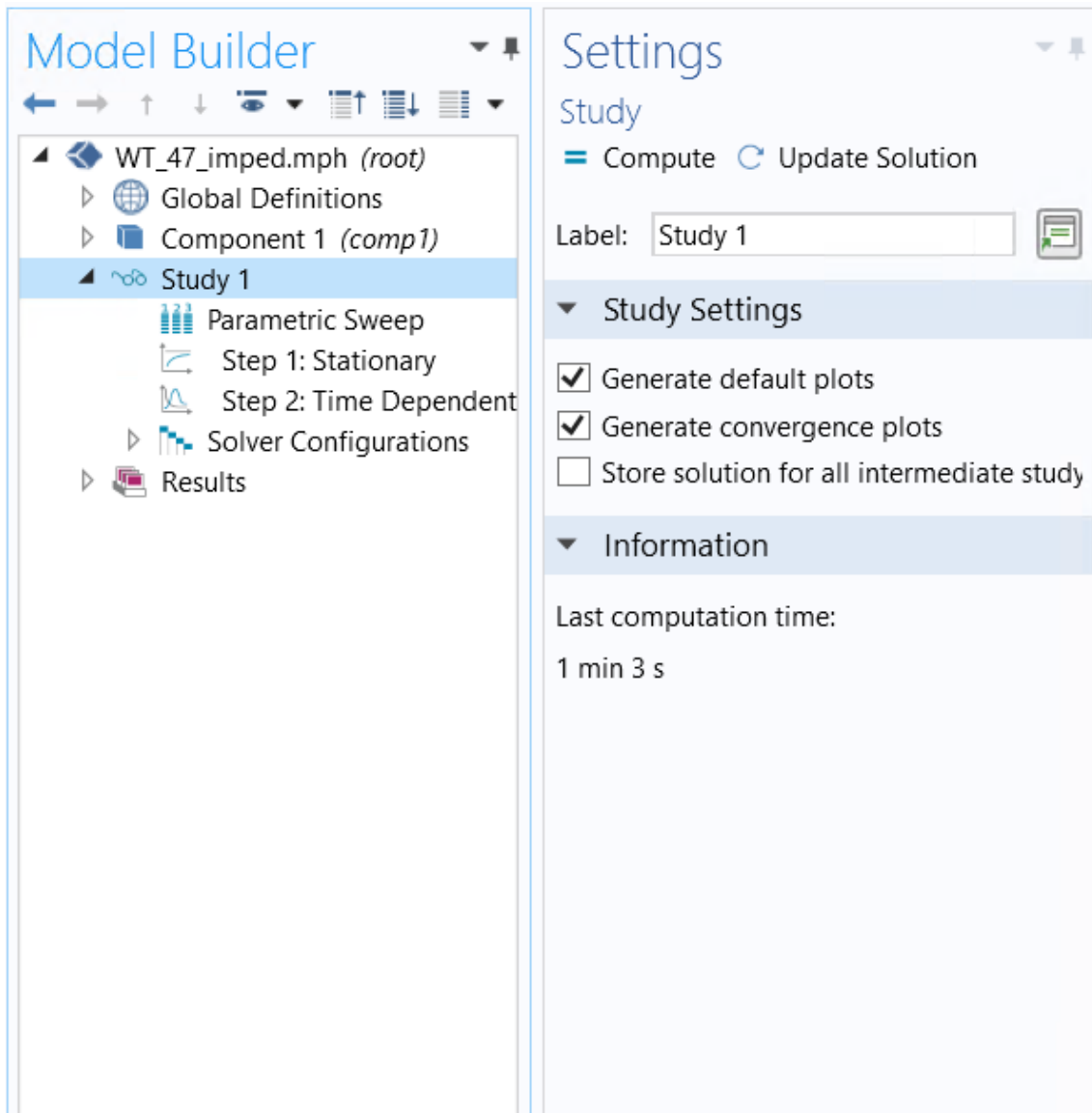


**Figure A.6:** The study node.

## Bibliography

- [1] K. Anselme, “Biomaterials and interface with bone,” *Osteoporosis International*, vol. 22, no. 6, p. 2037, 2011.
- [2] P. Moreo, J. M. Garca-Aznar, and M. Doblar, “Bone ingrowth on the surface of endosseous implants. Part 1: Mathematical model,” *Journal of Theoretical Biology*, vol. 260, pp. 1–12, Sept. 2009.
- [3] M. E. Mycielska and M. B. A. Djamgoz, “Cellular mechanisms of direct-current electric field effects: galvanotaxis and metastatic disease,” *Journal of Cell Science*, vol. 117, no. 9, pp. 1631–1639, 2004.
- [4] S. E. Lyshevski, ed., *Dekker Encyclopedia of Nanoscience and Nanotechnology, Third Edition*. CRC Press, Mar. 2014. DOI: 10.1081/E-ENN3.
- [5] L. Kloth and J. McCulloch, “Promotion of wound healing with electrical stimulation,” *Advances in wound care : the journal for prevention and healing*, vol. 9, no. 5, pp. 42–45, 1996.
- [6] J. Ryaby, “Clinical effects of electromagnetic and electric fields on fracture healing,” *Clinical orthopaedics and related research*, vol. 355S, pp. S205–15, 11 1998.
- [7] I. Yasuda, “Piezoelectricity of living bone,” *J. Kyoto. Pref. Univ. Med.*, p. 53:325, 1953.
- [8] R. Brand and L. Claes, “The law of bone remodelling: Lulus wolff, translated by p. maquet and r. furlong, springer, 1986, dm 188, 126 pp,” *Journal of Biomechanics*, vol. 22, no. 2, pp. 185 – 187, 1989.
- [9] R. Carmona, “Bone health and osteoporosis: a report of the surgeon general. u.s. department of health and human services, office of the surgeon general, rockville, md, usa,” *The Osteoporosis Report*, 01 2004.
- [10] C. A. L. Bassett, R. J. Pauluk, and R. O. Becker, “Effects of electric currents on bone in vivo,” *Nature*, vol. 204, no. 4959, pp. 652–654, 1964.
- [11] C. Brighton, Z. Friedenber, J. Black, J. J. Esterhai, J. Mitchell, and F. J. Montique, “Electrically induced osteogenesis: relationship between charge, current density, and the amount of bone formed: introduction of a new cathode



## Bibliography

- concept.,” *Clinical orthopaedics and related research*, vol. 161, pp. 122–132, 1981.
- [12] Y. S. Shayesteh, B. Eslami, M. M. Dehghan, H. Vaziri, M. Alikhassi, A. Mangoli, and A. Khojasteh, “The Effect of a Constant Electrical Field on Osseointegration after Immediate Implantation in Dog Mandibles: A Preliminary Study,” *Journal of Prosthodontics*, vol. 16, pp. 337–342, Sept. 2007.
- [13] D. C. Paterson, G. N. Lewis, and C. A. Cass, “Treatment of delayed union and nonunion with an implanted direct current stimulator.,” *Clinical orthopaedics and related research*, vol. 148, pp. 117–128, 1980.
- [14] C. T. Brighton and R. M. Hunt, “Ultrastructure of electrically induced osteogenesis in the rabbit medullary canal,” *Journal of orthopaedic research*, vol. 4, no. 1, pp. 27–36, 1986.
- [15] C. A. L. Bassett, “Beneficial effects of electromagnetic fields,” *Journal of cellular biochemistry*, vol. 51, no. 4, pp. 387–393, 1993.
- [16] C. Brighton, J. Cronkey, and A. Osteman, “In vitro epiphyseal-plate growth in various constant electrical fields,” *Journal of Bone & Joint Surgery - American*, vol. 58(7), pp. 971–8, Oct. 1976.
- [17] M. Collier, F. Kallfelz, V. Rendano, L. Krook, and H. Schryver, “Capacitively coupled electrical stimulation of bone healing in the horse: in vivo study with a salter type iv osteotomy model with stainless steel surface electrodes.,” *American Journal of Veterinary Research*, vol. 46, no. 3, pp. 622–631, 1985.
- [18] R. Abeed, M. Naseer, and E. Abel, “Capacitively coupled electrical stimulation treatment: Results from patients with failed long bone fracture unions,” *Journal of Orthopaedic Trauma*, vol. 12, no. 7, pp. 510–513, 1998.
- [19] I. Hvid, J. Horn, S. Huhnstock, and H. Steen, “The biology of bone lengthening,” *Journal of Children’s Orthopaedics*, vol. 10, pp. 487–492, Dec. 2016.
- [20] J. S. Khurana, *Bone Pathology*. New York: Humana Press, 1 ed., 2009.
- [21] S. Meng, Z. Zhang, and M. Rouabhia, “Accelerated osteoblast mineralization on a conductive substrate by multiple electrical stimulation,” *Journal of Bone and Mineral Metabolism*, vol. 29, no. 5, pp. 535–544, 2011.
- [22] M. Piccolino, “Animal electricity and the birth of electrophysiology: the legacy of Luigi Galvani,” *Brain research bulletin*, vol. 46, no. 5, pp. 381–407, 1998.

## Bibliography

- [23] K. Y. Nishimura, R. R. Isseroff, and R. Nuccitelli, "Human keratinocytes migrate to the negative pole in direct current electric fields comparable to those measured in mammalian wounds," *Journal of Cell Science*, vol. 109, no. 1, pp. 199–207, 1996.
- [24] X. L. J. Kolega, "Effects of direct current electric fields on cell migration and actin filament distribution in bovine vascular endothelial cells," *J Vasc Res*, vol. 39, pp. 391–404, 2002.
- [25] P.-H. G. Chao, H. H. Lu, C. T. Hung, S. B. Nicoll, and J. C. Bulinski, "Effects of Applied DC Electric Field on Ligament Fibroblast Migration and Wound Healing," *Connective Tissue Research*, vol. 48, pp. 188–197, Jan. 2007.
- [26] Y. Sun, H. Do, J. Gao, R. Zhao, M. Zhao, and A. Mogilner, "Keratocyte Fragments and Cells Utilize Competing Pathways to Move in Opposite Directions in an Electric Field," *Current Biology*, vol. 23, pp. 569–574, Apr. 2013.
- [27] N. Orida and J. D. Feldman, "Directional protrusive pseudopodial activity and motility in macrophages induced by extracellular electric fields," *Cell Motility*, vol. 2, no. 3, pp. 243–255, 1982.
- [28] P. Kuzyk and E. Schemitsch, "The basic science of peri-implant bone healing," *Indian journal of orthopaedics*, vol. 45, pp. 108–15, 03 2011.
- [29] C. N. Elias, "Factors affecting the success of dental implants," in *Implant Dentistry* (I. Turkyilmaz, ed.), ch. 14, Rijeka: IntechOpen, 2011.
- [30] M. Ring, "A thousand years of dental implants: a definitive history—part 1.," *Compendium of continuing education in dentistry (Jamesburg, N.J. : 1995)*, vol. 16, no. 10, pp. 1060, 1062, 1064 passim, 1995.
- [31] A. Garg, *Implant Dentistry*. Elsevier Health Sciences, 2009.
- [32] U. Breine, B. Johansson, P. Roylance, H. Roeckert, and J. Yoffey, "Regeneration of bone marrow. a clinical and experimental study following removal of bone marrow by curettage.," *Acta anatomica*, vol. 59, pp. 1–46, 1964.
- [33] A. Piattelli and G. Iezzi, "Dental stem cells: Regenerative potential," ch. MSCs and Biomaterials, pp. 241–252, Cham: Springer International Publishing, 2016.
- [34] S. A. W. Pickering and B. E. Scammell, "Electromagnetic fields for bone healing," *The international journal of lower extremity wounds*, vol. 1, no. 3, pp. 152–160, 2002.

## Bibliography

- [35] C. Potratz, D. Kluess, H. Ewald, and U. van Rienen, “Multiobjective optimization of an electrostimulative acetabular revision system,” *IEEE Transactions on Biomedical Engineering*, vol. 57, pp. 460–468, Feb 2010.
- [36] C., U. Zimmermann, and U. van Rienen, “Modeling of an optimized electrostimulative hip revision system under consideration of uncertainty in the conductivity of bone tissue,” *IEEE Journal of Biomedical and Health Informatics*, vol. 19, pp. 1321–1330, July 2015.
- [37] H. W. Pau, A. Grünbaum, K. Ehrt, R. Dahl, T. Just, and U. van Rienen, “Would an endosteal CI-electrode make sense? Comparison of the auditory nerve excitability from different stimulation sites using esrt measurements and mathematical models,” *European Archives of Oto-Rhino-Laryngology*, vol. 271, pp. 1375–1381, Jun 2014.
- [38] M. D. Bajin, O. Savas, F. Aslan, and L. Sennaroglu, “Cochlear Implantation in Neurobrucellosis,” *Balkan Medical Journal*, vol. 33, pp. 108–111, Feb. 2016.
- [39] C. Schmidt and U. van Rienen, “Modeling the field distribution in deep brain stimulation: The influence of anisotropy of brain tissue,” *IEEE Transactions on Biomedical Engineering*, vol. 59, pp. 1583–1592, June 2012.
- [40] C. Schmidt, P. Grant, M. Lowery, and U. van Rienen, “Influence of uncertainties in the material properties of brain tissue on the probabilistic volume of tissue activated,” *IEEE Transactions on Biomedical Engineering*, vol. 60, pp. 1378–1387, May 2013.
- [41] M. Brignole, A. Auricchio, G. Baron-Esquivias, P. Bordachar, G. Boriani, O.-A. Breithardt, J. Cleland, J.-C. Deharo, V. Delgado, P. Elliott, B. Gorenek, C. Israel, C. Leclercq, C. Linde, L. Mont, L. Padeletti, R. Sutton, P. Vardas, J. Zamorano, S. Achenbach, H. Baumgartner, J. Bax, H. Bueno, V. Dean, C. Deaton, C. Erol, R. Fagard, R. Ferrari, D. Hasdai, A. Hoes, P. Kirchhof, J. Knuuti, P. Kolh, P. Lancellotti, A. Linhart, P. Nihoyannopoulos, M. Piepoli, P. Ponikowski, P. Sirnes, J. Tamargo, M. Tendera, A. Torbicki, W. Wijns, S. Windecker, P. Kirchhof, C. Blomstrom-Lundqvist, L. Badano, F. Aliyev, D. Bnsch, H. Baumgartner, W. Bsata, P. Buser, P. Charron, J.-C. Daubert, D. Dobreanu, S. Faerestrand, D. Hasdai, A. Hoes, J.-Y. Le Heuzey, H. Mavrakis, T. McDonagh, J. Merino, M. Nawar, J. Nielsen, B. Pieske, L. Poposka, F. Ruschitzka, M. Tendera, I. Van Gelder, and C. Wilson, “213 ESC Guidelines on cardiac pacing and cardiac resynchronization therapy,” *European Heart Journal*, vol. 34, no. 29, pp. 2281–2329, 2013.
- [42] C. Valzania, A. Torbica, R. Tarricone, F. Leyva, and G. Boriani, “Implant rates of cardiac implantable electrical devices in europe: A systematic literature review,” *Health Policy*, vol. 120, no. 1, pp. 1 – 15, 2016.

## Bibliography

- [43] S. A. Pickering and B. E. Scammell, “Electromagnetic fields for bone healing,” *The International Journal of Lower Extremity Wounds*, vol. 1, no. 3, pp. 152–160, 2002.
- [44] J. Belinha, *Meshless Methods in Biomechanics: Bone Tissue Remodelling Analysis*, ch. Bone Tissue Remodelling Analysis, pp. 251–316. Cham: Springer International Publishing, 2014.
- [45] M. Mullender, R. Huiskes, and H. Weinans, “A physiological approach to the simulation of bone remodeling as a self-organizational control process,” *Journal of Biomechanics*, vol. 27, no. 11, pp. 1389 – 1394, 1994.
- [46] J. S. Lowe, P. G. Anderson, and A. Stevens, *Stevens & Lowe’s human histology*. Philadelphia, PA: Elsevier/Mosby, fourth edition ed., 2015.
- [47] D. J. Ortner and G. Turner-Walker, “Chapter 2 - the biology of skeletal tissues,” in *Identification of Pathological Conditions in Human Skeletal Remains (Second Edition)* (D. J. Ortner, ed.), pp. 11 – 35, San Diego: Academic Press, second edition ed., 2003.
- [48] S. Puckett, R. Pareta, and T. J. Webster, “Nano rough micron patterned titanium for directing osteoblast morphology and adhesion,” *International Journal of Nanomedicine*, vol. 3, no. 2, pp. 229–241, 2008.
- [49] M. Niinomi, T. Narushima, and M. Nakai, eds., *Advances in metallic biomaterials: processing and applications*. No. 4 in Springer series in biomaterials science and engineering, Heidelberg: Springer, 2015.
- [50] M. Capulli, R. Paone, and N. Rucci, “Osteoblast and osteocyte: games without frontiers.,” *Archives of biochemistry and biophysics*, vol. 561, pp. 3–12, 2014.
- [51] D. Burr, T. Bellido, and K. White, “Bone structure and function,” in *Rheumatology: Sixth Edition*, vol. 1-2, pp. 42–55, Elsevier Inc., 6 2014.
- [52] V. Everts, J. M. Delaiss, W. Korper, D. C. Jansen, W. Tigchelaar-Gutter, P. Saftig, and W. Beertsen, “The Bone Lining Cell: Its Role in Cleaning Howship’s Lacunae and Initiating Bone Formation,” *Journal of Bone and Mineral Research*, vol. 17, pp. 77–90, Jan. 2002.
- [53] J. L. Brown, S. G. Kumbar, and C. T. Laurencin, “Chapter ii.6.7 - bone tissue engineering,” in *Biomaterials Science (Third Edition)* (B. D. Ratner, A. S. Hoffman, F. J. Schoen, and J. E. Lemons, eds.), pp. 1194 – 1214, Academic Press, third edition ed., 2013.

## Bibliography

- [54] T. A. Franz-Odenaal, B. K. Hall, and P. E. Witten, “Buried alive: How osteoblasts become osteocytes,” *Developmental Dynamics*, vol. 235, no. 1, pp. 176–190, 2006.
- [55] R. Florencio-Silva, G. R. d. S. Sasso, E. Sasso-Cerri, M. J. Simes, and P. S. Cerri, “Biology of Bone Tissue: Structure, Function, and Factors That Influence Bone Cells,” *BioMed Research International*, vol. 2015, pp. 1–17, 2015.
- [56] R. B. Sher, G. A. Cox, and C. Ackert-Bicknell, “Chapter 2.5 - development and disease of mouse muscular and skeletal systems,” in *The Laboratory Mouse (Second Edition)* (H. J. Hedrich, ed.), pp. 209 – 239, Boston: Academic Press, second edition ed., 2012.
- [57] R. Sher, G. Cox, and C. Ackert-Bicknell, “Development and disease of mouse muscular and skeletal systems,” *The Laboratory Mouse*, pp. 209–239, 12 2012.
- [58] S. L. Dallas, M. Prideaux, and L. F. Bonewald, “The osteocyte: an endocrine cell ... and more,” *Endocrine reviews*, vol. 34, pp. 658–690, Oct 2013.
- [59] T. Cundy, I. R. Reid, and A. Grey, “Chapter 31 - metabolic bone disease,” in *Clinical Biochemistry: Metabolic and Clinical Aspects (Third Edition)* (W. J. Marshall, M. Lapsley, A. P. Day, and R. M. Ayling, eds.), pp. 604 – 635, Churchill Livingstone, third edition ed., 2014.
- [60] T. Wallace, *Dietary Bioactives and Bone Health*. MDPI AG, 2018.
- [61] J. Feher, “9.8 - calcium and phosphorus homeostasis ii: Target tissues and integrated control,” in *Quantitative Human Physiology (Second Edition)* (J. Feher, ed.), pp. 933 – 945, Boston: Academic Press, second edition ed., 2017.
- [62] D. L. Stocum, “Chapter 8 - regeneration of appendages,” in *Regenerative Biology and Medicine (Second Edition)* (D. L. Stocum, ed.), pp. 183 – 226, San Diego: Academic Press, second edition ed., 2012.
- [63] Y. Tanaka, S. Nakayamada, and Y. Okada, “Osteoblasts and osteoclasts in bone remodeling and inflammation,” *Current Drug Targets. Inflammation and Allergy*, vol. 4, pp. 325–328, June 2005.
- [64] S. Standring, H. Ellis, and C. Wigley, *Gray’s anatomy : the anatomical basis of clinical practice*. Elsevier Churchill Livingstone, 39 ed., 2005.
- [65] B. Clarke, “Normal bone anatomy and physiology,” *Clinical Journal of the American Society of Nephrology*, vol. 3, no. Supplement 3, pp. S131–S139, 2008.

## Bibliography

- [66] D. H. Copp and S. S. Shim, “The homeostatic function of bone as a mineral reservoir,” *Oral Surgery, Oral Medicine, and Oral Pathology*, vol. 16, pp. 738–744, June 1963.
- [67] J.-Y. Rho, L. Kuhn-Spearing, and P. Zioupos, “Mechanical properties and the hierarchical structure of bone,” *Medical Engineering and Physics*, vol. 20, no. 2, pp. 92 – 102, 1998.
- [68] D. K. Dubey and V. Tomar, “Role of hydroxyapatite crystal shape in nanoscale mechanical behavior of model tropocollagenhydroxyapatite hard biomaterials,” *Materials Science and Engineering: C*, vol. 29, no. 7, pp. 2133 – 2140, 2009.
- [69] C. Gao, S. Peng, P. ying Feng, and C. Shuai, “Bone biomaterials and interactions with stem cells,” in *Bone Research*, 2017.
- [70] A. M. Weatherholt, R. K. Fuchs, and S. J. Warden, “Specialized connective tissue: bone, the structural framework of the upper extremity,” *Journal of hand therapy : official journal of the American Society of Hand Therapists*, vol. 25, no. 2, pp. 123–132, 2012.
- [71] Ö. Kalenderer and A. Turgut, “Bone,” in *Musculoskeletal Research and Basic Science* (F. Korkusuz, ed.), pp. 303–321, Cham: Springer International Publishing, 2016.
- [72] B. Clarke, “Normal Bone Anatomy and Physiology,” *Clinical Journal of the American Society of Nephrology*, vol. 3, pp. S131–S139, Nov. 2008.
- [73] R. Amitrano and G. Tortora, *Update: Laboratory Exercises in Anatomy and Physiology with Cat Dissections*. Cengage Learning, 2012.
- [74] X. Feng, “Chemical and Biochemical Basis of Cell-Bone Matrix Interaction in Health and Disease,” *Current Chemical Biology*, vol. 3, pp. 189–196, May 2009.
- [75] U. E. Pazzaglia, T. Congiu, M. Raspanti, F. Ranchetti, and D. E. Quacci, “Anatomy of the intracortical canal system: scanning electron microscopy study in rabbit femur.,” *Clinical orthopaedics and related research*, vol. 467 9, pp. 2446–56, 2009.
- [76] B. Cooper, “The origins of bone marrow as the seedbed of our blood: From antiquity to the time of osler,” *Proceedings (Baylor University. Medical Center)*, vol. 24, pp. 115–8, 04 2011.
- [77] O. Gurevitch, S. Slavin, I. Resnick, S. Khitrin, and A. Feldman, “Mesenchymal progenitor cells in red and yellow bone marrow,” *Folia biologica*, vol. 55, pp. 27–34, 02 2009.

## Bibliography

- [78] M. C. Cora, K. Latimer, and G. S. Travlos, “Chapter 25 - bone marrow,” in *Boorman’s Pathology of the Rat (Second Edition)* (A. W. Suttie, ed.), pp. 495 – 519, Boston: Academic Press, second edition ed., 2018.
- [79] B. R. McCreadie, S. J. Hollister, M. B. Schaffler, and S. A. Goldstein, “Osteocyte lacuna size and shape in women with and without osteoporotic fracture,” *Journal of Biomechanics*, vol. 37, no. 4, pp. 563 – 572, 2004.
- [80] N. E. Lassen, T. L. Andersen, G. G. Plen, K. Se, E. M. Hauge, S. Harving, G. E. T. Eschen, and J.-M. Delaisse, “Coupling of bone resorption and formation in real time: New knowledge gained from human haversian bms,” *Journal of Bone and Mineral Research*, pp. n/a–n/a, 2017.
- [81] M. McGee-Lawrence and J. Westendorf, “Histone deacetylases in skeletal development and bone mass maintenance,” *Gene*, vol. 474, no. 1-2, pp. 1–11, 2011.
- [82] J. S. Walsh, “Normal bone physiology, remodelling and its hormonal regulation,” *Surgery (Oxford)*, vol. 33, no. 1, pp. 1 – 6, 2015. Orthopaedics I: General Principles.
- [83] L. F. Bonewald, “Mechanosensation and transduction in osteocytes,” *BoneKEy osteovision*, vol. 3, pp. 7–15, Oct 2006.
- [84] A. G. Robling and C. H. Turner, “Mechanical signaling for bone modeling and remodeling,” *Critical reviews in eukaryotic gene expression*, vol. 19, no. 4, pp. 319–338, 2009.
- [85] R. Marcus, D. Feldman, and J. Kelsey, *Osteoporosis, Two-Volume Set*. Elsevier Science, 2001.
- [86] J. Parvizi and G. K. Kim, “Chapter 160 - osteoblasts,” in *High Yield Orthopaedics* (J. Parvizi and G. K. Kim, eds.), pp. 331 – 332, Philadelphia: W.B. Saunders, 2010.
- [87] A. Bassi, J. Gough, M. Zakikhani, and S. Downes, “5 - bone tissue regeneration,” in *Electrospinning for Tissue Regeneration* (L. A. Bosworth and S. Downes, eds.), Woodhead Publishing Series in Biomaterials, pp. 93 – 110, Woodhead Publishing, 2011.
- [88] S. C. Manolagas, “From Estrogen-Centric to Aging and Oxidative Stress: A Revised Perspective of the Pathogenesis of Osteoporosis,” *Endocrine Reviews*, vol. 31, pp. 266–300, June 2010.
- [89] V. Swami, V. Vijayaraghavan, and V. Swami, “Current trends to measure implant stability,” *Journal of Indian Prosthodontic Society*, vol. 16, no. 2, pp. 124–130, 2016.

## Bibliography

- [90] P. Coelho and R. Jimbo, “Osseointegration of metallic devices: Current trends based on implant hardware design.,” *Archives of biochemistry and biophysics*, vol. 561, 07 2014.
- [91] P. Brnemark, B. Hansson, R. Adell, U. Breine, J. Lindström, O. Halln, and A. Ohman, “Osseointegrated implants in the treatment of the edentulous jaw. experience from a 10-year period,” *Scandinavian journal of plastic and reconstructive surgery. Supplementum*, vol. 16, pp. 1–132, 02 1977.
- [92] B. Ratner, “New ideas in biomaterials science a path to engineered biomaterials,” *Journal of biomedical materials research*, vol. 27, pp. 837–50, 07 1993.
- [93] S. TOM, “Kelley and firestein’s textbook of rheumatology, 2-volume set, 10th edition,” *The Journal of Rheumatology*, vol. 44, no. 6, pp. 964–964, 2017.
- [94] J. Park, C. H Gemmell, and J. Davies, “Platelet interactions with titanium: Modulation of platelet activity by surface topography,” *Biomaterials*, vol. 22, pp. 2671–82, 11 2001.
- [95] J. E. Davies, “Understanding peri-implant endosseous healing,” *Journal of dental education*, vol. 67, no. 8, pp. 932–949, 2003.
- [96] M. E. Gerritsen, “Chapter 8 - angiogenesis,” in *Microcirculation (Second Edition)* (R. F. Tuma, W. N. Durn, and K. Ley, eds.), pp. 351 – 383, San Diego: Academic Press, second edition ed., 2008.
- [97] C. A. Moreira, D. W. Dempster, and R. Baron, *Anatomy and Ultrastructure of Bone Histogenesis, Growth and Remodeling*. MDTText.com, Inc., South Dartmouth (MA), 2000.
- [98] H. Schell, G. N. Duda, A. Peters, S. Tsitsilonis, K. A. Johnson, and K. Schmidt-Bleek, “The haematoma and its role in bone healing,” *Journal of Experimental Orthopaedics*, vol. 4, p. 5, Feb 2017.
- [99] S. Overgaard, “Calcium phosphate coatings for fixation of bone implants. evaluated mechanically and histologically by stereological methods,” *Acta Orthopaedica Scandinavica*, vol. 71, no. sup297, pp. 1–74, 2001.
- [100] T. Kizuki, M. Ohgaki, M. Katsura, S. Nakamura, K. Hashimoto, Y. Toda, S. Udagawa, and K. Yamashita, “Effect of bone-like layer growth from culture medium on adherence of osteoblast-like cells,” *Biomaterials*, vol. 24, no. 6, pp. 941–947, 2003.



## Bibliography

- [101] S. Nakamura, T. Kobayashi, M. Nakamura, and K. Yamashita, “Enhanced in vivo responses of osteoblasts in electrostatically activated zones by hydroxyapatite electrets,” *Journal of Materials Science: Materials in Medicine*, vol. 20, pp. 99–103, Jan. 2009.
- [102] S. Itoh, S. Nakamura, T. Kobayashi, K. Shinomiya, K. Yamashita, and S. Itoh, “Effect of Electrical Polarization of Hydroxyapatite Ceramics on New Bone Formation,” *Calcified Tissue International*, vol. 78, pp. 133–142, Mar. 2006.
- [103] M. Ohgaki, T. Kizuki, M. Katsura, and K. Yamashita, “Manipulation of selective cell adhesion and growth by surface charges of electrically polarized hydroxyapatite,” *Journal of biomedical materials research*, vol. 57, no. 3, pp. 366–373, 2001.
- [104] V. Borsari, G. Giavaresi, M. Fini, P. Torricelli, A. Salito, R. Chiesa, L. Chiusoli, A. Volpert, L. Rimondini, and R. Giardino, “Physical characterization of different-roughness titanium surfaces, with and without hydroxyapatite coating, and their effect on human osteoblast-like cells,” *Journal of Biomedical Materials Research Part B: Applied Biomaterials*, vol. 75B, no. 2, pp. 359–368, 2005.
- [105] K. Anselme, M. Bigerelle, B. Noel, E. Dufresne, D. Judas, A. Iost, and P. Hardouin, “Qualitative and quantitative study of human osteoblast adhesion on materials with various surface roughnesses,” *Journal of Biomedical Materials Research*, vol. 49, no. 2, pp. 155–166, 2000.
- [106] A. Morse, M. McDonald, N. Kelly, K. Melville, A. Schindeler, I. Kramer, M. Kneissel, M. Van Der Meulen, and D. Little, “Mechanical load increases in bone formation via a sclerostin-independent pathway,” *Journal of Bone and Mineral Research*, vol. 29, no. 11, pp. 2456–2467, 2014.
- [107] G. Scott and J. King, “A prospective, double-blind trial of electrical capacitive coupling in the treatment of non-union of long bones,” *Journal of Bone and Joint Surgery - Series A*, vol. 76, no. 6, pp. 820–826, 1994.
- [108] H. Matsumoto, M. Ochi, Y. Abiko, Y. Hirose, T. Kaku, and K. Sakaguchi, “Pulsed electromagnetic fields promote bone formation around dental implants inserted into the femur of rabbits,” *Clinical Oral Implants Research*, vol. 11, no. 4, pp. 354–360, 2000.
- [109] E. Gongadze, D. Kabaso, S. Bauer, T. Slivnik, P. Schmuki, U. van Rienen, and A. Iglic, “Adhesion of osteoblasts to a nanorough titanium implant surface,” *International journal of nanomedicine*, vol. 6, pp. 1801–1816, 2011.
- [110] K. Anselme and M. Bigerelle, “Modelling approach in cell/material interactions studies,” *Biomaterials*, vol. 27, no. 8, pp. 1187 – 1199, 2006.

## Bibliography

- [111] X. Liu and G. L. Niebur, “Bone ingrowth into a porous coated implant predicted by a mechano-regulatory tissue differentiation algorithm,” *Biomechanics and Modeling in Mechanobiology*, vol. 7, no. 4, p. 335, 2007.
- [112] A. Andreykiv, P. Prendergast, F. van Keulen, W. Swieszkowski, and P. Rozing, “Bone ingrowth simulation for a concept glenoid component design,” *Journal of Biomechanics*, vol. 38, pp. 1023–1033, May 2005.
- [113] S.-H. Liao, R.-F. Tong, and J.-X. Dong, “Influence of anisotropy on peri-implant stress and strain in complete mandible model from CT,” *Computerized Medical Imaging and Graphics*, vol. 32, no. 1, pp. 53 – 60, 2008.
- [114] P. Moreo, M. Prez, J. Garca-Aznar, and M. Doblar, “Modelling the mechanical behaviour of living bony interfaces,” *Computer Methods in Applied Mechanics and Engineering*, vol. 196, pp. 3300–3314, July 2007.
- [115] R. A. Gittens, R. Olivares-Navarrete, R. Tannenbaum, B. D. Boyan, and Z. Schwartz, “Electrical Implications of Corrosion for Osseointegration of Titanium Implants,” *Journal of Dental Research*, vol. 90, pp. 1389–1397, Dec. 2011.
- [116] J.-H. Chen, C. Liu, L. You, and C. Simmons, “Boning up on wolff’s law: Mechanical regulation of the cells that make and maintain bone,” *Journal of biomechanics*, vol. 43, pp. 108–18, 10 2009.
- [117] C. Potratz, D. Kluess, H. Ewald, and U. van Rienen, “Multiobjective optimization of an electrostimulative acetabular revision system,” *IEEE Transactions on Biomedical Engineering*, vol. 57, no. 2, pp. 460–468, 2009.
- [118] U. Zimmermann and U. van Rienen, “An automatic pareto classifier for the multiobjective optimization of an electrostimulative acetabular revision system,” *IEEE Transactions on Magnetics*, vol. 50, no. 2, pp. 741–744, 2014.
- [119] C. Schmidt, U. Zimmermann, and U. van Rienen, “Modeling of an optimized electrostimulative hip revision system under consideration of uncertainty in the conductivity of bone tissue,” *IEEE journal of biomedical and health informatics*, vol. 19, no. 4, pp. 1321–1330, 2015.
- [120] J. K. Song, T. H. Cho, H. Pan, Y. M. Song, I. S. Kim, T. H. Lee, S. J. Hwang, and S. J. Kim, “An electronic device for accelerating bone formation in tissues surrounding a dental implant,” *Bioelectromagnetics*, vol. 30, pp. 374–384, July 2009.
- [121] J. Murray, *II. Spatial Models and Biomedical Applications*. Springer, 2003.

## Bibliography

- [122] J. D. Murray, *Mathematical Biology I. An Introduction*, vol. 17 of *Interdisciplinary Applied Mathematics*. New York: Springer, 3 ed., 2002.
- [123] G. Khalil, *Modeling of the bone-implant healing; mechanobiology of osteoblasts population in presence of endothelial cells*. PhD thesis, Universit de Toulouse, Universit Toulouse III-Paul Sabatier, 2011.
- [124] X. Yang, *Mathematical Modeling with Multidisciplinary Applications*. Wiley, 2013.
- [125] G. Larry A, “Analytic solution of partial differential equations,” in *Applied Mathematics for Science and Engineering*, ch. 7, pp. 111–146, John Wiley & Sons, Ltd, 2014.
- [126] E. Billo, “Partial differential equations,” in *Excel for Scientists and Engineers*, ch. 12, pp. 263–286, John Wiley & Sons, Ltd, 2006.
- [127] S. Guy, “Appendix c: Comparison between different numerical methods,” in *Practical Finite Element Modeling in Earth Science Using Matlab*, pp. 227–235, John Wiley & Sons, Ltd, 2017.
- [128] R. Lewis, P. Nithiarasu, and K. Seetharamu, “The finite element method,” in *Fundamentals of the Finite Element Method for Heat and Fluid Flow*, ch. 3, pp. 38–101, John Wiley & Sons, Ltd, 2005.
- [129] A. Bondeson, T. Rylander, and P. Ingelström, *Computational Electromagnetics*. Texts in Applied Mathematics, Springer New York, 2005.
- [130] A. B. Michael Aichinger, “Finite element methods,” in *A Workout in Computational Finance*, ch. 7, pp. 81–115, John Wiley & Sons, Ltd, 2013.
- [131] C. Pullar, *The Physiology of Bioelectricity in Development, Tissue Regeneration and Cancer*. Biological effects of electromagnetics series, CRC Press, 2016.
- [132] H.-Y. Yang, T. Dinh La, and R. R. Isseroff, “Utilizing Custom-designed Galvanotaxis Chambers to Study Directional Migration of Prostate Cells,” *Journal of Visualized Experiments*, Dec. 2014.
- [133] K. J. Painter and J. A. Sherratt, “Modelling the movement of interacting cell populations,” *Journal of Theoretical Biology*, vol. 225, pp. 327–339, Dec. 2003.
- [134] U. van Rienen, “Numerical methods in computational electrodynamics: Linear systems in practical applications,” ch. Classical Electrodynamics, pp. 11–34, Berlin, Heidelberg: Springer Berlin Heidelberg, 2001.

## Bibliography

- [135] E. F. Keller and L. A. Segel, "Initiation of slime mold aggregation viewed as an instability," *Journal of Theoretical Biology*, vol. 26, no. 3, pp. 399 – 415, 1970.
- [136] G. Tai, B. Reid, L. Cao, and M. Zhao, "Electrotaxis and wound healing: Experimental methods to study electric fields as a directional signal for cell migration," *Methods in molecular biology (Clifton, N.J.)*, vol. 571, pp. 77–97, 07 2009.
- [137] M. Waleed Shinwari, D. Zhitomirsky, I. Deen, P. Selvaganapathy, M. Jamal Deen, and D. Landheer, "Microfabricated reference electrodes and their biosensing applications," *Sensors*, vol. 10, no. 3, pp. 1679–1715, 2010.
- [138] S. Zhao, K. Zhu, Y. Zhang, Z. Zhu, Z. Xu, M. Zhao, and T. Pan, "ElectroTaxis-on-a-Chip (ETC): an integrated quantitative high-throughput screening platform for electrical field-directed cell migration," *Lab Chip*, vol. 14, pp. 4398–4405, Sept. 2014.
- [139] S. Zhao, R. Gao, P. N. Devreotes, A. Mogilner, and M. Zhao, "3d arrays for high throughput assay of cell migration and electrotaxis," *Cell Biology International*, vol. 37, no. 9, pp. 995–1002, 2013.
- [140] M. B. Djamgoz, M. Mycielska, Z. Madeja, S. P. Fraser, and W. Korohoda, "Directional movement of rat prostate cancer cells in direct-current electric field," *Journal of cell science*, vol. 114, no. 14, pp. 2697–2705, 2001.
- [141] L. Li, Y. H. El-Hayek, B. Liu, Y. Chen, E. Gomez, X. Wu, K. Ning, L. Li, N. Chang, L. Zhang, Z. Wang, X. Hu, and Q. Wan, "Direct-current electrical field guides neuronal stem/progenitor cell migration," *Stem cells*, vol. 26, no. 8, pp. 2193–2200, 2008.
- [142] M. Zhao, A. Agius-Fernandez, J. Forrester, and C. McCaig, "Orientation and directed migration of cultured corneal epithelial cells in small electric fields are serum dependent," *Journal of Cell Science*, vol. 109, no. 6, pp. 1405–1414, 1996.
- [143] X. Yan, J. Han, Z. Zhang, J. Wang, Q. Cheng, K. Gao, Y. Ni, and Y. Wang, "Lung cancer A549 cells migrate directionally in DC electric fields with polarized and activated EGFRs," *Bioelectromagnetics*, vol. 30, pp. 29–35, Jan. 2009.
- [144] D. Watson and D. Yee, "Behaviour of ag/agcl electrodes in solutions containing both cl and i," *Electrochimica Acta*, vol. 14, no. 11, pp. 1143 – 1153, 1969.
- [145] A. P. Abbott, K. E. Ttaib, G. Frisch, K. S. Ryder, and D. Weston, "The electrodeposition of silver composites using deep eutectic solvents," *Physical Chemistry Chemical Physics*, vol. 14, no. 7, p. 2443, 2012.

## Bibliography

- [146] G. J. Janz and D. J. G. Ives, "Silver, silver chloride electrodes," *Annals of the New York Academy of Sciences*, vol. 148, no. 1, pp. 210–221, 1968.
- [147] V. Birss and C. Smith, "The anodic behavior of silver in chloride solutions. the formation and reduction of thin silver chloride films," *Electrochimica Acta*, vol. 32, no. 2, pp. 259 – 268, 1987.
- [148] A. W. J. Cranny and J. K. Atkinson, "Thick film silver-silver chloride reference electrodes," *Measurement Science and Technology*, vol. 9, no. 9, p. 1557, 1998.
- [149] H. Suzuki, A. Hiratsuka, S. Sasaki, and I. Karube, "Problems associated with the thin-film Ag/AgCl reference electrode and a novel structure with improved durability," *Sensors and Actuators B: Chemical*, vol. 46, pp. 104–113, Feb. 1998.
- [150] L. Bousse, P. Bergveld, and H. Geeraedts, "Properties of ag/agcl electrodes fabricated with ic-compatible technologies," *Sensors and Actuators*, vol. 9, no. 3, pp. 179–197, 1986.
- [151] A. Belkind, E. Ezell, M. Dror, W.-A. Luo, J. Jacobs, and M. Lagally, "Compositional and morphological analysis of agcl films deposited by evaporation and r.f. sputtering," *Thin Solid Films*, vol. 142, no. 1, pp. 113 – 125, 1986.
- [152] C. Escoffier, P. D. Maguire, C. Mahony, W. G. Graham, E. T. McAdams, and J. A. McLaughlin, "Plasma Chloriding of Thin-Film Silver," *Journal of The Electrochemical Society*, vol. 149, no. 4, p. H98, 2002.
- [153] C. S. Feigerle, "Experiments in physical chemistry, sixth edition (shoemaker, david p.; garland, carl w.; nibler, joseph w.)," *Journal of Chemical Education*, vol. 74, no. 5, p. 492, 1997.
- [154] G. J. Janz and H. Taniguchi, "The silver-silver halide electrodes. preparation, stability, and standard potentials in aqueous and non-aqueous media.," *Chemical Reviews*, vol. 53, no. 3, pp. 397–437, 1953.
- [155] C. D. McCaig, "Controlling Cell Behavior Electrically: Current Views and Future Potential," *Physiological Reviews*, vol. 85, pp. 943–978, July 2005.
- [156] E. K. Onuma and S. W. Hui, "Electric field-directed cell shape changes, displacement, and cytoskeletal reorganization are calcium dependent.," *The Journal of Cell Biology*, vol. 106, no. 6, pp. 2067–2075, 1988.
- [157] M.-M. Poo, W. J. Poo, and J. W. Lam, "Lateral electrophoresis and diffusion of Concanavalin A receptors in the membrane of embryonic muscle cell.," *The Journal of cell biology*, vol. 76, no. 2, pp. 483–501, 1978.

## Bibliography

- [158] M. Poo and K. R. Robinson, "Electrophoresis of concanavalin a receptors along embryonic muscle cell membrane.," *Nature*, vol. 265 5595, pp. 602–5, 1977.
- [159] A. Schopf, C. Boehler, and M. Asplund, "Analytical methods to determine electrochemical factors in electrotaxis setups and their implications for experimental design," *Bioelectrochemistry*, vol. 109, pp. 41 – 48, 2016.
- [160] R. Funk and T. Monsees, "Effects of electromagnetic fields on cells: Physiological and therapeutical approaches and molecular mechanisms of interaction. a review," *Cells Tissues Organs*, vol. 182, no. 2, pp. 59–78, 2006.
- [161] L. Guo, C. Xu, D. Li, X. Zheng, J. Tang, J. Bu, H. Sun, Z. Yang, W. Sun, and X. Yu, "Calcium Ion Flow Permeates Cells through SOCs to Promote Cathode-Directed Galvanotaxis," *PLOS ONE*, vol. 10, p. e0139865, Oct. 2015.
- [162] G.-H. Lee, J.-D. Hwang, J.-Y. Choi, H.-J. Park, J.-Y. Cho, K.-W. Kim, H.-J. Chae, and H.-R. Kim, "An acidic pH environment increases cell death and pro-inflammatory cytokine release in osteoblasts: The involvement of BAX Inhibitor-1," *The International Journal of Biochemistry & Cell Biology*, vol. 43, pp. 1305–1317, Sept. 2011.
- [163] W. K. Ramp, L. G. Lenz, and K. K. Kaysinger, "Medium ph modulates matrix, mineral, and energy metabolism in cultured chick bones and osteoblast-like cells," *Bone and Mineral*, vol. 24, no. 1, pp. 59 – 73, 1994.
- [164] J. Ferrier, S. M. Ross, J. Kanehisa, and J. E. Aubin, "Osteoclasts and osteoblasts migrate in opposite directions in response to a constant electrical field," *Journal of Cellular Physiology*, vol. 129, no. 3, pp. 283–288, 1986.
- [165] S. Curtze, M. Dembo, M. Miron, and D. B. Jones, "Dynamic changes in traction forces with dc electric field in osteoblast-like cells," *Journal of Cell Science*, vol. 117, no. 13, pp. 2721–2729, 2004.
- [166] S. M. Ross, J. M. Ferrier, and J. E. Aubin, "Studies on the alignment of fibroblasts in uniform applied electrical fields," *Bioelectromagnetics*, vol. 10, no. 4, pp. 371–384, 1989.
- [167] N. Tandon, B. Goh, A. Marsano, P. H. G. Chao, C. Montouri-Sorrentino, J. Gimble, and G. Vunjak-Novakovic, "Alignment and elongation of human adipose-derived stem cells in response to direct-current electrical stimulation," in *2009 Annual International Conference of the IEEE Engineering in Medicine and Biology Society*, pp. 6517–6521, Sept 2009.

## Bibliography

- [168] A. Hicks, A. Panitch, M. Caplan, and J. D. Sweeney, “An Incubatable Direct Current Stimulation System for *In Vitro* Studies of Mammalian Cells,” *BioResearch Open Access*, vol. 1, pp. 199–203, Aug. 2012.
- [169] P.-H. Chao, R. Roy, R. Mauck, W. Liu, W. Valhmu, and C. Hung, “Chondrocyte translocation response to direct current electric fields,” *Journal of Biomechanical Engineering*, vol. 122, no. 3, pp. 261–267, 2000.
- [170] Alberts B, Lewis A, and et al, “Fibroblasts and Their Transformations: The Connective-Tissue Cell,” in *Molecular Biology of the Cell*, New York: Garland Science, 4 ed., 2002.
- [171] C. Frantz, K. M. Stewart, and V. M. Weaver, “The extracellular matrix at a glance,” *Journal of Cell Science*, vol. 123, no. 24, pp. 4195–4200, 2010.
- [172] C. A. Schneider, W. S. Rasband, and K. W. Eliceiri, “NIH Image to ImageJ: 25 years of image analysis,” *Nature Methods*, vol. 9, pp. 671–675, June 2012.
- [173] E. M. Czekanska, M. J. Stoddart, J. R. Ralphs, R. G. Richards, and J. S. Hayes, “A phenotypic comparison of osteoblast cell lines versus human primary osteoblasts for biomaterials testing: Phenotypic Comparison of Osteoblast Cell Lines,” *Journal of Biomedical Materials Research Part A*, vol. 102, pp. 2636–2643, Aug. 2014.
- [174] A. Burmester, R. Willumeit-Rmer, and F. Feyerabend, “Behavior of bone cells in contact with magnesium implant material,” *Journal of Biomedical Materials Research Part B: Applied Biomaterials*, vol. 105, no. 1, pp. 165–179, 2017.
- [175] M. Rohde, J. Ziebart, T. Kirschstein, T. Sellmann, K. Porath, F. Khl, B. Delenda, C. Bahls, U. van Rienen, R. Bader, and R. Khling, “Human osteoblast migration in dc electrical fields depends on store operated ca<sup>2+</sup>-release and is correlated to upregulation of stretch-activated trpm7 channels,” *Frontiers in Bioengineering and Biotechnology*, vol. 7, p. 422, 2019.
- [176] A. Burmester, B. Luthringer, R. Willumeit, and F. Feyerabend, “Comparison of the reaction of bone-derived cells to enhanced MgCl<sub>2</sub>-salt concentrations,” *Biomatter*, vol. 4, p. e967616, Jan. 2014.
- [177] S. Zhao, K. Zhu, Y. Zhang, Z. Zhu, Z. Xu, M. Zhao, and T. Pan, “Electrotaxis-on-a-chip (etc): an integrated quantitative high-throughput screening platform for electrical field-directed cell migration,” *Lab Chip*, vol. 14, pp. 4398–4405, 2014.
- [178] F. Heuck and U. Staufer, “Silver/silver-chloride electrode fabrication in closed micro-fluidic capillaries,” *Microelectronic Engineering*, vol. 87, no. 58, pp. 1383

## Bibliography

- 1385, 2010. The 35th International Conference on Micro- and Nano-Engineering (MNE).
- [179] A. P. Mazzoleni, B. F. Siskin, and R. L. Kahler, “Conductivity values of tissue culture medium from 20 C to 40 C,” *Bioelectromagnetics*, vol. 7, no. 1, pp. 95–99, 1986.
- [180] M. Nuez, ed., *Trends in electrochemistry research*. New York: Nova Science Publishers, 2007.
- [181] U. van Rienen, “Numerical methods in computational electrodynamics: Linear systems in practical applications,” ch. Numerical Treatment of Linear Systems, pp. 83–203, Berlin, Heidelberg: Springer Berlin Heidelberg, 2001.
- [182] R. K. Rhodes and R. P. Buck, “Impedance characterization of anodized silver/silver chloride electrodes,” *Analytica Chimica Acta*, vol. 113, no. 1, pp. 55–66, 1980.
- [183] H. Ha and J. Payer, “The effect of silver chloride formation on the kinetics of silver dissolution in chloride solution,” *Electrochimica Acta*, vol. 56, pp. 2781–2791, Feb. 2011.
- [184] T. R. Beck, “Conductivity of Anodic Silver Chloride during Formation,” *Journal of The Electrochemical Society*, vol. 131, no. 1, p. 89, 1984.
- [185] Y.-J. Huang, J. Samorajski, R. Kreimer, and P. C. Searson, “The Influence of Electric Field and Confinement on Cell Motility,” *PLoS ONE*, vol. 8, p. e59447, Mar. 2013.
- [186] X. Jin, J. Lu, P. Liu, and H. Tong, “The electrochemical formation and reduction of a thick agcl deposition layer on a silver substrate,” *Journal of Electroanalytical Chemistry*, vol. 542, pp. 85–96, 2003.
- [187] H. Lal, H. R. Thirsk, and W. F. K. Wynne-Jones, “A study of the behaviour of polarized electrodes. Part I. The silver/silver halide system,” *Transactions of the Faraday Society*, vol. 47, pp. 70–77, 1951.
- [188] J. Tiwari and C. Rao, “Template synthesized high conducting silver chloride nanoplates,” *Solid State Ionics*, vol. 179, pp. 299–304, May 2008.
- [189] E. Gongadze, U. van Rienen, and A. Iglic, “Generalized stern models of the electric double layer considering the spatial variation of permittivity and finite size of ions in saturation regime,” *Cellular & molecular biology letters*, vol. 16, pp. 576–594, Dec 2011.



## Bibliography

- [190] D. C. Grahame, “The electrical double layer and the theory of electrocapillarity,” *Chemical Reviews*, vol. 41, no. 3, pp. 441–501, 1947.
- [191] W. Du, *Resistive, Capacitive, Inductive, and Magnetic Sensor Technologies*. Series in Sensors, CRC Press, 2014.
- [192] M. Neuman, “Biopotential electrodes,” *Medical Instrumentation: Application and Design*, 3rd ed., pp. 183–232, 1998.
- [193] W. Du, *Resistive, Capacitive, Inductive, and Magnetic Sensor Technologies*. Series in Sensors, CRC Press, 2014.
- [194] V. S. Bagotsky, “Structure and Properties of Surface Layers,” in *Fundamentals of Electrochemistry*, pp. 147–180, Hoboken, NJ, USA: John Wiley & Sons, Inc., Dec. 2005. DOI: 10.1002/047174199X.ch10.
- [195] P. E. Long and D. W. Pepper, “An Examination of Some Simple Numerical Schemes for Calculating Scalar Advection,” *Journal of Applied Meteorology*, vol. 20, pp. 146–156, Feb. 1981.
- [196] K. Soetaert and P. Herman, *A Practical Guide to Ecological Modelling: Using R as a Simulation Platform*. Biomedical and Life Sciences, Springer Netherlands, 2008.
- [197] B. Cohen, A. Voorhees, S. Vedel, and T. Wei, “Development of a theoretical framework for analyzing cerebrospinal fluid dynamics,” *Cerebrospinal Fluid Research*, vol. 6, no. 1, p. 12, 2009.
- [198] X.-M. Li and H. Z. Zhao, “Gradient estimates and the smooth convergence of approximate travelling waves for reaction - diffusion equations,” *Nonlinearity*, vol. 9, pp. 459–477, mar 1996.
- [199] R. Erban and H. G. Othmer, “From Individual to Collective Behavior in Bacterial Chemotaxis,” *SIAM Journal on Applied Mathematics*, vol. 65, pp. 361–391, Jan. 2004.
- [200] K. C. Dee, T. T. Andersen, and R. Bizios, “Osteoblast population migration characteristics on substrates modified with immobilized adhesive peptides,” *Biomaterials*, vol. 20, no. 3, pp. 221–227, 1999.
- [201] P. Moreo, J. M. Garca-Aznar, and M. Doblar, “Bone ingrowth on the surface of endosseous implants. Part 2: Theoretical and numerical analysis,” *Journal of Theoretical Biology*, vol. 260, pp. 13–26, Sept. 2009.

## Bibliography

- [202] B. Delenda, R. Bader, and U. van Rienen, "Modeling and simulation of platelet reaction and diffusion towards an electro-stimulating dental implant," in *Engineering in Medicine and Biology Society (EMBC), 2015 37th Annual International Conference of the IEEE*, pp. 2584–2587, IEEE, 2015.
- [203] S. Gabriel, R. W. Lau, and C. Gabriel, "The dielectric properties of biological tissues: III. Parametric models for the dielectric spectrum of tissues," *Physics in medicine and biology*, vol. 41, no. 11, p. 2271, 1996.
- [204] W. F. Ganong, *Review of Medical Physiology*. New York: McGraw-Hill, 22nd ed., 2005.
- [205] P. D. Goodman, E. T. Barlow, P. M. Crapo, S. F. Mohammad, and K. A. Solen, "Computational Model of Device-Induced Thrombosis and Thromboembolism," *Annals of Biomedical Engineering*, vol. 33, pp. 780–797, June 2005.
- [206] W. Kraus, "[Magnetic field therapy and magnetically induced electrostimulation in orthopedics]. Magnetfeldtherapie und magnetisch induzierte elektrostimulation in der orthopadie," *Der Orthopade*, vol. 13, p. 7892, April 1984.
- [207] A. Zareidoost, M. Yousefpour, B. Ghaseme, and A. Amanzadeh, "The relationship of surface roughness and cell response of chemical surface modification of titanium," *Journal of materials science. Materials in medicine*, vol. 23, pp. 1479–1488, Jun 2012.
- [208] L. Marinucci, S. Balloni, E. Becchetti, S. Belcastro, M. Guerra, M. Calvitti, C. Lilli, E. Calvi, and P. Locci, "Effect of titanium surface roughness on human osteoblast proliferation and gene expression in vitro," *International Journal of Oral and Maxillofacial Implants*, vol. 21, no. 5, pp. 719–725, 2006.
- [209] K. Mustafa, J. Wroblewski, B. S. Lopez, A. Wennerberg, K. Hultenby, and K. Arvidson, "Determining optimal surface roughness of tio2 blasted titanium implant material for attachment, proliferation and differentiation of cells derived from human mandibular alveolar bone," *Oral Implants Research*, vol. 12, no. 5, pp. 515–525, 2001.